# Longitudinal subglacial bedform semi-automated mapping and measurement

**by**

**Marco André Gaspar Jorge**

Licenciatura (Geografia, variante Física), Universidade de Lisboa, 2009

Dissertation Submitted in Partial Fulfillment of the
Requirements for the Degree of
Master of Science

in the
Department of Geography
Faculty of Environment

**© Marco G. Jorge 2015**

**SIMON FRASER UNIVERSITY**

**Summer 2015**

All rights reserved.
However, in accordance with the *Copyright Act of Canada*, this work may be reproduced, without authorization, under the conditions for "Fair Dealing." Therefore, limited reproduction of this work for the purposes of private study, research, criticism, review and news reporting is likely to be in accordance with the law, particularly if cited appropriately.

# Approval

**Name:** **Marco André Gaspar Jorge**

**Degree:** **Master of Science**

**Title:** ***Longitudinal subglacial bedform semi-automated mapping and measurement***

**Examining Committee:** **Chair:** Geoff Mann
Associate Professor

**Tracy Brennand**
Senior Supervisor
Professor

**Suzana Dragićević**
Supervisor
Professor

**Darren Sjogren**
External Examiner
Associate Professor
Department of Geography
University of Calgary

**Date Defended/Approved:** May 25, 2015

## Abstract

This thesis addresses methodological issues in the morphometric inventorying of relict drumlins and mega-scale glacial lineations (longitudinal subglacial bedforms, LSBs) which pose limits to a robust description of LSB morphometry and thus to testing hypotheses of LSB genesis, with implications for postdicting past, and predicting future, ice sheet behavior. Focus is on a) the adequacy of previously used morphometric measurement methods (MMM) (GIS) and b) the development of LSB semi-automated mapping (SAM) methods. Dimensions derived from an ellipse fitted to the LSB footprint based on Euler's approximation are inaccurate and both these and orientation based on the longest straight line enclosed by the footprint are imprecise. A newly tested MMM based on the standard deviational ellipse performs best. A new SAM method outperforms previous methods. It is based on the analysis of normalized local relief closed contours and on a supervised ruleset encapsulating expert knowledge, published morphometric data and study area LSB morphometry.



**Keywords**: drumlin; mega-scale glacial lineation; morphometry; semi-automated mapping; flow direction; paleoglaciology

## Acknowledgements

My research was supported by a SFU Graduate Fellowship and a GSA Student Research Grant to myself and by a NSERC Discovery grant to Tracy A. Brennand. Income from Teaching Assistantships at SFU Department of Geography was fundamental in allowing me to study and live in Greater Vancouver. I would like to thank the users of the SAGA GIS discussion forum, and in particular Volker Wichmann, for helping me to understand the computation of normalized altitude (Böhner and Selige, 2006; used in Chapter 2).

I am deeply thankful to Prof. Tracy A. Brennand for having selected me to be part of the Glacial Geomorphology research team, unreservedly sharing her know-how and being completely open to my topical deambulations. Tracy's reviews of my manuscripts were a very good learning tool and I just wish that future reviewers I come across are as insightful and rigorous as Tracy is. I was privileged to have Tracy as senior supervisor and look forward to further collaboration. I would also like to thank Prof. Suzana Dragićević for discussions and suggestions on research methods, and both Prof. Suzana Dragićević and Prof. Darren Sjogren for taking part in the examining committee.

All SFU staff I dealt with were extremely nice, uncomplicated and helpful. A special thanks to the staff of the Department of Geography (Liliana, Anke, Marion, Joyce, Tiina, B-Jae, John, Chris and Justin) and to Eugene McCann and Geoff Mann, graduate research chairs. Thanks to the cleaning staff for keeping the RCB building shining.

Thanks to Josephine and fellow grads Jonny Cripps and Andrew Perkins for sharing the lab with me, engaging on both relevant and irrelevant discussions, and making me believe that what I was saying made sense.

Thank you to all my students, but not sure why.

Most importantly, thanks to myself and to my family.

# Table of Contents

Approval ..... ii
Abstract ..... iii
Acknowledgements ..... iv
Table of Contents ..... v
List of Tables ..... vii
List of Figures ..... ix

**Chapter 1. Introduction ..... 1**
1.1. Research rationale: Decoding longitudinal subglacial bedforms ..... 1
1.1.1. Longitudinal subglacial bedforms and their unexplained genesis ..... 1
1.1.2. Morphometric data: past and future ..... 5
1.1.3. LSB morphometry in past paleoglaciological reconstructions ..... 8
1.2. Research objectives ..... 8
1.3. Thesis organization and authorship ..... 9
1.4. Additional work ..... 10
1.5. References ..... 10

**Chapter 2. Measuring subglacial bedform orientation, length and asymmetry – method accuracy ..... 18**
2.1. Highlights ..... 18
2.2. Abstract ..... 18
2.3. Introduction ..... 19
2.4. Prior work ..... 21
2.5. Methodology ..... 22
2.5.1. LSB mapping ..... 23
2.5.2. Reference longitudinal axis ..... 24
2.5.3. Elliptical length ..... 25
2.5.4. Longest straight line ..... 25
2.5.5. Minimum bounding rectangle longitudinal axis ..... 25
2.5.6. Standard deviational ellipse longitudinal axis ..... 26
2.5.7. Morphometric data from LAs ..... 26
2.5.8. Performance assessment ..... 28
2.6. Results ..... 28
2.7. Discussion ..... 32
2.7.1. Dependence of method adequacy on footprint shape ..... 33
LSL, RLA and SDE methods ..... 33
Elliptical length ..... 36
2.7.2. Implications for previous works ..... 37
2.7.3. Outlook ..... 38
2.8. Conclusion ..... 40
2.9. References ..... 40

**Chapter 3. Towards the semi-automated extraction of longitudinal subglacial bedforms from DTMs – two new methods ..... 44**
3.1. Highlights ..... 44
3.2. Abstract ..... 44
3.3. Introduction ..... 45
3.4. Object-based mapping of LSBs: past work ..... 48
3.5. Methods ..... 49
3.5.1. Test area and DTM ..... 51
3.5.2. LSB manual mapping ..... 51
3.5.3. LSB operational definition ..... 53
3.5.4. DTM preprocessing ..... 56
3.5.5. Normalized closed contour method ..... 58
Implementation ..... 59
3.5.6. Landform elements mask method ..... 63
Implementation ..... 63
3.5.7. Performance assessment ..... 65
3.6. Results ..... 68
3.6.1. Manual mapping ..... 68
3.6.2. Object-oriented performance assessment ..... 68
3.6.3. Cell-based performance assessment ..... 69
3.7. Discussion ..... 72
3.7.1. DTM preprocessing ..... 72
3.7.2. Object-oriented performance assessment ..... 72
3.7.3. Cell-based performance assessment ..... 76
3.7.4. Comparison to previous methods ..... 77
3.7.5. Methodology limitations ..... 80
3.8. Conclusion ..... 82
3.9. References ..... 83

**Chapter 4. Conclusions ..... 93**
4.1. LSB measurement methods ..... 93
4.2. LSB mapping ..... 94
4.3. Novelty of conducted research ..... 96
4.4. References ..... 97
Appendix A. Puget Lowland drumlin field integrated terrain map ..... 100
Appendix B. LSB manual mapping in the Puget Lowland drumlin field ..... 101
Appendix C. Field investigations on LSB composition in the Puget Lowland drumlin field – visited sites ..... 102

# List of Tables


Table 1.1 LSB formation hypotheses classified by formative agent ..... 6

Table 2.1 Morphometric statistics for the LSB dataset used in this study ($n$ = 100); based on footprints' minimum bounding rectangle; elongation is the ratio of length to width; longitudinal asymmetry is the ratio between the footprints' upflow area and total area ($AS_{pl\_A}$ of Spagnolo et al., 2010) ..... 24

Table 2.2 Morphometric statistics for LSBs with E <5 based on footprints' minimum bounding rectangle ..... 30

Table 2.3 95th percentile of the absolute differences between data from the automated methods and the reference LA for footprints with elongation < 5 ..... 30

Table 2.4 Correlation between morphometric measure performance ($n$ = 60) ..... 30

Table 2.5 Performance assessment (MAE, mean absolute error; SD, standard deviation) ($n$ = 60); the lowest and highest values are bolded and underlined, respectively ..... 32

Table 2.6 Differences between means ($n$ = 60) – automated methods vs. reference data ..... 32

Table 2.7 General guidelines on footprint shapes more suited to the LSL and RLA methods ..... 33

Table 3.1 LSB operational definition (ruleset) and corresponding values for the test area; minimum and maximum values for measures 3-10 refer to MM-footprints in the test area ..... 55

Table 3.2 Object-oriented performance measures ..... 67

Table 3.3 MM-footprint morphometry ..... 68

Table 3.4 Performance assessment; with the exception of N-new (number of footprints) and TSS and kappa, all values are percentages; DMI, Difference of means index; DMI-A, all SAM & all MM; DMI-B, satisfactory SAM & all MM; DMI-C, satisfactory SAM & their respective MM footprints ..... 69

Table 3.5 Correlation (Pearson's coefficient) of footprint morphometry measures between satisfactory SAM-footprints and their respective MM-footprints (DMI-C) ..... 71

Table 3.6 Morphometric differences (% difference of SAM-footprints mean relative to MM-footprints mean) between satisfactory SAM-footprints and their respective MM-footprints (DMI-C) ..... 71

Table 3.7 Morphometric differences (% difference of SAM-footprints mean relative to MM-footprints mean) between the complete datasets of SAM- and MM-footprints (DMI-A) ..... 71

Table 3.8 Overall performance index ..... 75

Table 3.9 Overall performance index after the exclusion of regions where LSBs do not occur or are much degraded (Fig. 3.11) ..... 78

Table 3.10 SAM-method performance after the exclusion of regions where LSBs do not occur or are much degraded (Fig. 3.11); numbers within brackets represent changes relative to values in Table 3.4 (no mask) ..... 78

Table 3.11 Performance comparison between d'Oleire-Oltmanns et al. (2013) method and the NHR and NHRC methods; best-scoring method in each measure is also given; all values are percentages ..... 79

# List of Figures


Figure 1.1 Relict LSBs (mostly drumlins) in the Puget Lowland, WA, USA. Hillshaded terrain model derived from a 1.8 m cell-size DTM (http://pugetsoundlidar.ess. washington.edu/About_PSLC.htm). ..... 3

Figure 1.2 Relict mega-scale glacial lineations at the south margin of the Juan de Fuca Straight west of the Puget Lowland, WA, USA. Hillshaded terrain model derived from a 1.8 m cell-size DTM (http://pugetsoundlidar.ess.washington.edu/About_PSLC.htm). ..... 4

Figure 1.3 Morphological drumlin types based on investigations in the Livingstone Lake drumlin field, Saskatchewan, Canada (modified from Shaw, 1983). ..... 5

Figure 2.1 Derivation of the morphometric database for method evaluation. LSB = longitudinal subglacial bedform; DTM = digital terrain model; GME = Geospatial Modeling Environment (Beyer, 2012); SDE = standard deviational ellipse (Lefever, 1926); DEM = digital elevation model; $AS_{pl\_A}$: the ratio between the footprints' upflow area and total area (Spagnolo et al., 2010). ..... 23

Figure 2.2 Examples of manually mapped LSB footprints and LAs. ..... 24

Figure 2.3 Computation of the standard deviational ellipse (modified from Raine, 1978). Refer to text for explanation. ..... 27

Figure 2.4 Relationship between footprint elongation and morphometric differences between methods: A) difference in orientation relative to the LSL method; B) difference in length relative to elliptical length; C) difference between longitudinal asymmetry computed using the LSL and RLA methods. ..... 29

Figure 2.5 Cumulative histogram of automated method errors (differences to reference LA) ($n$ = 60): A, orientation; B, Length; C, longitudinal asymmetry ($AS_{pl\_A,}$ Spagnolo et al., 2010). ..... 31

Figure 2.7 Idealized shapes: A) elliptical; B) half-lemniscate (non-elliptical oval); C) rectangular; D) parabolic with symmetric crescentic lee; E) hyperbolic with symmetric convex lee; F) hyperbolic with asymmetric convex lee. A and C have 2 axes of symmetry; B, D and E have 1 axis of symmetry. Inside the shapes: solid lines represent the LA and its perpendicular bisector; dashed lines are the LSL and its perpendicular bisector. Angles in C, D and E represent the difference in orientation between the LA and the LSL. ..... 34

Figure 2.8 Examples of Puget Lowland LSB-footprints for which the LSL is a better approximation to the reference LA (orientation) than the RLA. Grey lines are the minimum bounding rectangle and its mid-axes; dashed lines represent the LSL and its perpendicular bisector; solid black lines are the reference LA. Bars at the bottom are 200 m wide. ..... 34

Figure 2.9 Examples of Puget Lowland LSB-footprints for which the RLA is a better approximation to the reference LA (orientation) than the LSL. Grey lines are the minimum bounding rectangle and its mid-axes; dashed lines represent the LSL and its perpendicular bisector; solid black lines are the reference LA. Bars at the bottom are 200 m wide for A and C-I and 100m wide for B. ..... 35

Figure 2.10 SDE2 longitudinal axis examples (solid lines). Dots are the footprint's vertices used to compute the SDE. Bars at the bottom are 200 m wide. ..... 36

Figure 2.11 Footprints with relatively large difference in orientation between the SDE2 and SDE3 methods. Short-dashed, wide-dashed and solid lines represent the orientation of the SDE2, SDE3 and reference LAs, respectively. Black and white dots are the un-rotated and rotated footprints' structural vertices. From left to right and top to bottom, angular divergence between SDE2 and SDE3 lines is 1.7º, 1.1º, 2.2º, 1.3º, 1.7º and 0.6º. Bars at the bottom are 100 m wide. ..... 37

Figure 2.12 Dependence of elliptical length accuracy on footprint general shape and outline complexity. A) E = 3, and two axes (1, 2) or one axis (3, 4) of symmetry; B) E = 3, and zero axes (1-3) or one axis (4) of symmetry; C) E = 6, and zero axes (1-3) or one axis (4) of symmetry. D) Elliptical length error (%). ..... 38

Figure 2.13 Dependence of elliptical length accuracy on elongation (i.e. area-perimeter ratio): example for an ellipse (A) and for a rectangle (B). Elliptical length error = *[(elliptical length – reference LA length) / reference LA length]* * 100. ..... 39

Figure 3.1 NCCM processing flow. ..... 50

Figure 3.2 LEMM processing flow. ..... 50

Figure 3.3 Test area. A) Location of the test area (black-outline quadrangle) within the Puget Lowland Drumlin Field and Puget Lobe footprint; the white line marks the last maximum extent of the Cordilleran Ice Sheet (Thorson, 1980). The hillshaded terrain model (10x vertical exaggeration) is derived from the USGS National Elevation Data 1/3 arc-second DTM. B) Hillshaded terrain model (5x vertical exaggeration, from a 9.1 m cell-size DTM – PSDEM, Finlayson, 2005) of the test area and footprints of figures presented later. ..... 52

Figure 3.4 DTM before (A) and after (B) preprocessing. Contour interval is 2 m. Arrow points to a road. ..... 57

Figure 3.5 NLR models for part of the test area (refer to Fig. 3.3 for location). A) Preprocessed DTM; B) NNR; C) TPI; D) NHR; E) NHR2; F) NHRC. A ranges between 87-177m a.s.l.; B, D and E range between 0-1; C ranges from -4.5 to 3.2; F ranges between 0.1-1.7. ..... 61

Figure 3.6 (A) Landform elements classification and (B) inter-LSB mask. In B, grey corresponds to the inter-LSB mask derived from the first landform elements classification and black represents the difference between that mask and processing loop 4 mask (mostly the result of the mathematical morphology filter – step 3 of LEMM processing flow). No saddle was mapped in this area. ..... 64

Figure 3.7 MM-footprints (A) and SAM-footprints (B-F). ..... 70

Figure 3.8 Inter-LSB mask and NHR derived from the original DTM (A and C, respectively) and from the preprocessed DTM (B and D, respectively). C and D vary between zero (dark blue) and one (red). Both A and B, and C and D were computed with the same parameters (the inter-LSB mask from the first loop in the LEMM processing flow and section 3.5.5, respectively). The original DTM was very noisy and neither A nor C would be adequate inputs for SAM. ..... 73

Figure 3.9 SAM-methods ratio of general detection to overdetection. ..... 74

Figure 3.10 Statistical distribution of SAM-footprints' (closed contours) NLR value. TPI and NHRC scales were normalized between 0-1. The relatively low values of TPI are related to TPI formula (i.e. mean, instead of minimum, elevation is the reference)..... 76

Figure 3.11 Mask (dark grey) of regions where LSBs do not occur or are much degraded..... 78

# Chapter 1. Introduction

## 1.1. Research rationale: Decoding longitudinal subglacial bedforms

Most warm-based glacier movement is related to processes at the ice-bed interface (Rignot et al., 2011); yet, in relation to the short time-span of the observational record and to the inaccessibility of present-day subglacial environments, these are not well constrained, introducing uncertainty into numerical models of ice sheet evolution and thus to projections of sea level change (Greenwood and Clark, 2009; Bartholomew et al., 2010). The paleoglaciological (morpho-sedimentary) record is spatially extensive and temporally comprehensive, readily accessible and easy to map, and can provide information at a detail which current numerical ice-sheet models are unable to resolve, but there is divergence on its glaciological significance and much remains to be done in terms of inventorying. While understanding the proxy value of this record is fundamental for paleoglaciological reconstructions, resolving past processes improves our ability to predict future changes to present-day glaciers; reconstructions of glacier geometry and dynamics associated with past periods of climate amelioration provide a basis for devising scenarios of future ice sheet evolution. On the other hand, observations from present-day glacial environments are fundamental for constraining the interpretation of relict features.

### 1.1.1. Longitudinal subglacial bedforms and their unexplained genesis

A particularly important characteristic of some glacial landforms is their morphological anisotropy. Formed at the ice-bed interface, transverse and longitudinal subglacial bedforms (LSBs) have their long axis consistently oriented (sub)perpendicular and (sub)parallel to ice flow vectors, respectively. This thesis focuses on positive-relief

LSBs, particularly drumlins and mega-scale glacial lineations (MSGLs) (Davis, 1884; Menzies, 1979a; Clark, 1993) (Figs 1.1, 1.2). These are very common at the footprints of past ice sheets (e.g., Prest et al., 1968; Hughes et al., 2010; found in ca. 70% of the previously glaciated area of Canada – Clark et al., 2009), occurring in spatial clusters of tens to tens of thousands of individuals (in drumlin fields) with positively spatially autocorrelated morphometry (Trenhaile, 1975; Aario, 1977; Francek, 1991; Smalley and Warburton, 1994; Stokes and Clark, 2002) and typically arranged in regular patterns (Clark, 2010). The distinction between drumlins and MSGLs has been based on shape and size, the latter being more elongate, longer and morphologically less varied than the first (Clark, 1993; Stokes and Clark., 2002; Clark et al., 2009). However, recent studies (Stokes et al., 2013; Spagnolo et al., 2014; Ely et al., 2014) indicate that, dimension-wise, drumlins and MSGLs are indivisible, underscoring the existence of a subglacial bedform continuum (Rose, 1987) and leading to the formulation of a common genetic model for both types of LSBs (Fowler and Chapwanya, 2014). Hereafter, the acronym LSBs refers to both drumlins and MSGLs.

Despite ca.180 years of research on the topic (since Bryce, 1833), LSB genesis is not yet fully understood, markedly different ideas still competing for its explanation. Proposed processes of drumlin and MSGL formation can be grouped into those that invoke meltwater and those that invoke ice as the main formative agent (Table 1.1). The first group is mainly attributed to Shaw and co-workers, who suggest that drumlins are formed during meltwater underbursts, but can be traced back to Bryce (1833) (drumlin formation by diluvial currents); the second group implicates the glacier bed deformation paradigm (e.g., Boulton and Hindmarsh, 1987) – that, in certain conditions (unconsolidated bed and high pore-water pressures), there may be a coupling between the glacier and its bed which results in the deformation and advection of the latter (mobile bed – till), with implications for glacier dynamics. Some hypotheses (*sensu lato*) of LSB genesis (Table 1.1, C and H; B with regard to drumlin composition, Stokes et al., 2011) attempt explaining the full range of LSB characteristics, whereas others focus on specific traits; for example, the ice-keel groove-ploughing hypothesis predicts (is fitted to) a downflow-decrease of MSGL amplitude (due to a progressive melting of the keels), which occurs in some MSGLs (Spagnolo et al., 2014). Mathematical modeling has been conducted in association with hypotheses B, F, G and I (Table 1.1); quantitative

predictions from these mostly refer to landform size and spacing (e.g., Fowler, 2009, 2010a,b). Predictions from hypotheses C and H about the shape and location of LSBs are supported by experimental (flume) and computational fluid dynamics studies (Shaw, 1996; Pollard et al., 1996; Wilhelm et al. 2003). The remaining hypotheses are more qualitative, conceptual models.

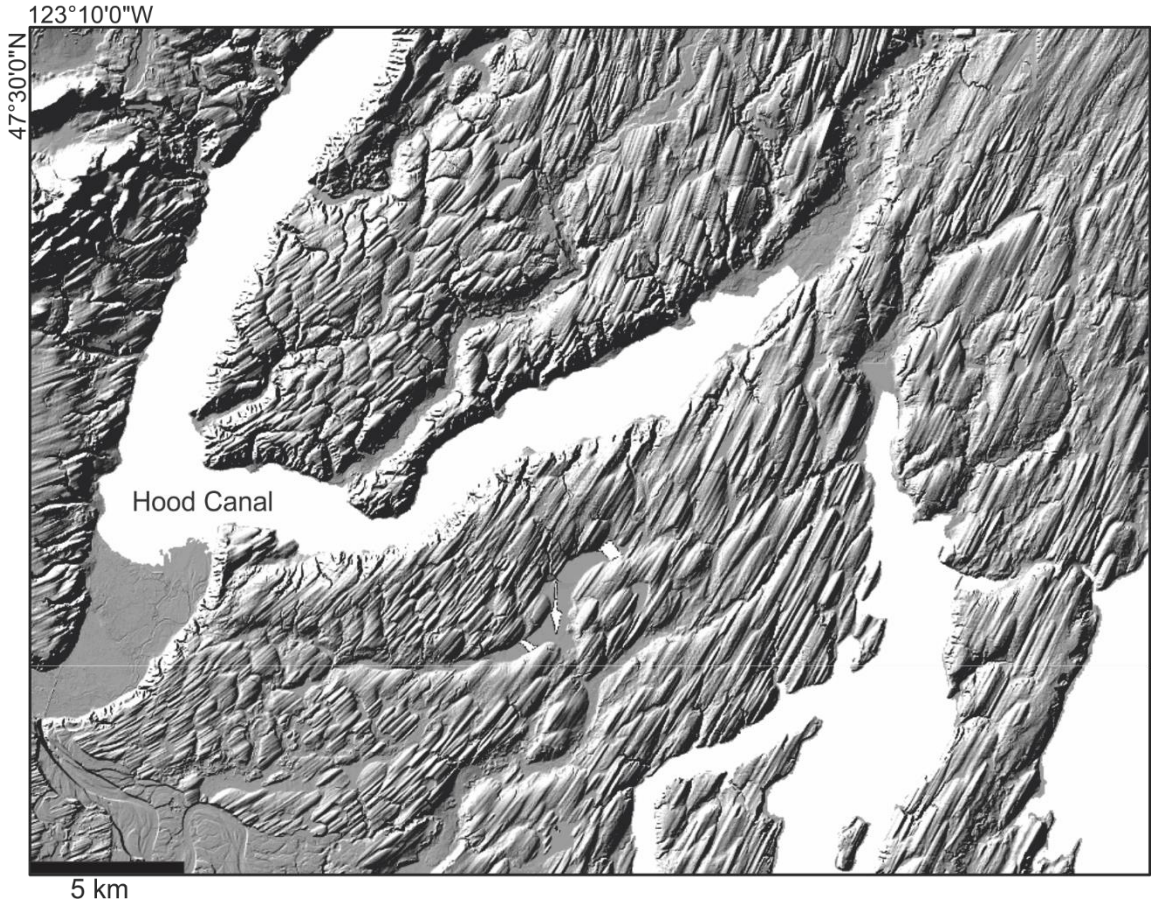


**Figure 1.1 Relict LSBs (mostly drumlins) in the Puget Lowland, WA, USA. Hillshaded terrain model derived from a 1.8 m cell-size DTM (http://pugetsoundlidar.ess. washington.edu/About_PSLC.htm).**

The success of a LSB genesis hypothesis is dependent on the ability of the proposed process(es) to explain the range of LSB morphometric (Shaw, 1983; Knight, 1997; Clark et al., 2009; Spagnolo et al., 2010, 2011, 2012; Spagnolo et al., 2014; Lamsters and Zelčs, 2014; Dowling et al., 2015) (Fig. 1.3) and compositional (Stokes et al., 2011 and Ó Cofaigh et al., 2013 for reviews) characteristics, as well as the variety of geomorphological settings in which LSBs occur (Menzies, 1979a; Patterson and Hooke,

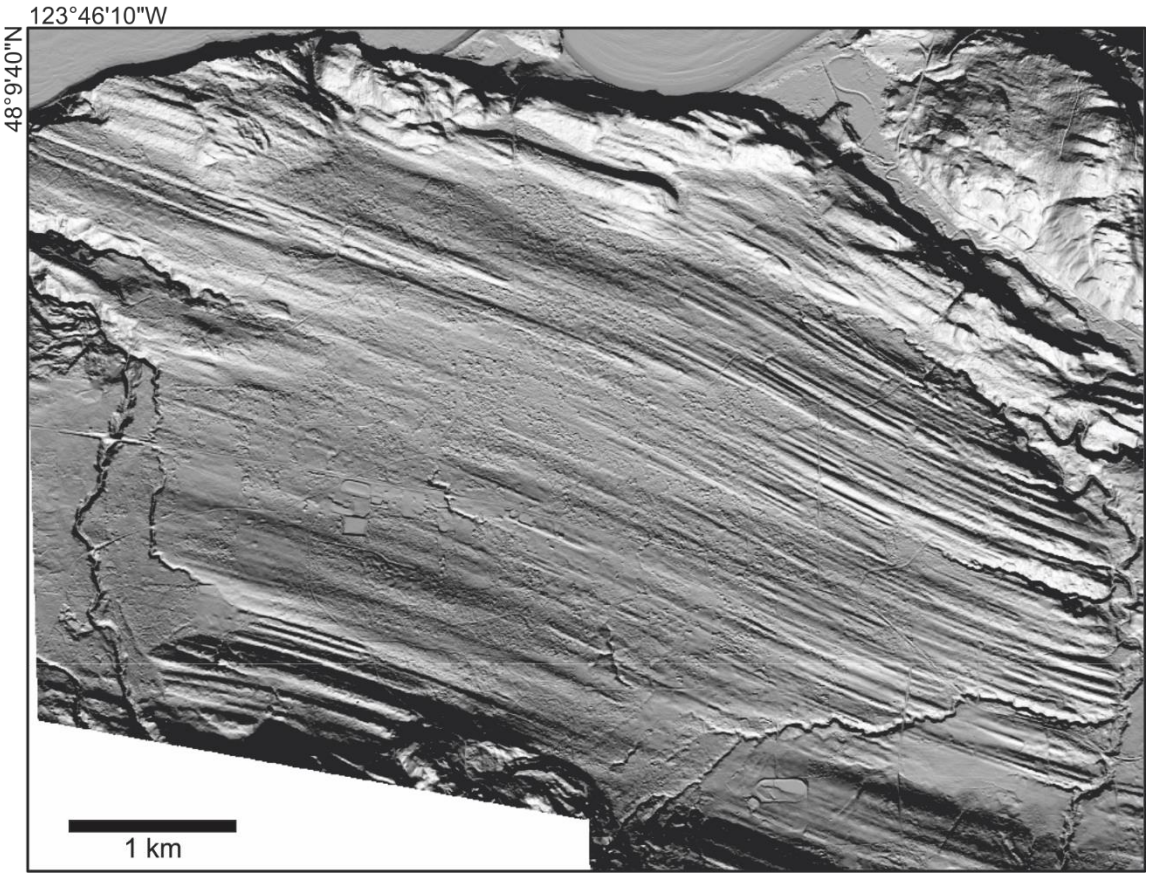


**Figure 1.2 Relict mega-scale glacial lineations at the south margin of the Juan de Fuca Straight west of the Puget Lowland, WA, USA. Hillshaded terrain model derived from a 1.8 m cell-size DTM (http://pugetsoundlidar.ess.washington.edu/About_PSLC.htm).**

1995). However, while LSB composition is well described (Stokes et al., 2011), existent morphometric data is limited, restricting hypothesis testing and development. The megaflood ideas (C and H) are particular in that they have been criticized mostly for the lack of evidence for the presence of subglacial meltwater reservoirs large enough to yield the outburst flow magnitudes necessary to conduct the implied geomorphic work (e.g., Benn and Evans, 2006), and not so much for the processes invoked. Stokes et al. (2013) tested predictions from MSGL formation hypotheses against a large morphometric dataset (17k MSGLs) and concluded that none of the existing hypotheses fits the range of inventoried characteristics, but also that the “rilling instability” hypothesis was not falsified. Spagnolo et al. (2014) assessed the “ice-keel groove-ploughing” and “rilling instability” hypotheses against the morphometry of 4k MSGLs from putative paleo

ice-streams in Canada, Norway and Antarctica, and from an active ice-stream in Antarctica, and concluded that neither fits the observed range of characteristics.

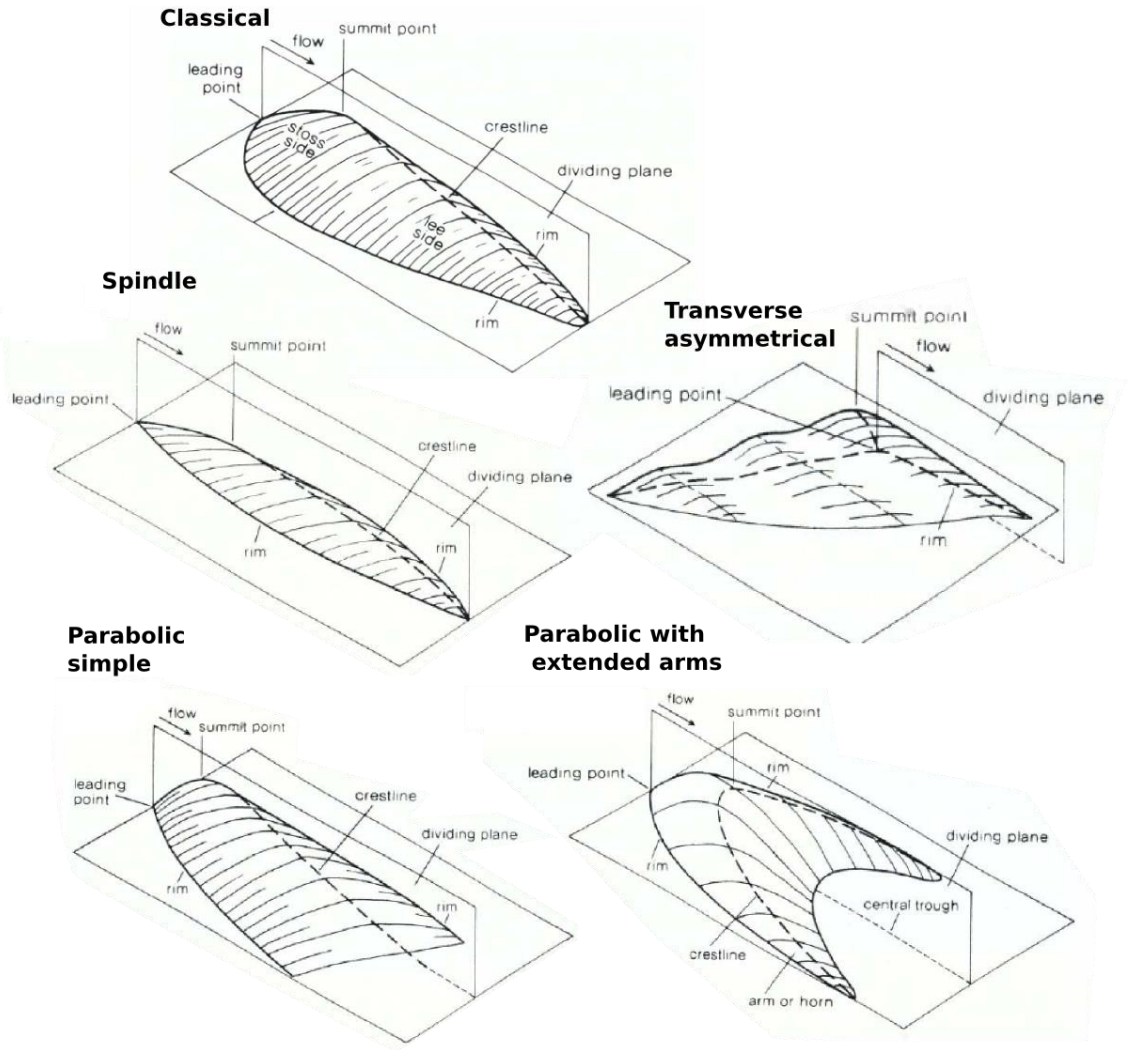


**Figure 1.3 Morphological drumlin types based on investigations in the Livingstone Lake drumlin field, Saskatchewan, Canada (modified from Shaw, 1983).**

## 1.1.2. Morphometric data: past and future

Before the 1990's to 2000's many descriptions of LSB shape were qualitative (e.g., Clapperton, 1989; Knight, 1997; Zelčs and Dreimanis, 1997); quantitative data were measured manually and pertained to small samples (tens to hundreds of landforms; e.g., Reed et al. 1962; Baranowski, 1969; Gravenor, 1974;

**Table 1.1 LSB formation hypotheses classified by formative agent**

| | Agent | Mechanism | Literature |
|---|---|---|---|
| Drumlins | Ice | A) Subglacial sediment deformation/deposition/erosion about an obstruction to till advection (e.g., topographic obstacle; "sticky spot" due to high substrate permeability) | Smalley and Unwin, 1968; Menzies, 1979b; Boulton, 1987; Hart, 1997 |
| | | B) Instability at the ice-deforming bed interface | Smalley and Warburton, 1994; Hindmarsh, 1998, 1999; Smalley et al., 2000; Fowler, 2000, 2009, 2010a; Fowler and Chapwanya, 2014 |
| | Water | C) Meltwater underburst a) deposition and/or b) erosion | a) Shaw, 1983, 1989; Shaw et al., 1989<br>b) Shaw and Sharpe, 1987; Shaw, 1989; Shaw et al., 1989<br>Shaw, 2002, 2010 |
| | | D) Sedimentation in lee-side water-filled cavities | Dardis et al., 1984 |
| MSGLs | Ice | E) Subglacial sediment deformation (attenuated drumlins) | Clark, 1993 |
| | | F) Ploughing of grooves in subglacial sediment by ice keels | Tulaczyk et al., 2001; Clark et al., 2003 |
| | | G) Spiral (turbulent) flow in basal ice | Schoof and Clarke, 2008 |
| | Water | H) Meltwater underburst | Munro-Stasiuk and Shaw, 2002; Shaw et al., 2008; Shaw, 2010; Shaw and Young, 2010; Lesemann et al., 2010* |
| | | I) Rilling instability in the basal hydraulic system | Fowler, 2010b |

* For "glacial curvilineations", which can be thought of as curved MSGLs

Crozier, 1975; Jauhiainen, 1975; Boots and Burns, 1984). With the evolution of computers and GIS and the increasing availability of high resolution satellite imagery and DEMs, analyses began being conducted for larger datasets (thousands to tens of thousands of LSBs) and with (semi-)automated methods (GIS) (Stokes and Clark, 2002; Kerr and Eyles, 2007; Hess and Briner, 2009; Clark et al., 2009; Greenwood and Clark, 2010; Spagnolo et al., 2010, 2011, 2012; Stokes et al., 2013; Spagnolo et al., 2014; Lamsters and Zelčs, 2014; Dowling et al., 2015), but typically for a limited number of properties and in 2D – mostly footprint length, width, elongation and longitudinal asymmetry. Data on LSB ridgeline planar shape, footprint transverse asymmetry, 3D morphometry, and spatial arrangement and autocorrelation are scarce. Spatial

arrangement (e.g., regular vs. random) is the most complex to quantify (due to fragmentation and palimpsesting of relict subglacial landscapes) and, since the mid-1980s, its quantitative analysis has received little attention (despite Hess and Briner, 2007; Maclachlan and Eyles, 2013). Drumlins are often described as being disposed in regular patterns, and such regularity is a core concept in theories of drumlin genesis (Clark, 2010), but with little quantitative basis. The insecurity of morphogenetic assumptions is highlighted by Spagnolo et al. (2010, 2011), who, based on the morphometry of 44.5k drumlins from northern Europe and North America, concluded that the long-established and widely used criteria for determining ice flow direction from drumlins (wider and steeper stoss side; tapering lee) is false.

At least as important as summarizing large datasets is to mine for morphometric types (sub-populations whose differences might be a function of distinct genetic conditions) and quantitatively describe previously reported morphological types (Fig. 1.3; e.g., Shaw, 1983; Knight, 1997). This has not been attempted and existing measures do not discriminate between categories of existing qualitative classifications (such as those in Fig. 1.3). Additionally, it is important to understand which aspects of LSB morphometry are determined by external factors (modulators of formation processes), 1) so that they are not wrongly used as direct glaciological proxies and 2) to constrain relationships between variables in LSB formation models, but this type of analyses is in its infancy (Maclachlan and Eyles, 2013). Several studies have linked variations in morphometry to environmental controls such as substrate properties (e.g., Miller 1972), topography (e.g., Trenhaile, 1975), sediment availability (e.g., Colgan and Mickelson, 1997), and mechanical properties of till (e.g., Rattas and Piotrowski, 2003), but only recently have these relationships been addressed statistically (Kerr and Eyles, 2007; Greenwood and Clark, 2010). However, the adequacy of inventorying methods should be addressed before proceeding to the analysis of new and more detailed morphometric attributes.

LSB mapping has been based on visual interpretation and manual digitization, a subjective and slow process which is difficult to reproduce, but little is known about the magnitude of inter-operator subjective differences, and published (semi-)automated mapping methods (designed for objectivity and speed) have not been highly successful.

On the other hand, previously used automated methods (GIS) for measuring LSB characteristics such as orientation, length and asymmetry based on mapped footprints have often been applied uncritically or with limited analysis of their adequacy. Both are low-level (pyramid) problems with implications for the robustness of existing morphometric data and derived conclusions, and thus should be addressed.

### 1.1.3. LSB morphometry in past paleoglaciological reconstructions

Despite our limited understanding of LSB genesis and the potential limitations of current morphometric data, LSB morphometry has been used to reconstruct ice flow direction and dynamics. Ice flow direction data is important not only for understanding glacial history, but also for practical applications in mineral exploration (e.g., Klassen and Thompson, 1993; Cummings et al., 2010). That LSBs are typically oriented (sub)parallel to ice flow is confirmed by other proxies, such as moraines, drift dispersal patterns and bedrock striae, and by imaging of present-day subglacial environments (King et al., 2007; Smith et al., 2007), and thus is well established (e.g., Davis, 1884; Alden, 1905; Knight, 2009; Stokes and Korteniemib, 2014). On the other hand, the long-established criteria for determining ice flow direction from drumlin shape (wider and steeper stoss side; tapering lee) may be false (Spagnolo et al., 2010, 2011).

LSB elongation has been causally linked to ice flow velocity, LSBs with higher length-width ratio forming under faster ice flow than less elongate LSBs (Clark, 1993; Stokes and Clark, 2002; King et al., 2009). This relationship has been invoked to identify and delineate paleo ice-streams (e.g., Margold et al., 2014), which are fast flowing (few hundreds of metres to 3 km $yr^{-1}$) streams of ice within ice sheets responsible for transferring large volumes of ice from accumulation to ablation zones, thus playing a dominant role in present-day ice sheet mass balance and in glacier-driven changes in eustatic sea level (Rignot, 2006; Shepherd and Wingham, 2007; Rignot et al., 2008).

## 1.2. Research objectives

The overarching goal of this thesis is to contribute to the testing and development of methods that can be used to produce a rich and robust LSB morphometric inventory

which, in turn, facilitates our ability to resolve LSB genesis and to reconstruct paleo glacier dynamics and evolution. Specifically, the objectives are:

1) to assess the adequacy of previously used automated morphometric measurement methods (GIS) in order to assess the robustness of current morphometric data and determine best practices; and

2) to develop a method for the semi-automated mapping of LSBs, as a solution to the subjectivity and slowness of manual mapping.

## 1.3. Thesis organization and authorship

This thesis is composed of 2 research articles (chapters 2 and 3), each addressing one of the objectives (1 and 2, respectively). The research articles are co-authored by myself (first author) and my Senior Supervisor (Tracy A. Brennand). I performed all the analyses and prepared the manuscripts. TAB contributed to research problem and method definition and accompanying analyses, promoted discussions on preliminary results and thoroughly reviewed the manuscripts in an iterative process with me, leading to significant improvements over the original versions.

Chapter 2 evaluates the adequacy of previously used methods and of a new method for the computation of LSB orientation, length and longitudinal asymmetry from LSB footprints. Tests are conducted using a sample of 100 LSBs representing the shape and size range of LSBs in the Puget Lowland Drumlin Field (Goldstein, 1994), WA, USA. Chapter 3 is a comparative study of two new methods (object-based) for the semi-automated mapping of LSBs from digital terrain models (DTMs). One method (normalized closed contour method, NCCM) is based on the identification of normalized local relief closed contour-bounded terrain segments with LSB-like morphometry; the other (land-form elements mask method, LEMM) involves classifying the DTM into land-form elements, masking out elements rare to absent in LSBs and identifying terrain segments with LSB-like morphometry out of the remaining areas. Both are based on a ruleset encapsulating expert knowledge, published morphometric data and the

morphometric range of LSBs in the study area. These methods are tested on a 139.5 $km^2$ test area in the Puget Lowland drumlin field.

## 1.4. Additional work

Earlier goals for my MSc research were to develop a richer array of morphometric measures (e.g., transverse asymmetry) and inventory the LSBs of the Puget Lowland drumlin field, WA, USA in order to assess the dependency of LSB morphometry on factors such as lithology (composition) and topography. It was while trying to map and measure LSBs using previously used methods that I realized that there were problems with the latter and thus uncertainties in the quality of previously collected data. In consultation with my supervisors, this led to a change in the research objectives – a refocusing on method development and assessment. This shelved work produced three products that are included in the appendices.

1) An integrated terrain model of a large part of the Puget Lowland drumlin field which brings together elevation and bathymetric data (Appendix A). This was to be used as a foundational dataset for manual and semi-automated mapping.

2) A manually mapped map of LSBs for part of the Puget Lowland drumlin field (Appendix B). Much of this mapping was conducted by undergraduate students in the SFU Work-Study Program, namely by Valerie Zhang and Suzann Rowden, whose dedication is much appreciated. The LSB dataset used in chapter 2 is included in the map and was mapped by myself.

3) A map of the location of sedimentary exposures visited during 15 days of field-work in the Puget Lowland (Appendix C). These sites were visited in order to obtain insights on LSB composition.

## 1.5. References

Aario, R., 1977. Associations of flutings, drumlins, hummocks and transverse ridges. GeoJournal 1(6), 65-72.

Alden, W. C., 1905. The drumlins of southeastern Wisconsin. U.S. Geological Survey Bulletin 273, 9-43.

Baranowski, S., 1969. Some remarks on the origin of drumlins. Geographia Polonica 17,197-208.

Bartholomew, I., Nienow, P., Mair, D., Hubbard, A., King, M. A., Sole, A., 2010. Seasonal evolution of subglacial drainage and acceleration in a Greenland outlet glacier. Nature Geoscience 3(6), 408-411.

Benn, D. I., Evans, D. J., 2006. Subglacial megafloods: outrageous hypothesis or just outrageous?. In: Knight, P. G. (Ed.), Glacier science and environmental change. Blackwell Publishing Ltd, pp. 42-50.

Boots, B. N., Burns, R. K., 1984. Analyzing the spatial distribution of drumlins: a two-phase mosaic approach. Journal of Glaciology 30(106), 302-307.

Boulton, G. S., 1987. A theory of drumlin formation by subglacial sediment deformation. In: Menzies, J., Rose, J. (Eds), Drumlin Symposium. Balkema, Rotterdam, pp. 103-116.

Boulton, G. S., Hindmarsh, R. C. A., 1987. Sediment deformation beneath glaciers: rheology and geological consequences. Journal of Geophysical Research: Solid Earth (1978–2012) 92(B9), 9059-9082.

Bryce, J., 1833. On the evidences of diluvial action in the north of Ireland. J. R. Geol. Soc. Dublin 1, 34–44.

Clapperton, C. M., 1989. Asymmetrical drumlins in Patagonia, Chile. Sedimentary Geology 62(2), 387-398.

Clark, C. D., 1993. Mega-scale glacial lineations and cross-cutting ice-flow landforms. Earth Surface Processes and Landforms 18(1), 1-29.

Clark, C. D., 2010. Emergent drumlins and their clones: from till dilatancy to flow instabilities. Journal of Glaciology 56(200), 1011-1025.

Clark, C. D., Tulaczyk, S. M., Stokes, C. R., Canals, M., 2003. A groove-ploughing theory for the production of mega-scale glacial lineations, and implications for ice-stream mechanics. Journal of Glaciology 49(165), 240-256.

Clark, C. D., Hughes, A. L., Greenwood, S. L., Spagnolo, M., Ng, F. S., 2009. Size and shape characteristics of drumlins, derived from a large sample, and associated scaling laws. Quaternary Science Reviews 28(7), 677-692.

Colgan, P. M., Mickelson, D. M., 1997. Genesis of streamlined landforms and flow history of the Green Bay lobe, Wisconsin, USA. Sedimentary Geology 111(1), 7-25.

Crozier, M. J., 1975. On the origin of the Peterborough drumlin field: testing the dilatancy theory. The Canadian Geographer/Le Géographe canadien 19(3), 181-195.

Cummings, D. I., Russell, H. A. J., Sharpe, D. R., Kjarsgaard, B. A., 2010. Eskers as mineral exploration tools: a review. Earth-Science Reviews 109(1-2), 32-43.

Dardis, G. F., McCabe, A. M., Mitchell, W. I., 1984. Characteristics and origins of lee-side stratification sequences in late pleistocene drumlins, northern Ireland. Earth Surface Processes and Landforms 9(5), 409-424.

Davis, W.M., 1884. Drumlins. Science 4, 418–420.

Dowling, T. P.F., Spagnolo, M., Möller, P., 2015. Morphometry and core type of streamlined bedforms in southern Sweden from high resolution LiDAR. Geomorphology (accepted manuscript).

Ely, J. C., Clark, C. D., Spagnolo, M., Stokes, C. R., Greenwood, S. L., Hughes, A. L., Dunlop, P., Hess, D., 2014. Demonstration of a subglacial bedform continuum: Is a unifying formation theory required?. EGU General Assembly Conference Abstracts 16, p. 5533.

Fowler, A. C., 2000. An instability mechanism for drumlin formation. Geological Society, London, Special Publications 176(1), 307-319.

Fowler, A. C., 2009. Instability modelling of drumlin formation incorporating lee-side cavity growth. Proceedings of the Royal Society A: Mathematical, Physical and Engineering Science 465(2109), 2681-2702.

Fowler, A. C., 2010a. The instability theory of drumlin formation applied to Newtonian viscous ice of finite depth. Proceedings of the Royal Society A: Mathematical, Physical and Engineering Science 466(2121), 2673-2694.

Fowler, A. C., 2010b. The formation of subglacial streams and mega-scale glacial lineations. Proceedings of the Royal Society A: Mathematical, Physical and Engineering Science 466(2123), 3181-3201.

Fowler, A. C., Chapwanya, M., 2014. An instability theory for the formation of ribbed moraine, drumlins and mega-scale glacial lineations. Proceedings of the Royal Society A: Mathematical, Physical and Engineering Science 470, 20140185.

Francek, M. A., 1991. A spatial perspective on the New York drumlin field. Physical Geography 12(1), 1-18.

Gravenor, C. P., 1974. The Yarmouth drumlin field, Nova Scotia, Canada. Journal of Glaciology 13(67), 45-54.

Greenwood, S. L., Clark, C. D., 2009. Reconstructing the last Irish Ice Sheet 2: a geomorphologically-driven model of ice sheet growth, retreat and dynamics. Quaternary Science Reviews 28(27), 3101-3123.

Greenwood, S. L., Clark, C. D., 2010. The sensitivity of subglacial bedform size and distribution to substrate lithological control. Sedimentary Geology 232(3), 130-144.

Hart, J. K., 1997. The relationship between drumlins and other forms of subglacial glaciotectonic deformation. Quaternary Science Reviews, 16(1), 93-107.

Hess, D. P., Briner, J. P., 2009. Geospatial analysis of controls on subglacial bedform morphometry in the New York Drumlin Field – implications for Laurentide Ice Sheet dynamics. Earth Surface Processes and Landforms, 34(8), 1126-1135.

Hindmarsh, R. C., 1998. The stability of a viscous till sheet coupled with ice flow, considered at wavelengths less than the ice thickness. Journal of Glaciology 44(147), 285-292

Hindmarsh, R. C., 1999. Coupled ice–till dynamics and the seeding of drumlins and bedrock forms. Annals of Glaciology 28(1), 221-230.

Hughes, A. L., Clark, C. D., Jordan, C. J., 2010. Subglacial bedforms of the last British Ice Sheet. Journal of Maps 6(1), 543-563.

Jauhiainen, F., 1975. Morphometric analysis of drumlin fields in northern Central Europe. Boreas 4(4), 219-230.

Kerr, M., Eyles, N., 2007. Origin of drumlins on the floor of Lake Ontario and in upper New York State. Sedimentary Geology 193(1), 7-20.

King, E. C., Woodward, J., Smith, A. M., 2007. Seismic and radar observations of subglacial bed forms beneath the onset zone of Rutford Ice Stream, Antarctica. Journal of Glaciology 53(183), 665-672.

King, E. C., Hindmarsh, R. C., Stokes, C. R., 2009. Formation of mega-scale glacial lineations observed beneath a West Antarctic ice stream. Nature Geoscience 2(8), 585-588.

Klassen, R. A., Thompson, F. J., 1993. Glacial history, drift composition, and mineral exploration, central Labrador. Geological Survey of Canada Bulletin 435.

Knight, J., 1997. Morphological and morphometric analyses of drumlin bedforms in the Omagh Basin, north central Ireland. Geografiska Annaler: Series A, Physical Geography 79(4), 255-266.

Knight, P. G., 2009. Drumlins. In: Gornitz, V. (Ed.), Encyclopedia of paleoclimatology and ancient environments. Springer, The Netherlands, pp.284-284.

Lamsters, K., Zelčs, V., 2014. Subglacial bedforms of the Zemgale Ice Lobe, south-eastern Baltic. Quaternary International (in press).

Lesemann, J. E., Piotrowski, J. A., Wysota, W. 2010. "Glacial curvilineations": New glacial landforms produced by longitudinal vortices in subglacial meltwater flows. Geomorphology 120(3), 153-161.

Maclachlan, J. C., Eyles, C. H., 2013. Quantitative geomorphological analysis of drumlins in the Peterborough drumlin field, Ontario, Canada. Geografiska Annaler: Series A, Physical Geography 95(2), 125-144.

Margold, M., Stokes, C. R., Clark, C. D., Kleman, J., 2014. Ice streams in the Laurentide Ice Sheet: a new mapping inventory. Journal of Maps (ahead-of-print), 1-16.

Menzies, J., 1979a. A review of the literature on the formation and location of drumlins. Earth-Science Reviews 14(4), 315-359.

Menzies, J., 1979b. The mechanics of drumlin formation with particular reference to the change in pore-water content of the till. Journal of Glaciology 22, 373-384.

Miller, J. W., 1972. Variations in New York Drumlins. Annals of the Association of American Geographers 62(3), 418-423.

Munro-Stasiuk, M. J., Shaw, J., 2002. The Blackspring Ridge Flute Field, south-central Alberta, Canada: evidence for subglacial sheetflow erosion. Quaternary International 90(1), 75-86.

Ó Cofaigh, C., Stokes, C. R., Lian, O. B., Clark, C. D., Tulacyzk, S., 2013. Formation of mega-scale glacial lineations on the Dubawnt Lake Ice Stream bed: 2. Sedimentology and stratigraphy. Quaternary Science Reviews 77, 210-227.

Patterson, C. J., Hooke, R. LeB., 1995. Physical environment of drumlin formation. Journal of Glaciology 41, 30–38.

Pollard A, WaKarini N, Shaw J. 1996. Genesis and morphology of erosional shapes associated with turbulent flow over a forward-facing step. In: Ashworth P,Bennett SJ, Best JL, McLelland SJ (Eds), Coherent Flow Structure in Open Channels. Chichester, Wiley, pp. 249–266.

Prest, V. K., Grant, D. R., Rampton, V. N., 1968. Glacial map of Canada. Geological Survey of Canada, "A" Series Map.

Rattas, M., Piotrowski, J. A., 2003. Influence of bedrock permeability and till grain size on the formation of the Saadjärve drumlin field, Estonia, under an east-Baltic Weichselian ice stream. Boreas 32(1), 167-177.

Reed, B., Galvin, C. J., Miller, J. P. 1962. Some aspects of drumlin geometry. American Journal of Science 260(3), 200-210.

Rignot, E., 2006. Changes in ice dynamics and mass balance of the Antarctic ice sheet. Philosophical Transactions of the Royal Society A: Mathematical, Physical and Engineering Sciences 364(1844), 1637-1655.

Rignot, E., Bamber, J. L., Van Den Broeke, M. R., Davis, C., Li, Y., Van De Berg, W. J., Van Meijgaard, E., 2008. Recent Antarctic ice mass loss from radar interferometry and regional climate modelling. Nature Geoscience 1(2), 106-110.

Rignot, E., Mouginot, J., Scheuchl, B., 2011. Ice flow of the Antarctic ice sheet. Science 333(6048), 1427-1430.

Rose, J., 1987. Drumlins as part of a glacier bedform continuum. In: Menzies, J., Rose, J. (Eds), Drumlin Symposium. Balkema, Rotterdam, pp. 103-116.

Schoof, C. G., Clarke, G. K., 2008. A model for spiral flows in basal ice and the formation of subglacial flutes based on a Reiner-Rivlin rheology for glacial ice. Journal of Geophysical Research: Solid Earth 113(B5).

Shaw, J., 1983. Drumlin formation related to inverted melt-water erosional marks. Journal of Glaciology 29(103), 461-479.

Shaw, J., 1989. Drumlins, subglacial meltwater floods, and ocean responses. Geology 17(9), 853-856.

Shaw, J., 1996. A meltwater model for Laurentide subglacial landscapes. In: McCann, S. B., Ford, D.C. (Eds), Geomorphologie sans Frontières. John Wiley, Chichester, pp. 181-236.

Shaw, J., 2002. The meltwater hypothesis for subglacial bedforms. Quaternary International 90(1), 5-22.

Shaw, J., 2010. In defence of the meltwater (megaflood) hypothesis for the formation of subglacial bedform fields. Journal of Quaternary Science 25(3), 249-260.

Shaw, J., Sharpe, D. R., 1987. Drumlin formation by subglacial meltwater erosion. Canadian Journal of Earth Sciences 24(11), 2316-2322.

Shaw, J., Young, R. R., 2010. Reply to comment by Ó Cofaigh, Dowdeswell, King, Anderson, Clark, DJA Evans, J. Evans, Hindmarsh, Lardner and Stokes "Comments on Shaw, J., Pugin, A., Young, R.,(2009): A meltwater origin for Antarctic Shelf bedforms with special attention to megalineations." Geomorphology 102, 364-375. Geomorphology 117, 199-201.

Shaw, J., Kvill, D., Rains, B., 1989. Drumlins and catastrophic subglacial floods. Sedimentary Geology 62(2), 177-202.

Shaw, J., Pugin, A., Young, R. R., 2008. A meltwater origin for Antarctic shelf bedforms with special attention to megalineations. Geomorphology 102(3), 364-375.

Shepherd, A., Wingham, D., 2007. Recent sea-level contributions of the Antarctic and Greenland ice sheets. Science 315(5818), 1529-1532.

Smalley, I. J., Unwin, D. J., 1968. The formation and shape of drumlins and their distribution and orientation in drumlin fields. Journal of Glaciology 7, 377-390.

Smalley, I., Warburton, J., 1994. The shape of drumlins, their distribution in drumlin fields, and the nature of the sub-ice shaping forces. Sedimentary geology 91(1), 241-252.

Smalley, I. J., Lu, P., Jefferson, I. F., 2000. The golf-ball model and the purpose of drumlin formation. Studia Quaternaria 17, 29-33.

Smith, A. M., Murray, T., Nicholls, K. W., Makinson, K., Aðalgeirsdóttir, G., Behar, A. E., Vaughan, D. G., 2007. Rapid erosion, drumlin formation, and changing hydrology beneath an Antarctic ice stream. Geology 35(2), 127-130.

Spagnolo, M., Clark, C. D., Hughes, A. L., Dunlop, P., Stokes, C. R., 2010. The planar shape of drumlins. Sedimentary Geology 232(3), 119-129.

Spagnolo, M., Clark, C. D., Hughes, A. L., Dunlop, P., 2011. The topography of drumlins; assessing their long profile shape. Earth Surface Processes and Landforms 36(6), 790-804.

Spagnolo, M., Clark, C. D., Hughes, A. L., 2012. Drumlin relief. Geomorphology 153, 179-191.

Spagnolo, M., Clark, C. D., Ely, J. C., Stokes, C. R., Anderson, J. B., Andreassen, K., Graham, A. G. C., King, E., 2014. Size, shape and spatial arrangement of mega-scale glacial lineations from a large and diverse dataset. Earth Surface Processes and Landforms 39(11), 1432-1448.

Stokes, C. R., Clark, C. D., 2002. Are long subglacial bedforms indicative of fast ice flow?. Boreas 31(3), 239-249.

Stokes C.R., Korteniemi J., 2015. Drumlin. In: Kereszturi, A., Hargitai, H. (Eds), Encyclopedia of Planetary Landforms. Springer New York, Chapter 161.

Stokes, C. R., Spagnolo, M., Clark, C. D., 2011. The composition and internal structure of drumlins: Complexity, commonality, and implications for a unifying theory of their formation. Earth-Science Reviews 107(3), 398-422.

Stokes, C. R., Spagnolo, M., Clark, C. D., Ó Cofaigh, C., Lian, O. B., Dunstone, R. B. 2013. Formation of mega-scale glacial lineations on the Dubawnt Lake Ice Stream bed: 1. size, shape and spacing from a large remote sensing dataset. Quaternary Science Reviews 77, 190-209.

Trenhaile, A. S., 1975. The morphology of a drumlin field. Annals of the Association of American Geographers 65(2), 297-312.

Tulaczyk, S. M., Scherer, R. P., Clark, C. D., 2001. A ploughing model for the origin of weak tills beneath ice streams: a qualitative treatment. Quaternary International 86(1), 59-70.

Wilhelm D, Hartel C, Kleiser L., 2003. Computational analysis of two dimensional–three-dimensional transition in forward-facing step flow. Journal of Fluid Mechanics 489, 1–27.

Zelčs, V., Dreimanis, A., 1997. Morphology, internal structure and genesis of the Burtnieks drumlin field, Northern Vidzeme, Latvia. Sedimentary Geology 111(1), 73-90.

# Chapter 2.

# Measuring subglacial bedform orientation, length and asymmetry – method accuracy[1]

## 2.1. Highlights

1. Several methods for computing bedform orientation, length and asymmetry, including a new method based on the standard deviational ellipse (SDE), are tested.

2. Method performance is dependent on footprint shape.

3. The use of elliptical length should be discontinued.

4. For elongation (E) >5, errors are negligible for most methods.

5. For E <5, SDE data was relatively independent of footprint shape and is preferred.

## 2.2. Abstract

This study is an assessment of previously reported automated methods and of a new method for measuring longitudinal subglacial bedform (LSB) morphometry. It evaluates the adequacy (accuracy and precision) of orientation, length and longitudinal asymmetry data derived from the longest straight line (LSL) fitting the LSB's footprint, the footprint's

[1] A version of this chapter is in preparation for submission to the journal Geomorphology as: Jorge, M.G. & Brennand, T.A. Measuring subglacial bedform orientation, length and asymmetry – method accuracy.

minimum bounding rectangle longitudinal axis (RLA) and the footprint's standard deviational ellipse (SDE) longitudinal axis (LA) (new method), and the accuracy of length based on an ellipse fitted to the area and perimeter of the footprint (elliptical length). Tests are based on 100 manually mapped drumlins and mega-scale glacial lineations representing the size and shape range of LSBs in the Puget Lowland drumlin field, WA, USA. Data from manually drawn LAs are used as reference for method evaluation. With the exception of elliptical length, errors decrease rapidly with increasing footprint elongation (decreasing potential angular divergence between LAs). For LSBs with elongation <5 and excluding the 5% largest errors (outliers) ($n$ = 60), 1) the LSL, RLA and SDE methods had very small mean absolute error (MAE) in all measures (e.g., MAE <5º in orientation and <5 m in length); they can be confidently used to characterize the central tendency of LSB samples. 2) When analyzing data spatially, the LSL method should be avoided for orientation (36% of the errors were larger than 5º). 3) Elliptical length was the least accurate of all methods (MAE of 56.1 m and 15% of the errors larger than 5%); its use should be discontinued. 4) The relative adequacy of the LSL and RLA depends on footprint shape; SDE computed with the footprint's structural vertices is relatively shape-independent and is the preferred method. These conclusions are useful also for research on fluvial and aeolian bedform morphometry.

Keywords: drumlin; mega-scale glacial lineation; morphometry; longitudinal axis; orientation; method

## 2.3. **Introduction**

Landforms and sediment within the deglaciated footprints of former glaciers record paleo glacier geometry and dynamics (e.g., Stokes et al., 2011). A particularly important property of some glacial landforms is their morphological anisotropy. Transverse and longitudinal subglacial bedforms (LSBs) have their long axis typically oriented (sub)perpendicular and (sub)parallel to ice-flow vectors, respectively. Both types are very common within the footprints of past ice-sheets (e.g., Prest et al., 1968; Hughes et al., 2010). This study deals with positive-relief LSBs, particularly drumlins and mega-scale glacial lineations (Davis, 1884; Menzies, 1979; Clark, 1993). Differentiation between the two has been based on shape, size and spatiality: mega-lineations are

more elongate, longer and morphologically less varied than drumlins and tend to form parallel ridge-groove corrugations (Clark, 1993; Stokes and Clark, 2002; Clark et al., 2009; Clark, 2010). More recent studies (Stokes et al., 2013; Spagnolo et al., 2014; Ely et al., 2014) indicate that, dimension-wise these two landforms are indivisible, substantiating the claim of a subglacial bedform continuum (Rose, 1987). Hereafter the acronym LSBs is used to refer to both drumlins and mega-scale glacial lineations.

LSB genesis is disputed (e.g., compare Shaw, 2002; Clark et al., 2003; Schoof and Clarke, 2008; Hooke and Medford, 2013; Fowler and Chapwanya, 2014). Gaps (e.g., transverse asymmetry, 3D morphometry) and uncertainties (e.g., measurement method adequacy; sample representativeness) in the current morphometric data present limitations to testing hypotheses of LSB genesis. Existing geospatial data (DEMs and imagery from space-borne sensors) and software (GIS) provide the opportunity to improve the morphometric inventory, but, first, the adequacy of measurement methods must be assessed. Some previously reported methods have been applied uncritically or with limited assessment of potential bias; if method adequacy is not evaluated and bias is limiting, error will tend to accumulate both as new studies apply the same methods and as more complex measures are devised.

This study assesses the adequacy of previously reported automated methods and a new method for deriving LSB orientation, length and longitudinal asymmetry from LSB footprints. Measuring these properties requires determining a longitudinal axis. Inaccuracies in the axis' orientation propagate onto the quantification of length and longitudinal asymmetry. Tests are conducted on the accuracy and precision of orientation, length and longitudinal asymmetry computed based on the 1) longest straight line fitting LSB footprints (Spagnolo et al., 2010; Maclachlan and Eyles, 2013), 2) footprints' standard deviational ellipse (Lefever, 1926) (new method) and 3) footprints' minimum bounding rectangle (Napieralski and Nalepa, 2010; Dowling et al., 2015), and the accuracy of length based on an ellipse fitted to the area and perimeter of footprints (Clark et al. 2009; Lamsters, 2012; Spagnolo et al., 2014; Lamster and Zelčs, 2014). These methods are applied to 100 manually mapped drumlins and mega-scale glacial lineations representing the size and shape range of LSBs in the Puget Lowland Drumlin

Field (Goldstein, 1994), WA, USA and the accuracy of derived morphometric data is determined in relation to data based on a manually drawn longitudinal axis.

## 2.4. Prior work

Clark et al. (2009) used the a- and b-axes of ellipses defined based on the area and perimeter of footprints using Euler's approximation for deriving the length and width of 37k drumlins from Great Britain. They justified the adequacy of the method (hereafter referred to as elliptical length) based on a coefficient of determination ($r^2$) of 0.9991 between manually measured and automatically derived lengths from 100 drumlins. However, $r^2$ is a limited statistic. For example, consider two paired lists of 10 values, one ranging between 100-550 (intervals of 50) and the other between 100-1000 (intervals of 100); while their $r^2$ would be 1, the mean difference between the pairs of values would be 225.

Following Clark et al. (2009), later studies applied the same method uncritically. Lamsters (2012) computed the elliptical length and width of 880 drumlins from Latvia and, like Clark et al. (2009), justified method adequacy based on the correlation to 100 manually measured lengths (Spearman's coefficient of 0.98 for length and 0.93 for width). Euler's approximation was also used by Spagnolo et al. (2014), who analysed 1929 mega-scale glacial lineations from putative paleo ice-streams in northwestern Canada, and by Lamsters and Zelčs (2014), for 4400 LSBs from Latvia and Lithuania.

Spagnolo et al. (2010, 2011) analyzed longitudinal (a)symmetry for a very large sample of drumlins (44.5k) from northern Europe and North America based on the longest straight line (LSL) fitting inside the footprints. Spagnolo et al. (2010) focused on planar asymmetry and Spagnolo et al. (2011) on the longitudinal topographic profile. Spagnolo et al. (2010) did not assess potential bias – is LSL a good representation of footprints' longitudinal axis as manually drawn by an expert? Spagnolo et al. (2011) assessed two potential sources of bias: 1) LSL not passing through the summit of the drumlin; 2) LSL being shorter than a manually draw profile for slightly curving drumlins. The first was assessed by comparing the relative longitudinal position (RLP) of the highest point on the LSL profile (after Harry and Trenhaile, 1971) to the RLP of the true

summit based on Euclidean distances to the upflow and downflow ends (validation data) – errors exceeded 9.4% for 20% of the drumlins and the average absolute error was 6%. It is important to note that, because drumlin up and downflow ends may be transversally misaligned, the Euclidean distances up and downflow of the summit may correspond to different vectors. Bias related to differences in length between the LSL and the ridgeline was assessed by comparing the RLP of the highest point on LSL to the RLP of the summit on a manually drawn ridgeline for 100 drumlins – errors were larger than 10% for 15% of the drumlins and the average absolute error was 6%. In both cases, the authors concluded that the differences were not significant. Following Spagnolo et al. (2010, 2011), Maclachlan and Eyles (2013) used LSL to compute both length and longitudinal asymmetry for 812 drumlins in southern Ontario, Canada.

Dowling et al. (2015), following Napieralski and Nalepa (2010) (a study on the influence of DTM resolution on derived morphometrics), used footprints' minimum bounding rectangle for deriving the length, width (rectangle length, width) and elongation (ratio of length to width) for 10,311 LSBs from southern Sweden. Potential bias was not discussed.

These examples illustrate the need to properly assess method adequacy whenever a method is applied for the first time. The application of specific methods can increase exponentially as new inventories are conducted using previous methods.

## 2.5. **Methodology**

Defining a flow vector for LSB footprints is not straightforward and may require expert arbitration, but is important when building the morphometric inventory necessary to test hypotheses of LSB genesis. LSB footprints often lack axes of symmetry (they are transversally and longitudinally asymmetric), and can be best fitted by, or resemble, a variety of shapes, from ellipses and half-lemniscates to rectangles and parabolic and hyperbolic curves. Therefore, the orientation, length and longitudinal asymmetry measurement methods are assessed using a morphometrically diverse LSB sample. Tests are based on a manually mapped dataset of 100 LSBs (footprints, polygons) representing the shape and size range of LSBs in the Puget Lowland Drumlin Field

(Goldstein, 1994), WA, USA and a manually drawn longitudinal axis (LA) for these footprints. Previously reported methods are evaluated by comparing the data obtained from them to data from the manual LA (reference data). Figure 2.1 shows the workflow used to derive the morphometric database.

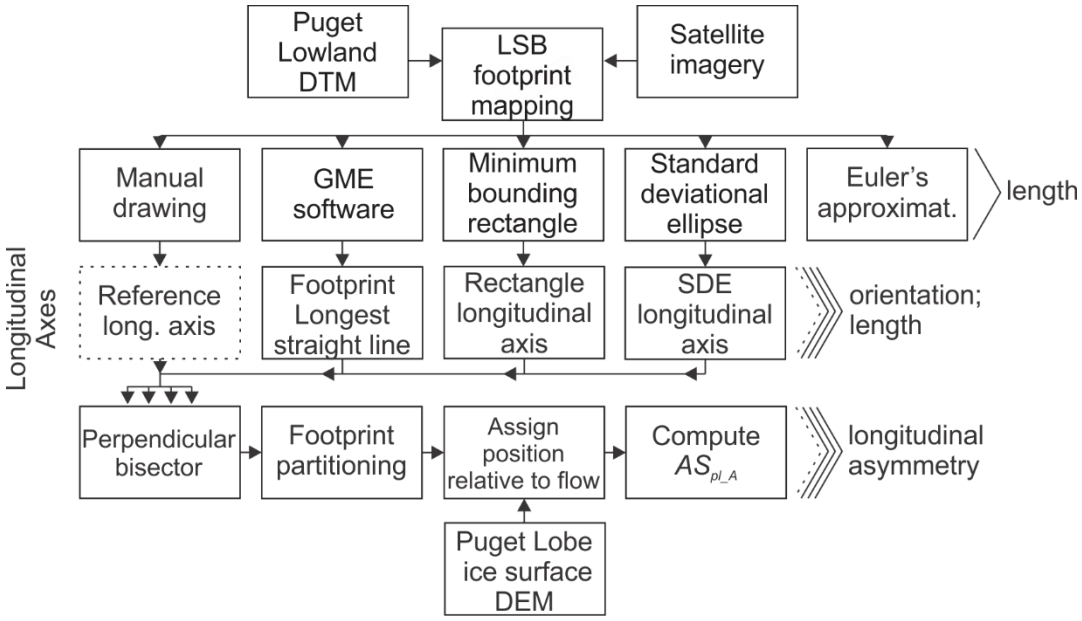


**Figure 2.1 Derivation of the morphometric database for method evaluation. LSB = longitudinal subglacial bedform; DTM = digital terrain model; GME = Geospatial Modeling Environment (Beyer, 2012); SDE = standard deviational ellipse (Lefever, 1926); DEM = digital elevation model; $AS_{pl\_A}$: the ratio between the footprints' upflow area and total area (Spagnolo et al., 2010).**

### 2.5.1. LSB mapping

LSB mapping was based on a 1.8 m cell-size digital terrain model (DTM; NDEP, 2004) with vertical resolution <1 m prepared by the Puget Lowland LiDAR Consortium (http://pugetsoundlidar.ess.washington.edu/About_PSLC.htm) and on the break-of-slope criterion (LSBs are essentially bounded by concave breaks in slope gradient – Evans, 2012). LSB footprint polygons (Fig. 2.2) were manually mapped within a GIS (ArcMap®) by inspecting a zenith-hillshaded terrain model overlain with 1 m-interval contours and a semi-transparent, display extent-adaptive color rendering of the DTM. ArcMap was used because it allows automatic display-extent adaptive rendering. The dataset is composed of 100 LSBs (Table 2.1), but with much redundancy in terms of shape and size.

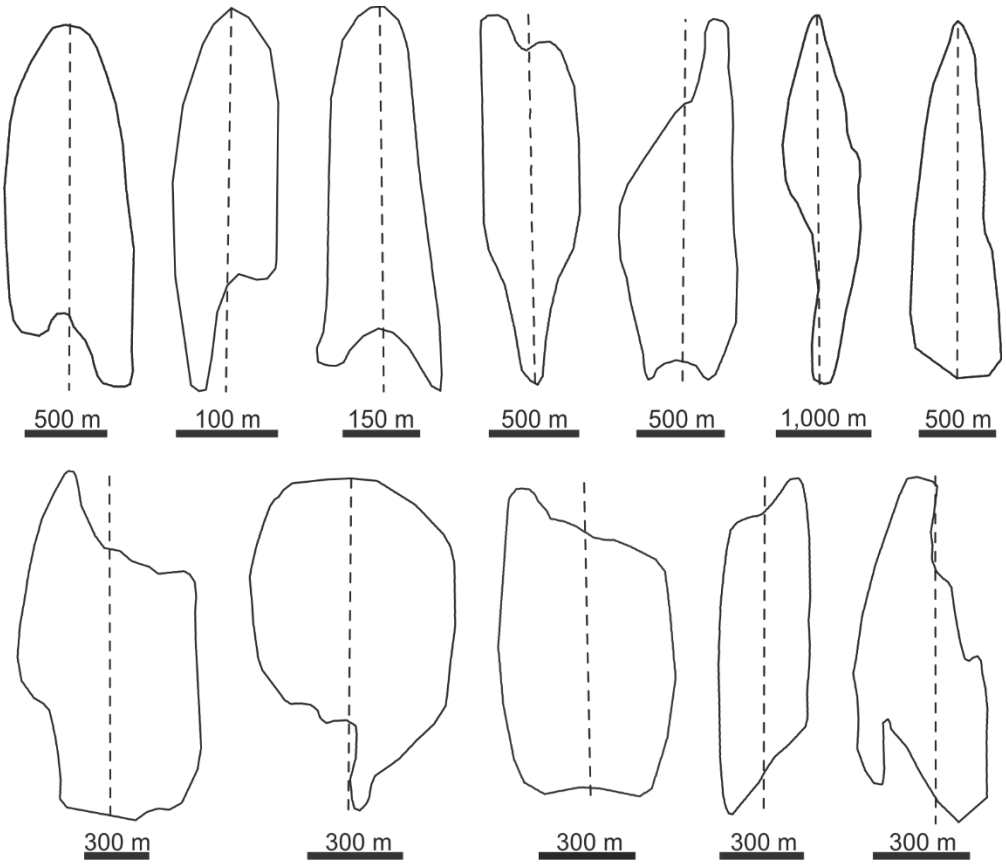


**Figure 2.2 Examples of manually mapped LSB footprints and LAs.**

**Table 2.1 Morphometric statistics for the LSB dataset used in this study (*n* = 100); based on footprints' minimum bounding rectangle; elongation is the ratio of length to width; longitudinal asymmetry is the ratio between the footprints' upflow area and total area ($AS_{pl\_A}$ of Spagnolo et al., 2010)**

| Measure | Minimum | Median | Mean | Maximum |
|---|---|---|---|---|
| Length (m) | 147 | 1198 | 1404 | 4839 |
| Width (m) | 22 | 258 | 356 | 1425 |
| Elongation | 1.3 | 4.1 | 5.4 | 19.8 |
| Longitudinal asymmetry | 0.36 | 0.52 | 0.51 | 0.67 |

## 2.5.2. Reference longitudinal axis

In practical terms, the reference LA is defined as a line sharing the orientation, length and minimum and maximum *y* coordinates (varying along the direction of polygon

elongation) with the footprint it belongs to. A footprint's LA was manually drawn based on a qualitative assessment of footprint shape focusing on what the orientation of a symmetric version (mathematically defined a-axis) of the footprint would be (Fig. 2.2). The transverse placement of the line (i.e. middle vs. others) does not affect orientation or length measurements.

### 2.5.3. Elliptical length

Longitudinal subglacial bedform length was obtained from ellipses derived using the perimeter and area of footprints as proposed by Clark et al. (2009):

$$A = \pi ab \; and \;\; P = \pi\sqrt{2(a^2 + b^2)} \; (Euler's \; approximation) \qquad \textbf{Equation 1}$$

$$Length = \frac{1}{\pi}\sqrt{P^2 + P^4 - 16\pi^2 A^2} \qquad \textbf{Equation 2}$$

In Equation 1, *A*, *P*, and *a* and *b* are the ellipse's area, perimeter, and semi-major and -minor axes, respectively. Equation 2 is the derived expression for obtaining the length of the ellipse based on the perimeter and area of a footprint.

### 2.5.4. Longest straight line

The longest straight line (LSL) enclosed by LSB footprints was derived in the Geospatial Modelling Environment (GME) (Beyer, 2012) software (*geom.polygonfetch* tool). For LSBs lacking pronounced outline concavities, the LSL connects the distant-most pairs of coordinates on the LSB outline. When the outline interferes with the path connecting those two points, the distant-most antipodal locations that can be connected through a straight path are used.

### 2.5.5. Minimum bounding rectangle longitudinal axis

The rectangle longitudinal axis (RLA) (of symmetry) corresponds to a line equidistant to the longest sides of the footprint's minimum bounding rectangle (MBR). Minimum-width, -area and -perimeter bounding rectangles were visually compared; they

were very similar; the minimum-width version was used. The RLA was derived from a Voronoi tessellation based on the MBR's 4 vertices (a skeletonization or medial axis transform – Blum, 1967).

### 2.5.6. Standard deviational ellipse longitudinal axis

The standard deviational ellipse (SDE) (Lefever, 1926) measures the geographic dispersion, and thus trend, of point patterns. For its computation, first, the mean centre of gravity of a set of points is obtained (Fig. 2.3A), then their standard deviation (SD) about the original (arbitrary) (Fig. 2.3B) and several sequentially rotated coordinate-axes (Fig. 2.3C) with origin at the mean centre of gravity (Raine, 1978) computed. Lines connecting same-absolute-value SDs on the respective x-axis define ellipses (Fig. 2.3D).

One-SD SDEs were separately derived for the LSB footprints from i) points equidistantly (5 m) placed at the LSB's outline (SDE1), ii) footprints' structural vertices (i.e. those needed to maintain polygon shape) (SDE2) and iii) footprints' structural vertices and their 180°-rotated version (SDE3), using ARCMAP module *Directional Distribution.* The basis for testing SDE3 is in that, for transversally asymmetric footprints, the rotated set of vertices may counterbalance the asymmetric spatial distribution of the un-rotated set (the combination of both sets is less asymmetric than the individual sets) and thus allow a better estimation of footprint orientation. Structural vertices (approximated) were extracted from simplified (deletion of non-essential points) footprint polygons. SDEs' LA was derived in GME (Beyers, 2012) as their enclosed longest straight line. For ellipses falling short, or extending beyond, the footprint's outline, the LA was extended (*extend* operation in ARCMAP using a layer merging the ellipse's LA to the footprint's MBR-composing lines as input), or cropped, to the MBR limits, respectively.

### 2.5.7. Morphometric data from LAs

Longitudinal axis length corresponds to the Euclidean distance between the line's end points. LA orientation is represented as the angle between the LA and a N-S vector (projection grid) and ranges between -89º and +90º. As a measure of longitudinal

asymmetry, $AS_{pl\_A}$ (Spagnolo et al., 2010) is used: the ratio between the footprint's upflow area and total area. $AS_{pl\_A}$ was derived for each LSB as follows (4th row in Fig. 2.1): 1) creation of the LA's perpendicular bisector (90°-rotation of the LA at its midpoint); 2) footprint partition using the LA's perpendicular bisector; 3) automated labelling of upflow and downflow segments using an ice surface elevation model; and 4) computation of $AS_{pl\_A}$. The Puget lobe ice surface elevation model was derived from Thorson (1980): his contour map (Thorson, 1980: fig. 4) was digitized, the contours densified with vertices, and a continuous surface interpolated using a cell-size of 30 m (ca. one-fifth of minimum footprint length). Ice surface elevation values decrease downflow and thus are lower at the footprints' down than upflow segment. $AS_{pl\_A}$ values above and below 0.5 represent larger up and downflow segments, respectively.

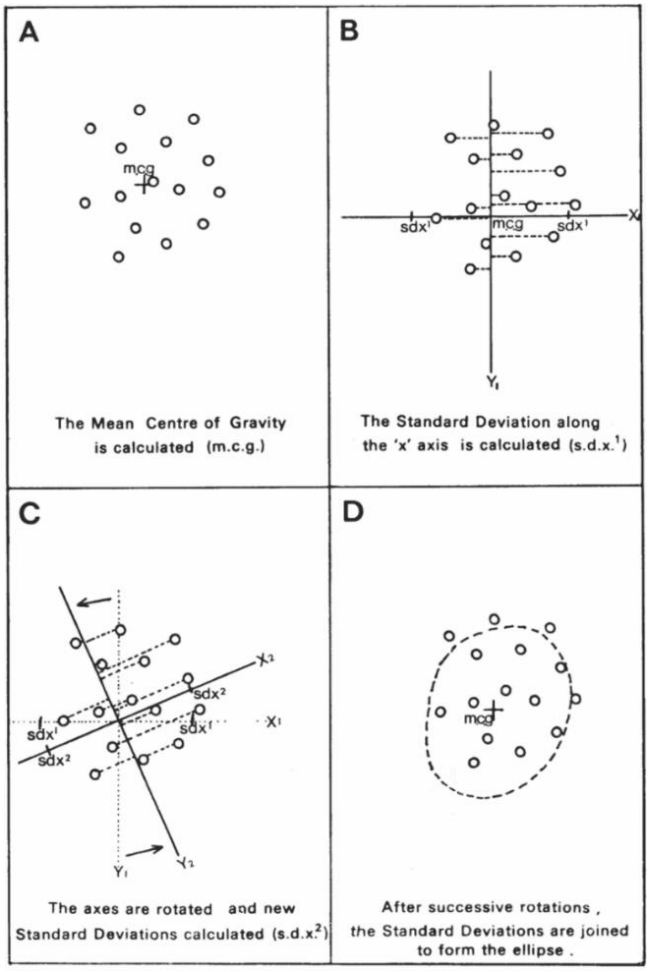


**Figure 2.3 Computation of the standard deviational ellipse (modified from Raine, 1978). Refer to text for explanation.**

### 2.5.8. Performance assessment

For method performance assessment, data based on the manually mapped LA was used as reference, the mean absolute error (MAE) as a measure of accuracy, and standard deviation (SD) as an indicator of precision. MAE is the mean of the absolute differences (errors) between pairs of observations and was used over the root-mean-squared-error because the latter is ambiguous (Willmott and Matsuura, 2005).

## 2.6. Results

With the exception of elliptical length, absolute differences between the values for footprint orientation, length and longitudinal asymmetry computed with the various automated methods diminish with increasing footprint length-to-width ratio (elongation, E) (Fig. 2.4). Elliptical lengths differed considerably (up to 100s of metres) from those of the other methods and independently of elongation (Fig. 2.4B). With the exception of elliptical length, for LSBs with E > ~5 differences between methods were minimal (e.g., < ~1° in orientation). The results presented hereafter refer to LSBs with E <5 ($n$ = 64, Table 2.2) and exclude the 5% highest errors (treated as outliers) ($n$ = 60, Table 2.3). Method performance on orientation, length and longitudinal asymmetry was very strongly, positively correlated (Table 2.4).

Figure 2.5 presents the cumulative histograms of method errors. Errors generally were small. The errors of the LSL, RLA and SDE1-3 methods have normal distributions (curve shape) on all measures. Distributions were very similar between the RLA and SDE1-3 methods and LSL has a distinctively large range on all measures. On length, elliptical length errors have a right-skewed distribution and are up to one order of magnitude larger than those of the other methods. The performance statistics (Table 2.5) summarize Fig. 2.5 distributions. In terms of footprint orientation, RLA and SDE3 were the best performers but, with the exception of LSL, every method had MAE below 3° (Table 2.5). Regarding footprint length, RLA, SDE3 and SDE2 had the best, and LSL and elliptical length the worst, performance, but every method other than elliptical length had accuracy and precision below 5.1 m (Table 2.5). Elliptical length yielded a mean error about 1 order of magnitude higher than LSL and with an equivalently higher SD

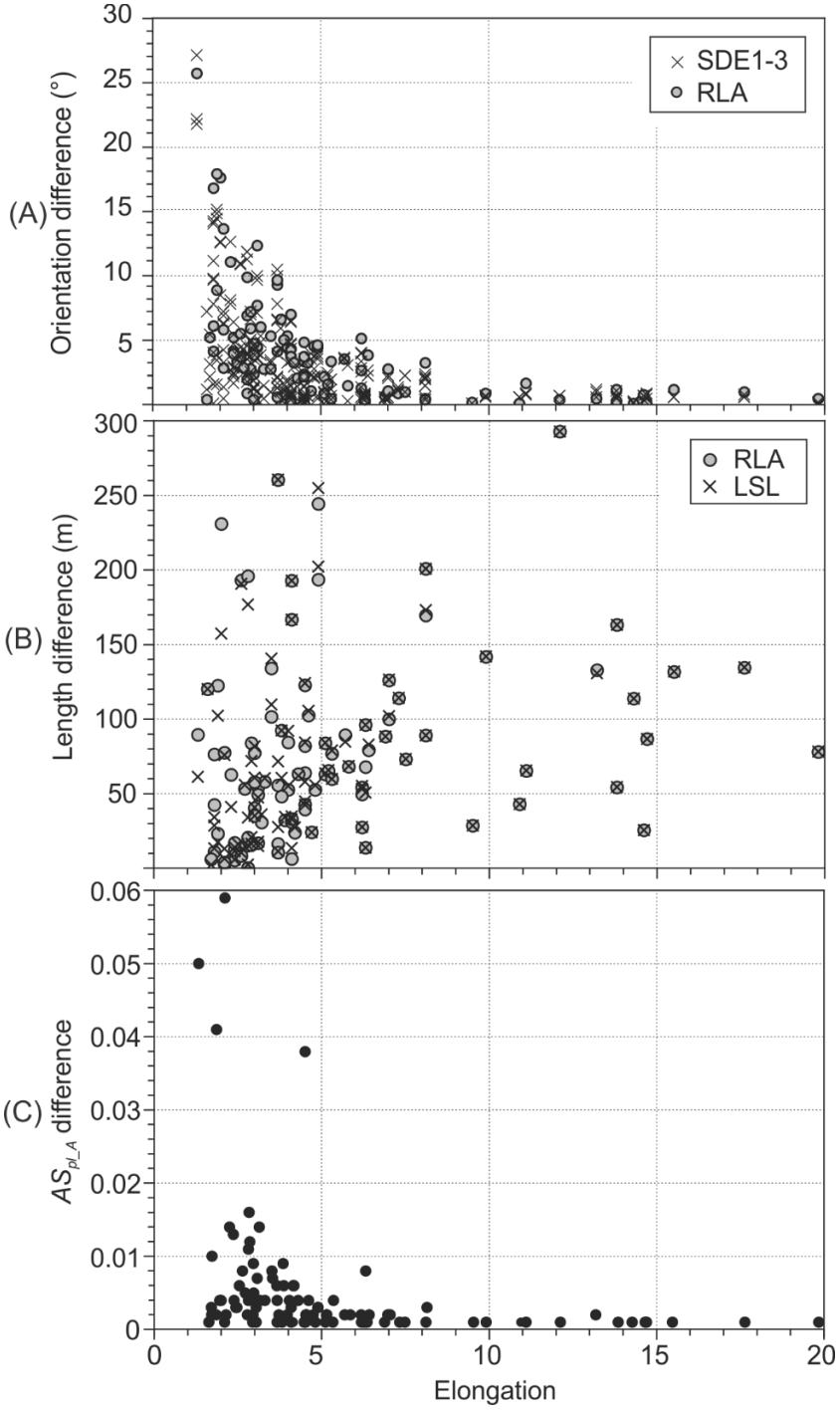


**Figure 2.4** **Relationship between footprint elongation and morphometric differences between methods: A) difference in orientation relative to the LSL method; B) difference in length relative to elliptical length; C) difference between longitudinal asymmetry computed using the LSL and RLA methods.**

(Table 2.5). On longitudinal asymmetry, SDE2 and RLA, and LSL, were the most and least accurate methods, respectively, but every method had very low MAE and SD (Table 2.5). The SDEs based on the footprints' structural vertices (SDE2-3) outperformed (lower MAE and SD) the SDE computed using 5 m-equidistant points on the footprints' outline (SDE1), but by a very small margin (Table 2.5). Concerning the difference between the means from the automated methods and from the reference LAs, only elliptical length yielded a mean off by more than 1% (Table 2.6).

**Table 2.2 Morphometric statistics for LSBs with E <5 based on footprints' minimum bounding rectangle**

| Measure | Minimum | Median | Mean | Maximum |
|---|---|---|---|---|
| Length (m) | 147 | 1198 | 1445 | 4839 |
| Width (m) | 61 | 423 | 462 | 1425 |
| Elongation | 1.3 | 3.1 | 3.2 | 4.9 |
| Longitudinal asymmetry[1] | 0.37 | 0.50 | 0.51 | 0.67 |

[1] $AS_{pl\_A}$, Spagnolo et al., 2010

**Table 2.3 95th percentile of the absolute differences between data from the automated methods and the reference LA for footprints with elongation < 5**

| Method | Orientation (º) | Length (m) | Longitudinal asymmetry[1] * 10^2 |
|---|---|---|---|
| LSL | 18.7 | 27.3 | 1.49 |
| RLA | 7.5 | 13.8 | 0.40 |
| SDE1 | 9.1 | 18.4 | 0.50 |
| SDE2 | 7.6 | 9.3 | 0.37 |
| SDE3 | 7.4 | 10.1 | 0.48 |
| Elliptical length | - | 193.6 | - |

[1] $AS_{pl\_A}$, Spagnolo et al., 2010

**Table 2.4 Correlation between morphometric measure performance (*n* = 60)**

| | Mean absolute error | | Standard deviation | |
|---|---|---|---|---|
| | Length | Longitudinal asymmetry[1] | Length | Longitudinal asymmetry[1] |
| Orientation | 0.98 | 0.99 | 0.95 | 0.98 |
| Length | | 0.97 | | 0.88 |

[1] $AS_{pl\_A}$, Spagnolo et al., 2010

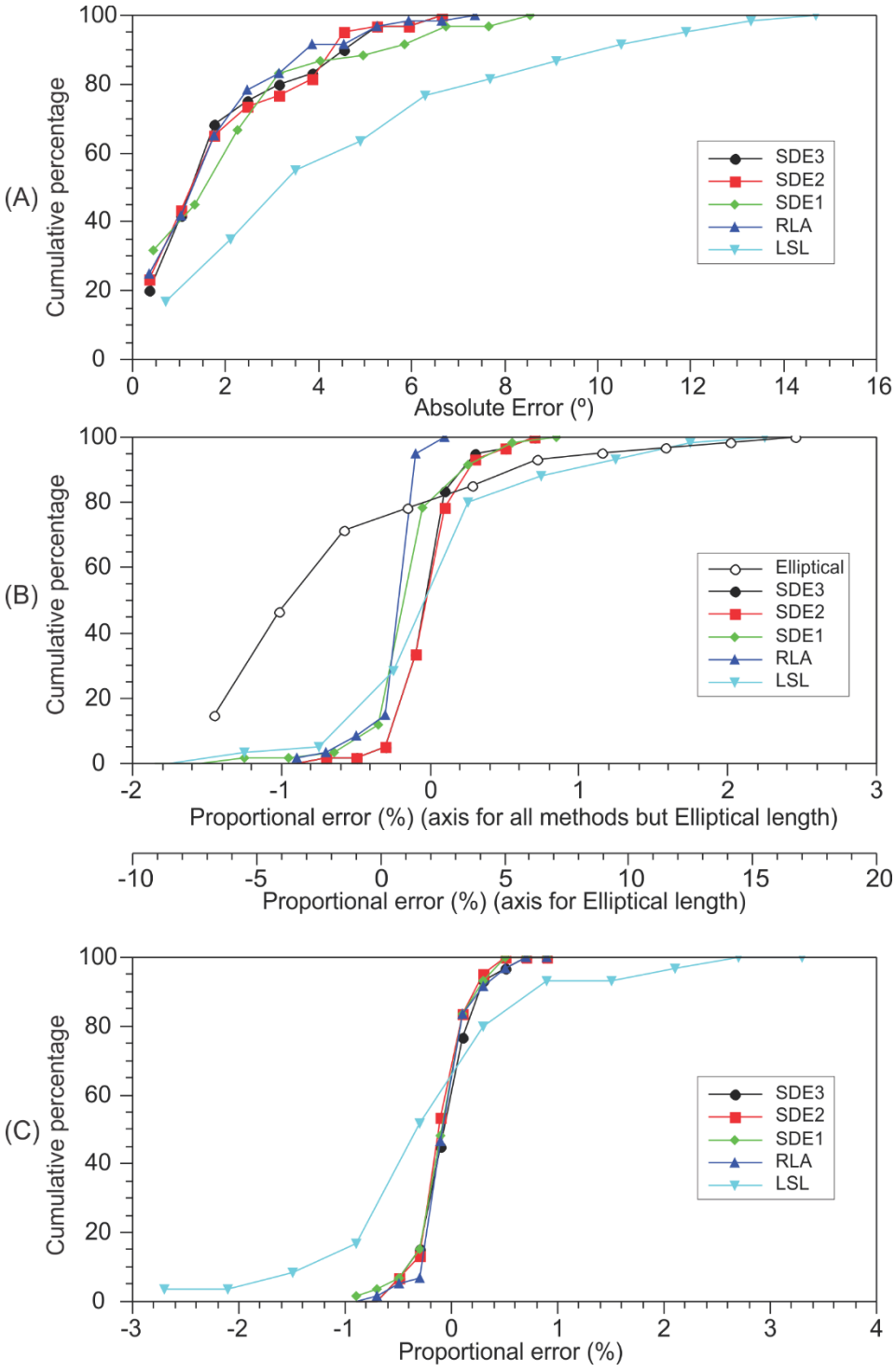


**Figure 2.5** **Cumulative histogram of automated method errors (differences to reference LA) (*n* = 60): A, orientation; B, Length; C, longitudinal asymmetry (*AS*$_{pl\_A}$, Spagnolo et al., 2010).**

**Table 2.5** **Performance assessment (MAE, mean absolute error; SD, standard deviation) (*n* = 60); the lowest and highest values are bolded and underlined, respectively**

| Method | Orientation | | Length | | Longitudinal asymmetry[1] | |
|---|---|---|---|---|---|---|
| | MAE | SD | MAE | SD | MAE x10 | SD x10 |
| LSL | <u>4.7</u> | <u>4.0</u> | 4.6 | 5.1 | <u>0.36</u> | <u>0.37</u> |
| RLA | **2.0** | **1.7** | **1.2** | 2.2 | **0.08** | 0.10 |
| SDE1 | 2.4 | 2.2 | 2.3 | 3.7 | 0.10 | 0.10 |
| SDE2 | 2.1 | 1.8 | 1.8 | **2.1** | 0.09 | **0.08** |
| SDE3 | **2.0** | **1.7** | 1.7 | **2.1** | 0.10 | 0.09 |
| Elliptical length | | | <u>56.1</u> | <u>47.8</u> | | |

[1] $AS_{pl\_A}$, Spagnolo et al., 2010

**Table 2.6** **Differences between means (*n* = 60) – automated methods vs. reference data**

| Method | Orientation (º) | Length (%)[1] | Longitudinal asymmetry (%)[1,2] |
|---|---|---|---|
| LSL | -0.39 | 0.15 | 0.06 |
| RLA | -0.28 | -0.09 | 0.03 |
| SDE1 | 0.29 | -0.02 | 0.01 |
| SDE2 | 0.20 | 0.05 | 0.00 |
| SDE3 | 0.06 | 0.04 | 0.03 |
| Elliptical length | | -1.19 | |

[1] % of the reference mean; [2] $AS_{pl\_A}$, Spagnolo et al., 2010

## 2.7. Discussion

In terms of central tendency, all of the tested methods (LSL, RLA, SDE1-3 and elliptical length) accurately described LSB orientation, length and longitudinal asymmetry (Table 2.6). The differences between the data from the different automated methods increase as LSBs become more compact (E <5, Fig. 2.4) because potential angular divergence between LAs also increases (the possible range in orientation of a line extending between the stoss and lee sides increases). The large errors in orientation with the LSL method and in length with elliptical length (Fig. 2.5) are of concern when analyzing morphometry spatially, especially if error magnitude is spatially autocorrelated.

## 2.7.1. Dependence of method adequacy on footprint shape

### *LSL, RLA and SDE methods*

The relative adequacy of the LSL and RLA methods depends on footprint shape (Table 2.7; Figs 2.6-2.8). In contrast, the SDE2-3 methods are relatively shape-independent (Fig. 2.9), and thus are preferable over the LSL and RLA methods. SDE2 and SDE3 had similar accuracy and precision (Fig. 2.5; Tables 2.5, 2.6), and angular divergence between SDE2 and SDE3 LAs was always small (maximum = 2.3º; Fig. 2.10); SDE2 is preferable over SDE3 because it is simpler to compute.

**Table 2.7 General guidelines on footprint shapes more suited to the LSL and RLA methods**

| Method | Footprint shape |
|---|---|
| LSL | - high elongation[1] (e.g., E > ~5)<br>- ovaloid: ~elliptical and ~half-lemniscate (Figs 2.6a-b, 2.7a-c,e,f)<br>- ~hyperbolic with symmetric convex lee (Figs 2.6e, 2.7d,g) |
| RLA | - high elongation[1] (e.g., > ~5)<br>- ~rectangular (Figs 2.6c, 2.8a-d,g)<br>- ~parabolic (Figs 2.6d, 2.8f,h,i) |
| neither | Hyperbolic with (half-)crescentic or asymmetric lee (Fig. 2.6f) |

[1] Excludes curving LSBs, e.g., curvilineations (Lesemann et al., 2010)

The RLA and LSL methods performed relatively well and poorly, respectively, because ovaloid (~elliptical and ~half-lemniscate) footprints (Fig. 2.6a-b; Fig. 2.7a-c,e,f) and ~hyperbolic footprints with a symmetric convex (as opposed to crescentic) lee (Fig. 2.6e; Fig. 2.7d,g) were relatively rare. Rather, most footprints have misaligned ends (line connecting leading and lee-most points, i.e. LSL, is oblique to the reference LA) (Figs 2.6d,f, 2.8a-i), ~parabolic footprints with (half-)crescentic lee (Figs 2.6d, 2.8f,h,i) being a typical example, and ~"rectangular" footprints (closer to rectangle than to ellipse; Fig. 2.6c) are common (Fig. 2.8a-d,g). For rectangular footprints, LSL will be oblique to the sides of the LSB because the distant-most vertices of a rectangle are at opposite sides of its longitudinal mid-axis (Fig. 2.6c). The RLA method is inadequate for footprints lacking straight segments in their sides (i.e. ovaloid and hyperbolic shapes, Fig. 2.6a,b,e,f) and is well suited to footprints with a relatively long straight segment aligned

parallel to the LA (i.e. rectangular and parabolic shapes, Fig. 2.6c,d). With the exception of very low eccentricity (curvature) hyperbolic footprints (e.g., Fig. 2.7e), for which the RLA method may be adequate, neither the RLA nor the LSL are well suited to describe hyperbolic shapes with (half-)crescentic or asymmetric convex lee (Fig. 2.6f), and curving footprints (e.g., glacial curvilineations of Lesemann et al., 2010).

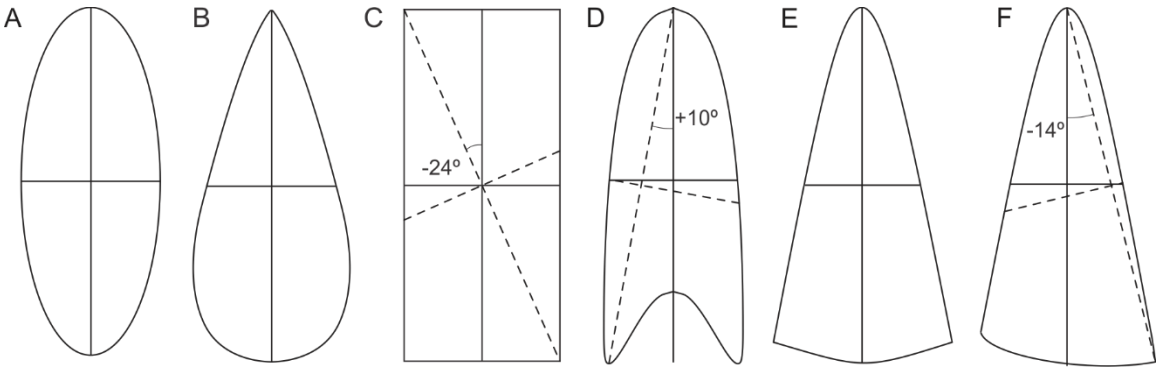


**Figure 2.6** **Idealized shapes: A) elliptical; B) half-lemniscate (non-elliptical oval); C) rectangular; D) parabolic with symmetric crescentic lee; E) hyperbolic with symmetric convex lee; F) hyperbolic with asymmetric convex lee. A and C have 2 axes of symmetry; B, D and E have 1 axis of symmetry. Inside the shapes: solid lines represent the LA and its perpendicular bisector; dashed lines are the LSL and its perpendicular bisector. Angles in C, D and E represent the difference in orientation between the LA and the LSL.**

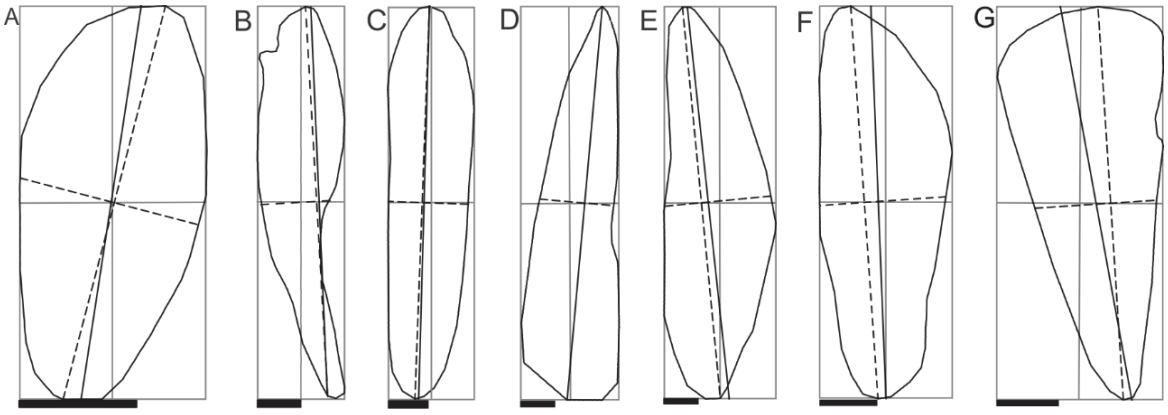


**Figure 2.7** **Examples of Puget Lowland LSB-footprints for which the LSL is a better approximation to the reference LA (orientation) than the RLA. Grey lines are the minimum bounding rectangle and its mid-axes; dashed lines represent the LSL and its perpendicular bisector; solid black lines are the reference LA. Bars at the bottom are 200 m wide.**

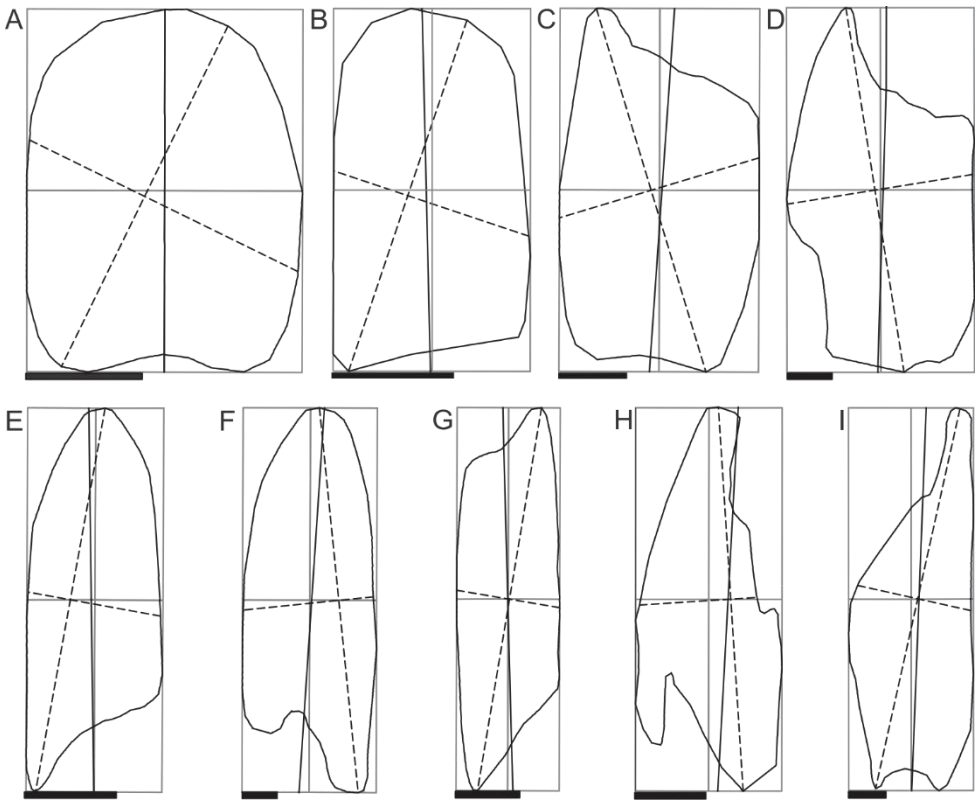


**Figure 2.8 Examples of Puget Lowland LSB-footprints for which the RLA is a better approximation to the reference LA (orientation) than the LSL. Grey lines are the minimum bounding rectangle and its mid-axes; dashed lines represent the LSL and its perpendicular bisector; solid black lines are the reference LA. Bars at the bottom are 200 m wide for A and C-I and 100m wide for B.**

Spagnolo et al. (2011) assessed the relative frequency of different footprint shapes based on the footprint-to-footprint minimum bounding rectangle area ratio, values close to 0.5, 0.78 and 1 indicating resemblance to a rhombus, ellipse and rectangle, respectively. However, this measure is insensitive to geometric variability which, for instance, may lead ~elliptical footprints to be more space-filling than more rectangular shapes, and thus cannot be used to determine which method (LSL or RLA) may be more adequate for a certain dataset. For example, the ratio values for Fig. 2.7A (elliptical) and Fig. 2.8C (rectangular) footprints are 0.78 and 0.77, respectively.

### *Elliptical length*

Equation 2 (after Clark et al., 2009) defines the length of an ellipse based on the area and perimeter of a footprint. However, LSB footprints have outlines of variable complexity/irregularity and their general shape may depart significantly from elliptical. Both a) LSBs of equal length and maximum width but different general shape and/or outline complexity and b) LSBs of equivalent general shape and outline complexity but different elongation, will have different elliptical lengths (Fig. 2.11). Regarding the latter case: for an ellipse, error magnitude increases rapidly with increasing elongation (and area-perimeter ratio) up to ~10% at E ~9, and then ~stabilizes (Fig. 2.12A); for a rectangle, error is minimum at E ~9 and increases both towards higher and lower elongations (Fig. 2.12B).

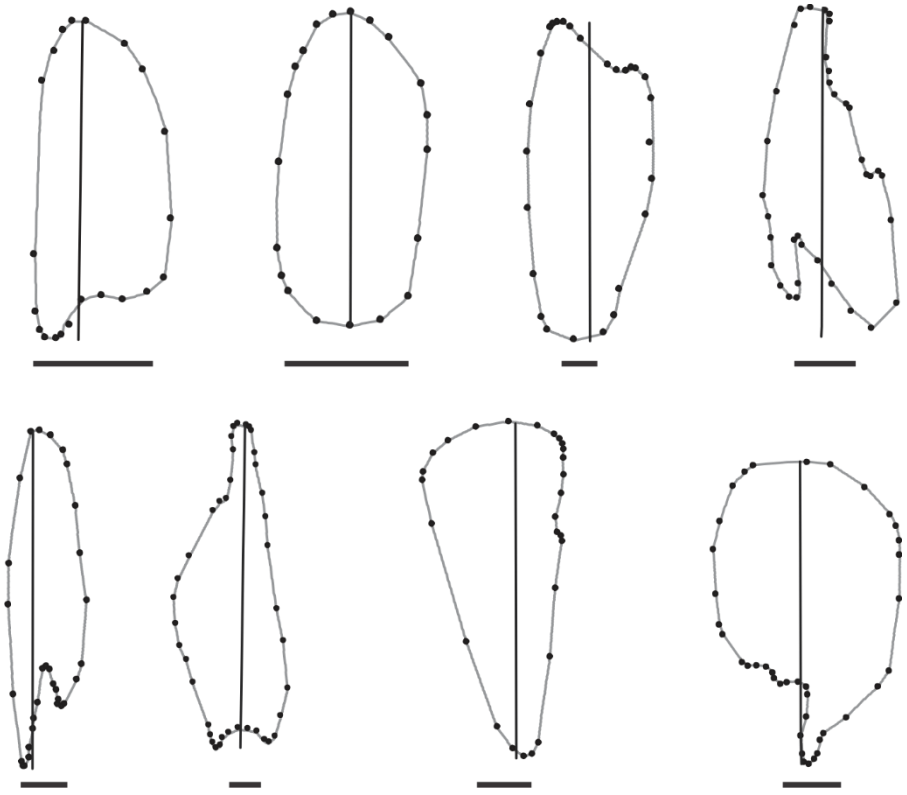

**Figure 2.9** **SDE2 longitudinal axis examples (solid lines). Dots are the footprint's vertices used to compute the SDE. Bars at the bottom are 200 m wide.**

## 2.7.2. Implications for previous works

Clark et al. (2009) used ellipses defined based on the area and perimeter of footprints using Euler's approximation for deriving the length (elliptical length) and width of 37k drumlins from Great Britain. Based on the performance of elliptical length here, bias of their results in terms of central tendency statistics is likely minor, but errors for individual LSBs, and thus in dispersion statistics, may be considerable (i.e. low precision) (Tables 2.5, 2.6; Fig. 2.5). Their LSB dataset should be re-analyzed using more adequate methods (SDE2, RLA and LSL).

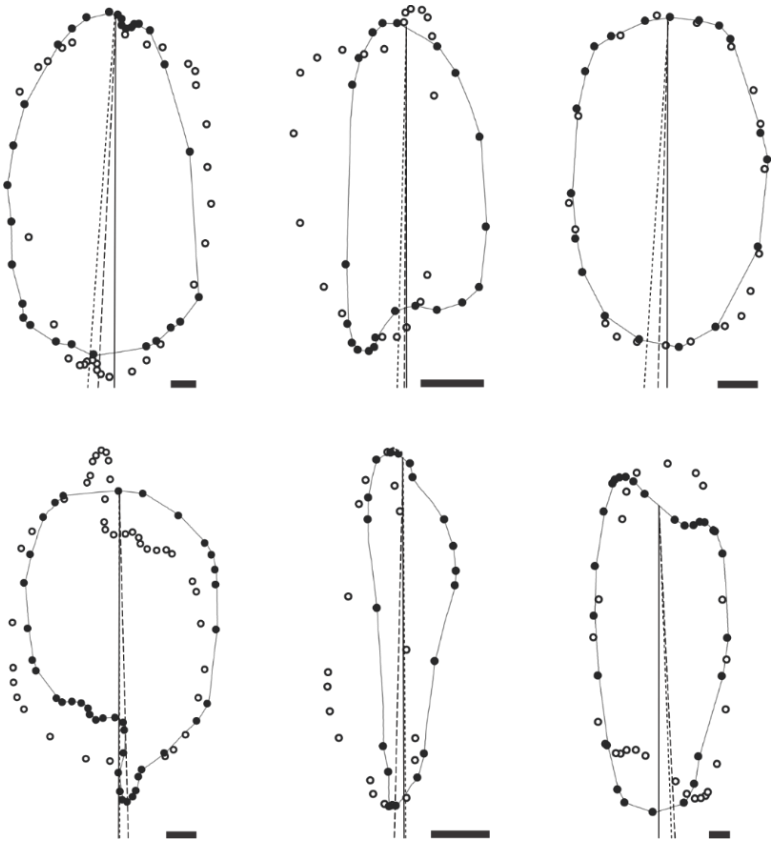

**Figure 2.10** **Footprints with relatively large difference in orientation between the SDE2 and SDE3 methods. Short-dashed, wide-dashed and solid lines represent the orientation of the SDE2, SDE3 and reference LAs, respectively. Black and white dots are the un-rotated and rotated footprints' structural vertices. From left to right and top to bottom, angular divergence between SDE2 and SDE3 lines is 1.7º, 1.1º, 2.2º, 1.3º, 1.7º and 0.6º. Bars at the bottom are 100 m wide.**

Spagnolo et al. (2010) used the LSL to compute longitudinal asymmetry ($AS_{pl\_A}$) for 44.5k drumlins from northern Europe and North America and Dowling et al. (2015) used the minimum bounding rectangle for deriving the length (RLA), width and elongation of 10.3k LSBs from southern Sweden. Based on the results presented here (Tables 2.5, 2.6; Fig. 2.5): their central tendency statistics are likely very accurate; bias in dispersion statistics may be significant and thus should be elucidated (using the SDE2 method).

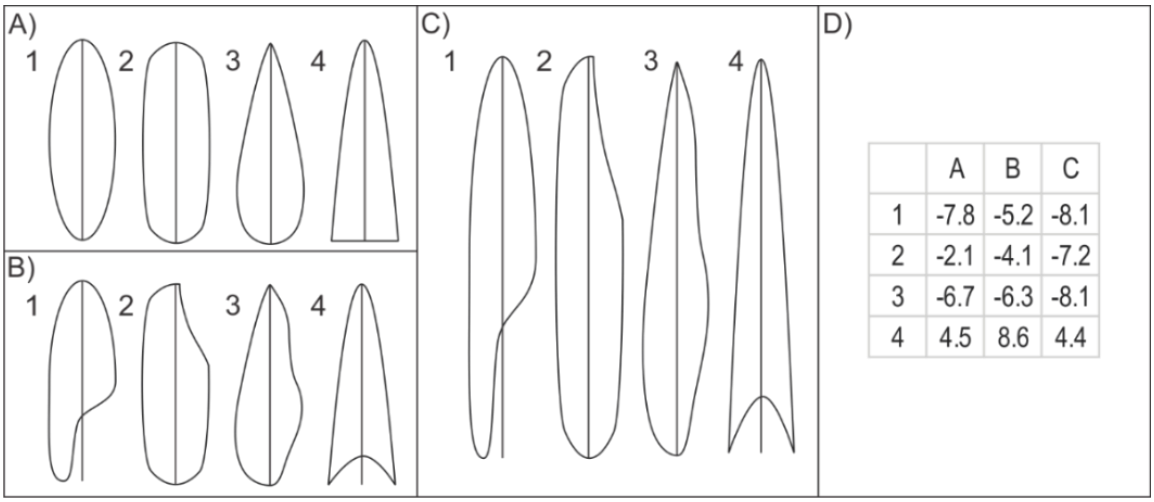


| | A | B | C |
|---|---|---|---|
| 1 | -7.8 | -5.2 | -8.1 |
| 2 | -2.1 | -4.1 | -7.2 |
| 3 | -6.7 | -6.3 | -8.1 |
| 4 | 4.5 | 8.6 | 4.4 |

**Figure 2.11 Dependence of elliptical length accuracy on footprint general shape and outline complexity. A) E = 3, and two axes (1, 2) or one axis (3, 4) of symmetry; B) E = 3, and zero axes (1-3) or one axis (4) of symmetry; C) E = 6, and zero axes (1-3) or one axis (4) of symmetry. D) Elliptical length error (%).**

### 2.7.3. Outlook

Accurate description of LSB footprint (LA) orientation is essential for the inventorying of not only LSB length and longitudinal asymmetry, but also transverse asymmetry, whose quantification has not yet been attempted. Relative to longitudinal asymmetry, transverse asymmetry additionally requires defining the transverse positioning of the LA based on what the transverse symmetric version of the footprint would be. In principle, this longitudinal axis of symmetry represents the vector along which, under homogeneous conditions, formative processes symmetrically unfold to each side of. Accurate retrieval of LSB orientation is fundamental also for the

computation of new, more detailed shape measures, such as based on the longitudinal analysis of footprint width, which possibly can be used to automatedly identify the 5 general types of shapes addressed in this study (elliptical, half-lemniscate, rectangular, parabolic and hyperbolic). For a robust and data-driven LSB shape classification, more detailed measures need to be applied.

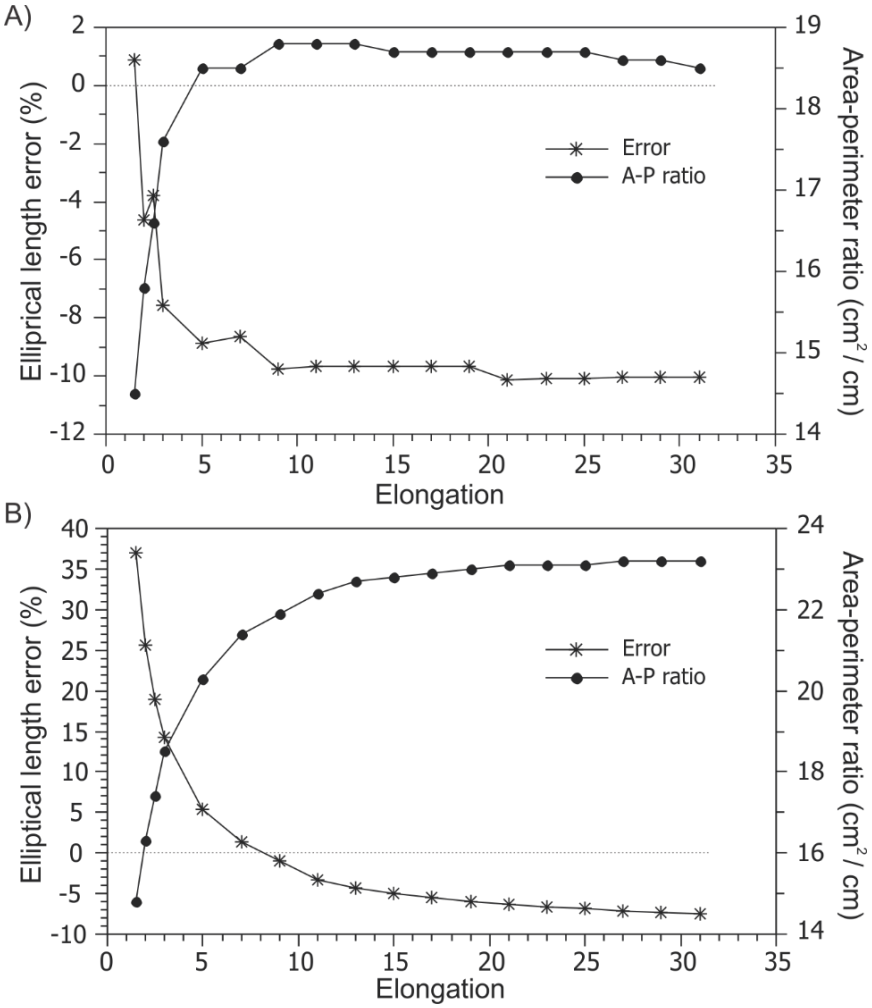


**Figure 2.12 Dependence of elliptical length accuracy on elongation (i.e. area-perimeter ratio): example for an ellipse (A) and for a rectangle (B). Elliptical length error = *[(elliptical length – reference LA length) / reference LA length]* * 100.**

## 2.8. **Conclusion**

With the exception of elliptical length, differences between the morphometric statistics obtained from the manual method (reference for performance evaluation) and the automated methods decrease rapidly with increasing footprint elongation (Fig. 2.4), because of decreasing angular divergence between LAs. For compact LSBs (E <5) and excluding the 5% largest errors (outliers) ($n$ = 60), most methods (LSL, RLA, SDE1-3) can be confidently used to characterize the central tendency of LSB samples. The RLA method (Napieralski and Nalelpa, 2010; Dowling et al., 2015) was the best performer on orientation, length and longitudinal asymmetry (MAE of 2.0º, 1.2 m and 0.008 or 0.1 % of the reference mean, respectively; Table 2.5). The LSL method (Spagnolo et al., 2010) had the worst performance on orientation and longitudinal asymmetry (MAE of 4.7º and 0.004 or 0.4% of the reference mean, respectively) and the second worst performance on length (MAE of 4.6 m) (Table 2.5). Elliptical length (Clark et al., 2009) was the least accurate of all methods (MAE of 56.1 m and 15% of the errors larger than 5%; Table 2.5 and Fig. 2.5) and should be discontinued. When analyzing morphometric data spatially, the LSL method should be avoided for orientation (36% of the errors were >5º, Fig. 2.5).

The relative adequacy of the LSL and RLA methods depends on footprint shape (Table 2.6; Figs 2.6-2.8). In contrast, data from the SDE2 and SDE3 methods (standard deviational ellipse computed based on the footprints' structural vertices) is relatively independent of footprint shape (Figs 2.9, 2.10), making it more reliable than data from the LSL and RLA methods. Mean errors from the SDE2 and SDE3 methods will tend to fall in between those of the LSL and RLA methods. SDE2 is preferable over SDE3 because it is simpler to compute, and thus is, on balance, the preferred method for computing LSB orientation, length and longitudinal asymmetry. Applying the methods tested here (LSL, RLA and SDE) to large LSB samples described in previous studies would help quantify errors in the current LSB morphometric inventory.

## 2.9. **References**

Beyer, H. L., 2012. Geospatial Modelling Environment (Version 0.7. 2.1). URL: http://www.spatialecology.com/gme.

Blum, H., 1967. A transformation for extracting new descriptors of shape. In: Dunn, W. W. (Ed.), Proc. Symp. Models for the Perception of Speech and Visual Form. MIT Press, Cambridge, MA, pp. 362–380.

Clark, C. D., 1993. Mega-scale glacial lineations and cross-cutting ice-flow landforms. Earth Surface Processes and Landforms 18(1), 1-29.

Clark, C. D., 2010. Emergent drumlins and their clones: from till dilatancy to flow instabilities. Journal of Glaciology 56(200), 1011-1025.

Clark, C. D., Tulaczyk, S. M., Stokes, C. R., Canals, M., 2003. A groove-ploughing theory for the production of mega-scale glacial lineations, and implications for ice-stream mechanics. Journal of Glaciology 49(165), 240-256.

Clark, C. D., Hughes, A. L., Greenwood, S. L., Spagnolo, M., Ng, F. S., 2009. Size and shape characteristics of drumlins, derived from a large sample, and associated scaling laws. Quaternary Science Reviews 28(7), 677-692.

Davis, W.M., 1884. Drumlins. Science 4, 418–420.

Dowling, T. P.F., Spagnolo, M., Möller, P., 2015. Morphometry and core type of streamlined bedforms in southern Sweden from high resolution LiDAR. Geomorphology (accepted manuscript).

Ely, J. C., Clark, C. D., Spagnolo, M., Stokes, C. R., Greenwood, S. L., Hughes, A. L., Dunlop, P., Hess, D., 2014. Demonstration of a subglacial bedform continuum: Is a unifying formation theory required?. EGU General Assembly Conference Abstracts 16, 5533.

Evans, I. S. 2012., Geomorphometry and landform mapping: What is a landform?. Geomorphology 137(1), 94-106.

Fowler, A. C., Chapwanya, M., 2014. An instability theory for the formation of ribbed moraine, drumlins and mega-scale glacial lineations. Proceedings of the Royal Society A: Mathematical, Physical and Engineering Science 470, 20140185.

Goldstein, B., 1994. Drumlins of the Puget Lowland, Washington State, USA. Sedimentary geology 91(1), 299-311.

Harry, D. G., Trenhaile, A. S., 1987. The morphology of the Arran drumlin field, southern Ontario, Canada. In: Menzies, J., Rose, J. (Eds), Drumlin Symposium. Balkema, Rotterdam, pp. 161–173.

Hooke, R. L., Medford, A., 2013. Are drumlins a product of a thermo-mechanical instability?. Quaternary Research 79(3), 458-464.

Hughes, A. L., Clark, C. D., Jordan, C. J., 2010. Subglacial bedforms of the last British Ice Sheet. Journal of Maps 6(1), 543-563.

Lamsters, K., 2012. Drumlins and related glaciogenic landforms of the Madliena Tilted Plain, Central Latvian Lowland. Bulletin of the Geological Society of Finland 84, 45–57.

Lamsters, K., Zelčs, V., 2014. Subglacial bedforms of the Zemgale Ice Lobe, south-eastern Baltic. Quaternary International (in press).

Lefever, D. W., 1926. Measuring geographic concentration by means of the standard deviational ellipse. American Journal of Sociology 32, 88-94.

Lesemann, J. E., Piotrowski, J. A., Wysota, W., 2010. “Glacial curvilineations”: New glacial landforms produced by longitudinal vortices in subglacial meltwater flows. Geomorphology 120(3), 153-161.

Maclachlan, J. C., Eyles, C. H., 2013. Quantitative geomorphological analysis of drumlins in the Peterborough drumlin field, Ontario, Canada. Geografiska Annaler: Series A, Physical Geography 95(2), 125-144.

Menzies, J., 1979. A review of the literature on the formation and location of drumlins. Earth-Science Reviews 14(4), 315-359.

Napieralski, J., Nalepa, N., 2010. The application of control charts to determine the effect of grid cell size on landform morphometry. Computers & Geosciences 36(2), 222-230.

NDEP, 2004. Guidelines for Digital Elevation Data. National Digital Elevation Program (NDEP), Version 1.0. (http://www.ndep.gov/NDEP_Elevation_Guidelines_Ver1_10May2004.pdf).

Prest, V. K., Grant, D. R., Rampton, V. N., 1968. Glacial map of Canada. Geological Survey of Canada, "A" Series Map.

Raine, J. W., 1978. Summarizing point patterns with the standard deviational ellipse. Area 10(5), 328-333.

Reed, B., Galvin, C. J., Miller, J. P., 1962. Some aspects of drumlin geometry. American Journal of Science 260(3), 200-210.

Rose, J., 1987. Drumlins as part of a glacier bedform continuum. In: Menzies, J., Rose, J. (Eds), Drumlin Symposium. Balkema, Rotterdam, pp.103-116

Schoof, C. G., Clarke, G. K., 2008. A model for spiral flows in basal ice and the formation of subglacial flutes based on a Reiner-Rivlin rheology for glacial ice. Journal of Geophysical Research: Solid Earth 113(B5).

Shaw, J., 2002. The meltwater hypothesis for subglacial bedforms. Quaternary International 90(1), 5-22.

Spagnolo, M., Clark, C. D., Hughes, A. L., Dunlop, P., Stokes, C. R., 2010. The planar shape of drumlins. Sedimentary Geology 232(3), 119-129.

Spagnolo, M., Clark, C. D., Hughes, A. L., Dunlop, P., 2011. The topography of drumlins; assessing their long profile shape. Earth Surface Processes and Landforms 36(6), 790-804.

Spagnolo, M., Clark, C. D., Ely, J. C., Stokes, C. R., Anderson, J. B., Andreassen, K., Graham, A. G. C., King, E., 2014. Size, shape and spatial arrangement of mega-scale glacial lineations from a large and diverse dataset. Earth Surface Processes and Landforms 39(11), 1432-1448.

Stokes, C. R., Clark, C. D., 2002. Are long subglacial bedforms indicative of fast ice-flow?. Boreas 31(3), 239-249.

Stokes, C. R., Spagnolo, M., Clark, C. D., 2011. The composition and internal structure of drumlins: Complexity, commonality, and implications for a unifying theory of their formation. Earth-Science Reviews 107(3), 398-422.

Stokes, C. R., Spagnolo, M., Clark, C. D., Ó Cofaigh, C., Lian, O. B., Dunstone, R. B., 2013. Formation of mega-scale glacial lineations on the Dubawnt Lake Ice Stream bed: 1. size, shape and spacing from a large remote sensing dataset. Quaternary Science Reviews 77, 190-209.

Thorson, R. M., 1980. Ice-sheet glaciation of the Puget Lowland, Washington, during the Vashon Stade (late Pleistocene). Quaternary Research 13(3), 303-321.

Willmott, C. J., Matsuura, K., 2005. Advantages of the mean absolute error (MAE) over the root mean square error (RMSE) in assessing average model performance. Climate research 30(1), 79-82.

# Chapter 3.

# Towards the semi-automated extraction of longitudinal subglacial bedforms from DTMs – two new methods[1]

## 3.1. Highlights

1. DTM preprocessing drastically improved DTM suitability for longitudinal subglacial bedform (LSB) semi-automated mapping.

2. The closed contour method outperforms the land-form elements mask method and published methods.

3. Normalized local relief closed contours define LSB-candidate objects.

4. Existent opensource software is fully adequate for applying the methods.

## 3.2. Abstract

Relict drumlin and mega-scale glacial lineation (positive relief, longitudinal subglacial bedforms – LSBs) morphometry has been used as a proxy for paleo-ice-sheet dynamics though LSB genesis is unresolved and the current morphometric inventory incomplete. LSB morphometric inventories have relied on manual mapping, which is subjective and thus difficult to reproduce. Automated mapping overcomes this, and is faster, but previous methods for LSB (semi-)automated mapping have not been highly successful.

[1] A version of this chapter is in preparation for submission to the journal Geomorphology as: Jorge, M.G. & Brennand, T.A. Towards the semi-automated extraction of longitudinal subglacial bedforms from DTMs – two new methods.

Here, two new (object-based) methods for the semi-automated extraction of LSBs (footprints) from DTMs are tested. As segmentation procedures, the normalized closed contour method (NCCM) relies on the contouring of a normalized local relief model (NLR) (addressing LSBs on slopes) and the land-form elements mask method (LEMM) on the classification of land-form elements derived from the DTM. Both use the same LSB (operational) definition: a ruleset encapsulating expert knowledge, published morphometric data and the morphometric range of LSBs in the study area. The NCCM was separately applied to 4 different NLR models, two computed in moving windows and two hydrology-based. The NCCM outperformed the LEMM. NCCM based on a hydrological relief model from a multiple direction flow routing algorithm performed best. The NCCM with a hydrological relief model from a combination of two flow routing algorithms (multiple and single direction) had the highest general detection rate (90%; better than equivalent measures in published methods), morphometric detection rate (56%), True Skill Statistic (0.48) and kappa (0.49). Future work on the NCCM could focus on improving NLR modeling for LSBs on slopes, testing absolute (fixed-datum) elevation contours as an alternative to NLR modeling for LSBs on relatively flat terrain, and refining the LSB ruleset.

Keywords: semi-automated mapping; drumlin; mega-scale glacial lineation; closed contour; landform elements; morphometry

## 3.3. Introduction

Drumlins and mega-scale glacial lineations (MSGLs) (Davis, 1884; Menzies, 1979; Clark, 1993) are smoothly rounded, elongate, positive-relief subglacial bedforms typically oriented (sub)parallel to ice flow vectors in effect at the time of their formation and with variable composition (Stokes et al., 2011; Ó Cofaigh et al., 2013) and wide dimensional range (Clark et al., 2009; Spagnolo et al., 2012; Spagnolo et al., 2014; Dowling et al., 2015). They are very frequent within the footprints of past ice sheets (e.g., Prest et al., 1968; Hughes et al., 2010), occurring in spatial clusters of tens to tens of thousands of individuals (i.e. drumlin fields) with spatially autocorrelated morphometry (e.g., Trenhaile, 1975; Aario, 1977; Francek, 1991; Smalley and Warburton, 1994; Stokes and Clark, 2002) and typically arranged in regular patterns (cf. Clark, 2010). The distinction between drumlins and MSGLs has been based on shape and size, the latter

being more elongate, longer and morphologically less varied than the first (Clark, 1993; Stokes and Clark., 2002; Clark et al., 2009). However, recent studies (Stokes et al., 2013; Spagnolo et al., 2014; Ely et al., 2014) indicate that, dimension-wise, drumlins and MSGLs are indivisible, underscoring a subglacial bedform continuum (Rose, 1987). Current data indicates that, together, drumlins and MSGLs range from 0.3 m to 120 m in height (Spagnolo et al., 2012, 2014; Dowling et al., 2015), from 20 m to several 10s of km in length and from 15 m to 5 km in width (Clark et al., 2009; Spagnolo et al., 2014). Drumlins and MSGLs are hereafter collectively referred to as longitudinal subglacial bedforms (LSBs).

Longitudinal subglacial bedforms form at the ice-bed interface, where a large proportion of glacier velocity is modulated (Engelhardt et al., 1990; Stearns et al., 2008; Rignot et al., 2011), and thus their morphometry has been linked to ice flow (e.g., Stokes and Clark, 2002; King et al., 2009) or meltwater flow (e.g., Shaw, 2002; Shaw et al., 2008). Relict LSB morphometry has been used in paleoglaciological reconstructions to map ice flow direction, ice streams (e.g., Sollid and Sørbel, 1994; Kleman et al., 1997; Stokes and Clark, 2001; Greenwood and Clark, 2009; Margold et al., 2014, 2015) and flood flows (underbursts, Shaw et al., 1989, 1996; Rains et al., 1993; Munro-Stasiuk and Shaw, 2002) despite LSB genesis being unresolved (e.g., Clark et al., 2010; Stokes et al., 2011; Hooke and Medford, 2013; Spagnolo et al., 2014; Fowler and Chapwanya, 2014). Testing hypotheses of LSB genesis requires an adequate inventory of their morphometry. The first step in this inventory is LSB footprint mapping.

To date, LSB footprint mapping has been mainly done manually, based on visual interpretation (e.g., Clark et al., 2009; Spagnolo et al., 2010, 2011, 2012; Stokes et al., 2013; Spagnolo et al., 2014; Dowling et al., 2015), a methodology which is slow and subjective and thus difficult to reproduce. Uncertainty about the magnitude of the subjective differences and the validity of manually mapped footprint datasets limit interpretations from derived morphometric analyses. Other limitations to the current morphometric inventory include insufficient or no data on 2D transverse asymmetry, 3D shape, and spatial arrangement and autocorrelation, and, although ~100,000 LSBs have been inventoried (Ely et al., 2014), uncertainty about sample representativeness.

(Semi-)automated mapping techniques are objective and fast (Van Asselen and Seijmonsbergen, 2006; Molloy and Stepinski, 2007; Saha et al., 2011). When combined with the increasing availability of high-resolution digital terrain models (DTMs, NDEP, 2004) (e.g., 12 m x 12 m cell-size global DEM, http://www.astrium-geo.com/en/168-tandem-x-global-dem), (semi-)automated mapping has the potential to improve the robustness of the LSB morphometric inventory available to test and to constrain hypotheses of LSB genesis and thus LSB glaciological significance.

Whereas the automated classification of DTMs into elementary forms or land-form elements is well established (e.g., Dikau et al., 1991; MacMillan et al., 2000; Drăguţ and Blaschke, 2006; Minár and Evans, 2008; Jasiewicz and Stepinski, 2013), algorithms for the delineation of genetic landforms are more demanding and have had more limited success. The first group of methods is conceptually simpler to implement because classes are simply morphometric or geometric. In contrast, genetic landforms are assemblages of elementary forms (composite forms of Minár and Evans, 2008) and have both a morphological and a genetic component in their definition – they can be thought of as units of maximum internal morphogenetic homogeneity and, in principle, only landforms with a morphometric (topographic) signature can be mapped with high success rates. Automated drumlin delimitation is thought to be a simple procedure (Evans, 2012) because they are typically bounded by concave breaks in slope gradient and have a distinct appearance, but a topographic signature has not been previously quantitatively demonstrated.

The (semi-)automated mapping of LSB footprints from DTMs is a recent endeavour. Rutzinger et al. (2012) test automated breakline mapping for a single drumlin amongst other landforms. Maclachlan and Eyles (2013) use closed contour analysis, but do not focus on method development. Saha et al. (2011), d´Oleire-Oltmanns et al. (2013) and Eisank et al. (2014) use multi-resolution segmentation (MRS) of DTMs within an object-based image analysis framework (Baatz and Schäpe, 2000), but with inadequate results for morphometric purposes. DTM-based automated mapping methods have been developed with varying success for other landforms, including craters (Bue and Stepinski, 2007), volcanos (Euillaides et al., 2013) and sinkholes (de Carvalho et al., 2013). Here, two new object-based methods for the semi-automated

extraction of LSB footprints from DTMs are presented, and tested in the Puget Lowland Drumlin Field (Goldstein, 1994), WA, USA.

## 3.4. Object-based mapping of LSBs: past work

(Semi-)automated object-based landform mapping spans the fields of digital image processing and geomorphometry (Evans, 1972), a sub-discipline of geomorphology concerned with the study of land surface form(s) through digital terrain modeling and analysis. Mapping with object-based (image) analysis (OBIA, Baatz and Schäpe, 2000) (OBA) typically entails: 1) segmentation of the image(s) into segments or objects (aggregations of pixels), based on either internal homogeneity criteria (e.g., slope variance) (region-based segmentation) or outline (e.g., break-of-slope) recognition and delineation (edge-based segmentation); and 2) object classification or filtering – from candidate objects to meaningful objects (Blaschke, 2010). The nature of OBA segmentation algorithms is what distinguishes OBA from somewhat equivalent pixel-based procedures the most: segmentation is based not only on pixel values but also on image texture (Lucieer and Stein, 2005), leading to the creation of more intelligible (i.e. more proximal to real world features) objects better suited for semantic modelling – the implementation of pertinent knowledge about the feature(s) being mapped into computer language/software realized terms (an operational definition *sensu lato*). In addition, classifications based on image objects are less affected by the "salt-and-pepper" noise that is common in pixel-based classifications (Blaschke et al., 2000), and segmentation results are typically handled in a vector graphics format, allowing easy derivation of any kind of attribute (aggregative cell statistics, geometry, context) for the individual objects prior to, and to be used by, the classifier or filter. The acronym GEOBIA has been more recently introduced in the literature in order to acknowledge the specificity of geographic objects (Blaschke, 2010). The application of OBA to DTMs is recent, the first studies dating from 2006 (Stepinski et al., 2006; Drăguţ and Blaschke, 2006). eCognition® probably has been the most used OBA software in geomorphological studies, but other software, some of which are opensource (e.g., OrfeoToolbox, orfeo-toolbox.org; QGIS, www.qgis.org; SAGA GIS, www.saga-gis.org), also support OBA. Here, the expression

*object-based* refers to any analysis or method which includes segmentation of an image or DTM into objects more meaningful than individual cells as one of its steps.

It was within this context that Saha et al. (2011), d´Oleire-Oltmanns et al. (2013) and Eisank et al. (2014) used object-based methods in their attempts to (semi-)automate the extraction of drumlin footprints from DTMs. Saha et al. (2011) extract then merge three terrain objects: two slopes facing opposite directions and outlined by breaks in slope gradient, and one ridge (mediating the slopes). Drumlin objects are essentially defined through edge-based segmentation and classified from morphometric rules based on manually mapped LSBs in their study area. On the other hand, d'Oleire-Oltmanns et al. (2013) and Eisank et al. (2014) use a region-based segmentation (multiresolution segmentation of Baatz and Schäpe, 2000) to extract drumlin footprints as individual objects. d'Oleire-Oltmanns et al. (2013) define drumlins as multi-convex relief units (based on mean curvature) with elliptical planar shape. Eisank et al. (2014) test the individual suitability of several terrain parameters, i.e. do not use a single operational definition. Because drumlins are topographically complex and variable and currently are not well represented by a single terrain parameter(ization), using a region-based segmentation (delineation of homogeneous objects) for directly extracting footprints as single objects is counterintuitive.

(Semi-)automated terrain object-based LSB (landform) mapping can be broadly defined as a 4-step procedure: 1) computation of terrain parameter(s) on which the landform operational definition is built; 2) segmentation of terrain parameter(s) (one- or multi-dimensional cell-based feature vectors) – from a data storage structure-controlled representation (cells) to terrain-meaningful objects; 3) computation of object attributes required for implementing the operational definition; and 4) classification or filtering. Whether multi-scale segmentation is or is not needed in order to deal with the landform dimensional range depends on the segmentation algorithm used.

## 3.5. Methods

Two new methods for the semi-automated mapping (SAM) of LSB footprints from DTMs are compared in a test area in the Puget Lowland, WA, USA (section 3.5.1). Their

performance is assessed in relation to a footprint dataset from manual mapping (MM) (section 3.5.2). One method is based on the identification of normalized local relief (NLR) contour-bounded terrain objects with LSB-like morphometry and is separately applied to 4 different NLR models (section 3.5.5). This is referred to as the normalized closed contour method (NCCM) (Fig. 3.1). The second method involves classifying the DTM into landform elements, masking out elements rare to absent in LSBs and identifying terrain segments with LSB-like morphometry out of the remaining areas (section 3.5.6). This is referred to as the landform elements mask method (LEMM) (Fig. 3.2). Both methods share the same DTM preprocessing (section 3.5.4) and LSB operational definition (section 3.5.3). The latter is a ruleset combining expert knowledge with morphometric data from previous inventories and from MM-LSBs in the study area.

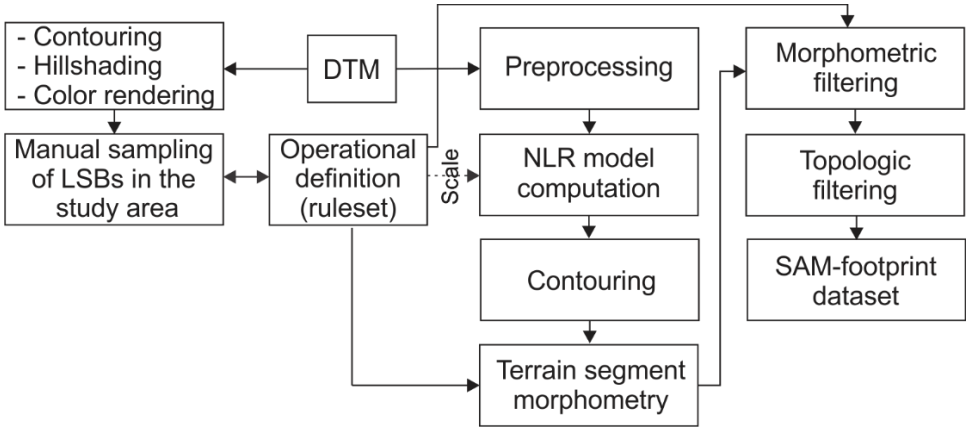


**Figure 3.1 NCCM processing flow.**

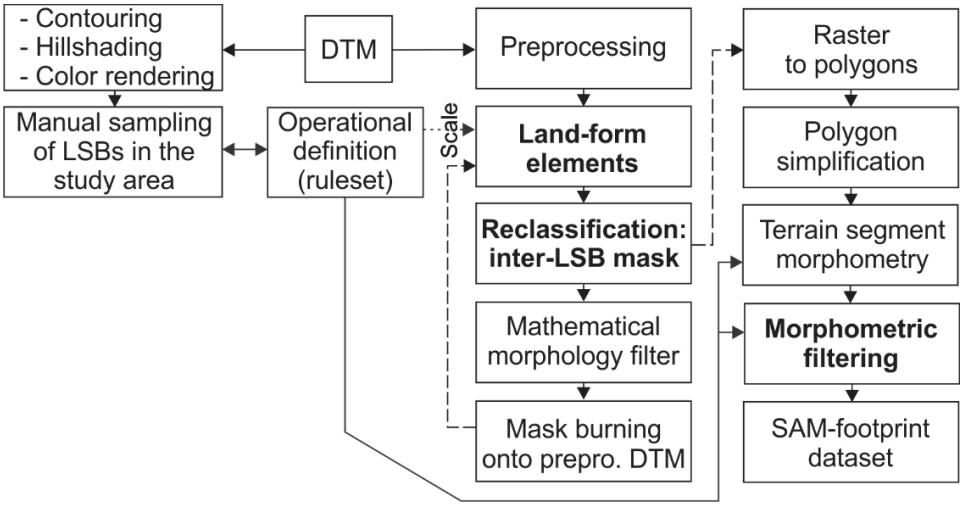


**Figure 3.2 LEMM processing flow.**

### 3.5.1. Test area and DTM

The test area (139.5 $km^2$) is located in the east-central part of the Puget Lowland Drumlin Field (Goldstein, 1994; ~19k $km^2$), WA, USA and within the footprint of the Puget lobe, a fast flowing, topographically constrained outlet glacier of the last Cordilleran Ice Sheet which attained its maximum extent 17,420 ± 90 cal yr BP (Porter and Swanson, 1998) (Fig. 3.3). The test area was chosen over other areas in the drumlin field because it is a relatively large area seamlessly populated by LSBs with a relatively high diversity of morphometries and has relatively low anthropogenic disturbance. The northern and southern limits of the test area are (sub-)perpendicular to the general orientation of the LSBs that they cross.

The region is covered by several freely available DTMs, including USGS National Elevation Data of 1/3 and 1/9 arc-second (6.9 m and 2.3 m at the latitude of Seattle, respectively) horizontal resolution, a 1.8 m cell-size DTM with vertical resolution <1 m produced by the Puget Sound LiDAR Consortium (http://pugetsoundlidar.ess.washington.edu/About_PSLC.htm), and a 9.1 m cell-size DTM partly created by downsampling (5x) of the previous (Puget Sound DEM, PSDEM – Finlayson, 2005). This study uses the 1.8 m DTM downsampled (weighted average) to a 9.1 m cell-size (not the PSDEM because it is distorted in the test area), which is appropriate for studies on LSB morphometry (cf. Napieralski and Nalepa, 2010). This cell-size was chosen over the original 1.8 m because it is closer to typical resolutions of DTMs available for other regions and reduces noise and DTM size (14 vs. 350 megabytes) while not compromising the identification of small LSBs in the test area.

### 3.5.2. LSB manual mapping

The MM-footprint dataset is used as the reference for SAM performance assessment and for deriving some of the values for the LSB ruleset. LSB edges mostly correspond to concave breaks in slope gradient and, accordingly, MM of LSBs (footprints) has been based on break-of-slope delineation (e.g., Mitchell and Riley, 2006; Clark et al., 2009; Spagnolo et al., 2010; Saha et al., 2011; Dowling et al., 2015). The same criterion is used here. LSB footprint polygons were manually drawn within a GIS by inspecting a zenith-hillshaded (~slope) terrain model overlain with 1.5 m-interval

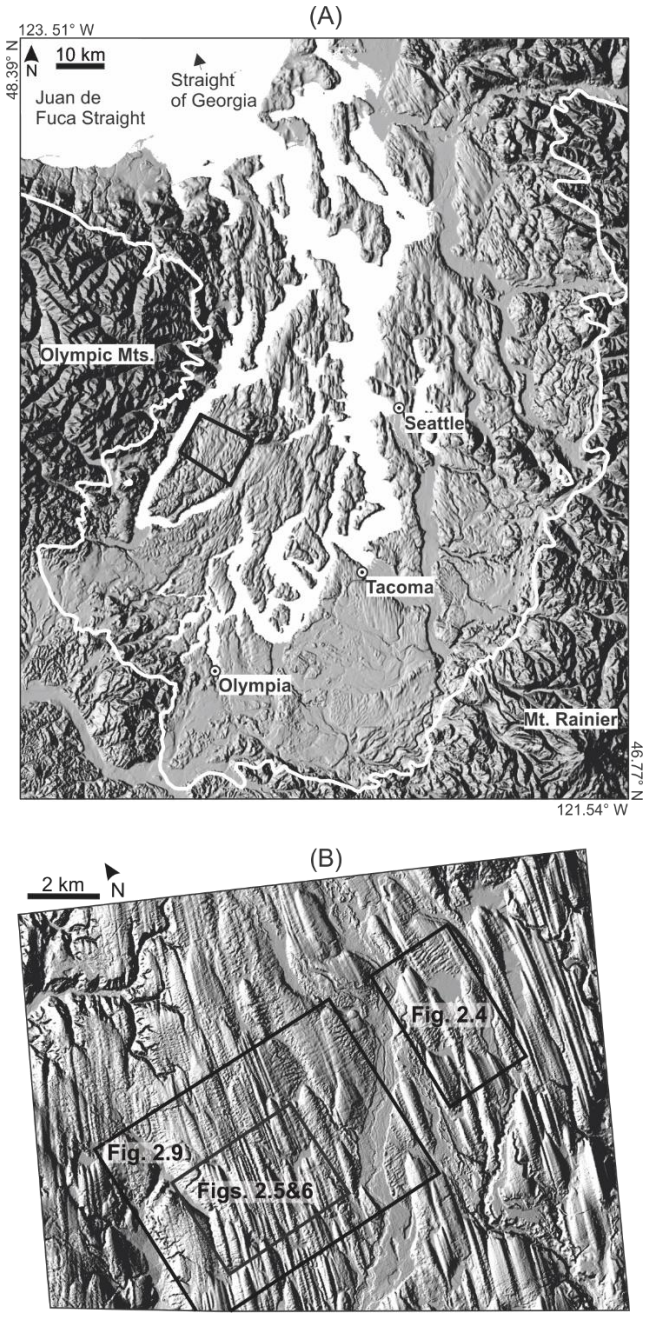


**Figure 3.3** **Test area. A) Location of the test area (black-outline quadrangle) within the Puget Lowland Drumlin Field and Puget Lobe footprint; the white line marks the last maximum extent of the Cordilleran Ice Sheet (Thorson, 1980). The hillshaded terrain model (10x vertical exaggeration) is derived from the USGS National Elevation Data 1/3 arc-second DTM. B) Hillshaded terrain model (5x vertical exaggeration, from a 9.1 m cell-size DTM – PSDEM, Finlayson, 2005) of the test area and footprints of figures presented later.**

contours derived from the DTM and a semi-transparent, display extent-adaptive color rendering of the DTM. Other hillshaded models, ranging in solar angle between 35°-65° and illuminated from opposite azimuths (110° and 290°) perpendicular to general LSB orientation (NNE-SSW) aided in the interpretation. Anthropogenic features were identified using Bing Maps. Where original LSB edges were poorly preserved, drawn limits reflect a visual interpolation based on well-preserved segments. In order to minimize MM subjectivity, footprints digitized in a first pass were subjected to multiple inspections days apart, until modifications imposed to the previous set of footprints reached a minimum. ArcMap® was used because of built-in automatic display extent-adaptive rendering. Bing Maps imagery was sourced from OpenLayers Plugin for QGIS.

Elongate partial LSBs truncated transverse to their long axis at the test area border ($n$ = 8) were included, because for (semi-)automated mapping they are indistinguishable from complete LSBs (limitation of current operational definitions). Excluding incomplete LSBs at the test area border would require either a) use of very irregular limits at the southern border of the test area, where truncated LSBs are long (e.g., 1.62 km) and closely spaced (displacing the limits in the up or downflow direction is not a solution because other LSBs would become truncated), or b) redefinition of the areas that they occupy into non-LSB terrain, changing *a priori* probability (LSB density). Potential changes in method performance after applying the latter option are assessed in the discussion section (3.7.6). Bias in morphometric statistics due to the inclusion of elongated LSBs truncated at the test area border is irrelevant for the purpose of SAM performance assessment because their morphometry falls within the range of the other LSBs.

### 3.5.3. LSB operational definition

The LSB operational definition is a pragmatic set of rules that defines LSBs in software-realized terms (ideally unambiguously). LSBs are typically described as distinctive landforms, but this has not been addressed quantitatively (what is their topographic signature?); operational definitions based on existing definitions of LSBs (e.g., d'Oleire-Oltmanns et al., 2013) thus are exploratory and potentially ambiguous. Here, a LSB morphometry knowledge-base combining expert knowledge (that LSBs are

relatively straight, elongated and highly convex hills with a high degree of parallel conformity and relatively regular surface and outline that occur within the footprints of paleo ice-sheets; Menzies, 1979; Shaw, 1983; Clark, 1993; Smalley and Warburton, 1994; Patterson and Hooke, 1995; Knight, 1997; Clark et al., 2009) with morphometric data from previous inventories (Spagnolo et al., 2012, 2014) and from MM-LSBs from a DTM of the test area, seeds a ruleset used to classify the outputs of segmentation algorithms (LSB-candidate terrain segments) into LSB and non-LSB terrain segments (Figs 3.1, 3.2). This LSB ruleset (Table 3.1) is based on measures of size (2, 7 and 8), 2D shape (3, 6), 3D shape (1, 9 and 10) and orientation (4, 5). Values for measures 3 to 10 are based on MM-LSBs in the study area. Measure 1 has been used to distinguish hills from depressions (Doctor and Young, 2013). DTM vertical resolution conditions the relief of the smallest hills that can be identified, whereas for maximum relief current data (Spagnolo et al., 2012) can be used (measure 2). Measure 3 allows distinguishing between circular and elongated hills; had the elongation (ratio of footprint length to width) of LSBs in the study area not been sampled, a minimum value of, e.g., 1.1, could be used. The use of measures 4 and 5 reflects that LSB orientation is relatively constant amongst neighboring landforms and thus potentially very discriminatory (any hill with different orientation can be ruled out). If, in a certain study area, the orientation of a cross-cutting LSB set is outside the range in orientation of non-superimposed LSBs, then rules can be specified as to exclude or separately map each set. Measure 5 allows distinguishing also between flat-topped (i.e. no ridgeline; e.g., anthropogenic structures that may persist in the DTM) and convex hilltops. Footprint outline complexity (measure 6) is used because, relative to other landforms, LSB outlines tend to be regular/smooth. Applied thresholds were constrained from examples of MM- and SAM-footprints (typically more irregular than MM-footprints) and vary with footprint elongation because outline complexity tends to increase with increasing elongation. The remaining ruleset measures (7-10) were chosen from a wider group of variables (including footprint area and perimeter, 2D ridge sinuosity, mean total slope curvature, mean longitudinal slope curvature, and standard deviation of slope) for reducing the number of false positives without significantly affecting the number of successfully mapped LSBs following filtering with measures 1-6 on preliminary versions of the NCCM and LEMM. Not to risk excluding relatively successful SAM-footprints for being somewhat wider than maximum sampled width, measure 8 allows SAM-footprints to be 25% wider than the latter. Out of

the selection of variables that made it into the ruleset (1-10), measures 9 and 10 were the least discriminative and are the least straightforward to sample. Therefore, in order to better understand if the inclusion of measures 9 and 10 in the ruleset is beneficial, two maps, one based on measures 1-8 (hereafter referred to as ruleset X) and the other on measures 1-10 (hereafter referred to as ruleset Y), were produced for each SAM method.

**Table 3.1 LSB operational definition (ruleset) and corresponding values for the test area; minimum and maximum values for measures 3-10 refer to MM-footprints in the test area**

| Measure | Rule | Minimum | Maximum |
|---|---|---|---|
| 1 – Mean topographic position index (Guisan et al., 1999) | (> ~0) LSBs are hills | 0 (NCCM); -0.2 (LEMM) | -- |
| 2 – Relief (m) | > at least 2x DTM vertical resolution & < maximum reported in the literature (worldwide) | 2 | 120 |
| 3 – Footprint elongation | > minimum | 1.83 | -- |
| 4 – Footprint orientation (°) | > minimum & < maximum | 0 / 180 | 40 / 220 |
| 5 – Ridge orientation (°) | LSBs have ridges; > minimum & < maximum | 0 / 180 | 56 / 236 |
| 6 – Footprint (outline) shape complexity index (Lindsay, 2014) | Elongation <5 | -- | 0.17 (NCCM); 0.15 (LEMM) |
| | Elongation ≥5 and <10 | -- | 0.20 (NCCM); 0.22 (LEMM) |
| | Elongation ≥10 and <20 | -- | 0.25 (NCCM & LEMM) |
| | Elongation ≥20 | -- | 0.45 (NCCM & LEMM) |
| 7 – Footprint length (m) | > minimum | 266 | -- |
| 8 – Footprint width (m) | > minimum & < maximum*1.25 | 45 | 830 |
| 9 – Standard deviation of aspect (radians) | > minimum & < maximum | 0.268 | 1.947 |
| 10 – Mean cross-sectional curvature (radians) | > minimum & < maximum | -1.43E-05 | 1.10E-04 |

Measures 1 and 6 are different between the NCCM and the LEMM (Table 3.1). The LEMM ruleset uses a lower mean topographic position index than NCCM because LEMM footprints tend to be larger than the corresponding MM-footprints (i.e. to extend

into inter-LSB terrain). This biases performance slightly in favor of LEMM, but is useful for assessing method potential (assuming that there is a solution to the over-mapping). Relative method performance was not significantly affected. The maximum allowed shape complexity index is lower and higher for the LEMM for LSBs with elongation <5 and between ≥5 and <10, because its footprint-candidate objects had smoother and more irregular outlines at these elongation values, respectively, than the footprint-candidates of the NCCM.

Footprint length, width and orientation were derived with the minimum bounding rectangle method (Napieralski and Nalepa, 2010; Dowling et al., 2015; chapter 2 of this thesis). This method was chosen because, while not being the best LSB morphometric measurement method (chapter 2), it was the most accurate and very precise (e.g., standard deviation of 1.7º in orientation) for a sample of LSBs from the Puget Lowland drumlin field and is much simpler to apply than the best method (chapter 2). Elongation corresponds to the ratio of footprint length to width (*n*:1; for a circle, *n* = 1). Ridge orientation was derived from ridges defined by thresholding a catchment area model based on the D8-flow routing algorithm (O'Callaghan and Mark, 1984). The shape complexity index is calculated as 1 - *area of footprint* / *area of footprint's convex hull* and ranges between 0 (lack of boundary concavities) and ~1. Relief is the elevation range of LSBs. Measures 8-10 are based on every cell of the LSB DTM. The minimum bounding rectangle was derived in ARCMAP®, measure 6 in Whitebox GIS (Lindsay, 2014) and the remaining measures in SAGA GIS (Olaya and Conrad, 2009).

### 3.5.4. DTM preprocessing

LSBs in the test area frequently display highly indented outlines and irregular topography (Fig. 3.4A) due to post LSB-formation processes and anthropogenic terrain modification. Notably, sets of small (from <2 m to ~10 m in height), regularly spaced (<100 m apart) transverse ridges can be superimposed on LSBs. While in some locations their texture is crisp, in others they occur as smooth undulations. Some have been interpreted as crevasse-squeeze ridges (Haugerud, 2009). Additionally, drainage reorganization and adjustment to base level changes following glacier retreat led to the truncation of some LSBs, particularly at the west and east margins of the test area. The

MM operator is able to recognize such irregularities in the DTM and draw footprints more representative of original LSB edges than present-day topography. For SAM the DTM was processed to better reflect assumptions on original LSB topography: smooth outline and texture (Fig. 3.4B). This preprocessing utilized SAGA GIS modules (italicized below) and is explained below.

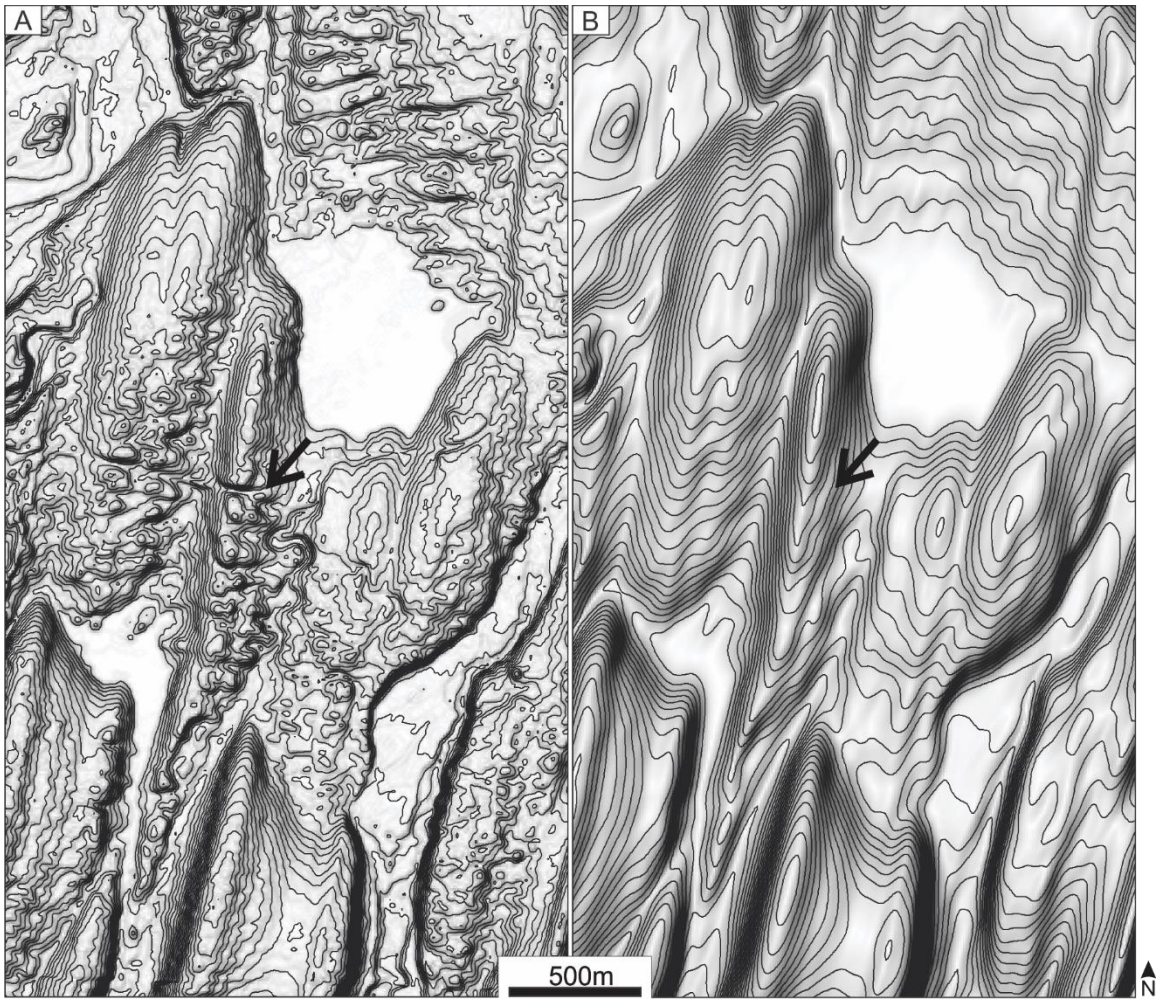


**Figure 3.4 DTM before (A) and after (B) preprocessing. Contour interval is 2 m. Arrow points to a road.**

First, the DTM was smoothed with anisotropic filters (*directional statistics for single grid*) conditioned to general LSB orientation (NNE-SSW), in the following order: filter 1) directional mean with a spatial range of 10 cells (~1/3 of minimum LSB length), first along 200°, then 20° (flipped by 180°) azimuth; filter 2) directional mean with a spatial range of 10 cells, weighted to the power of two of the inverse distance and with a

direction tolerance of 3°, first along 290º, then 110º azimuth (perpendicular to filter 1). In both filter 1 and 2, the reverse direction filtering is needed in order to reduce the geometric distortion (directional spread) generated in the first run. A *mesh denoise* operation (Sun et al., 2007) was then applied. This algorithm was selected because it is designed such that sharp features (e.g., breaks of slope) are preserved (in contrast with smoothing operators, which tend to subdue high frequencies). It was applied with a common-edge neighbourhood, an averaging threshold of 0.1, 15 iterations for normal update and 50 iterations for vertex update. These settings provided a good compromise between the level of smoothing and the loss of relevant information. In practice, differences relative to whether a typical smoothing algorithm (such as a median or a Gaussian kernel) had been used were small.

### 3.5.5. Normalized closed contour method

The NCCM assumes that each LSB footprint can be represented by a lowermost, normalized local relief (NLR) closed contour. In a top-down approach, LSB footprint objects are identified by querying a multitude of candidate objects (every NLR closed contour) against a LSB ruleset (Fig. 3.1, Table 3.1). NLR is used here as a general term for any normalized, local (neighborhood) datum relief model, and “normalized” is used as a synonym of relative.

NCCM draws on passive contouring for segmenting a NLR model into LSB-candidate objects. Passive contouring refers to the creation of contours by conversion of digital representation format (raster to vector), in contrast to active contouring, which typically refers to the recognition and delineation of edges (edge-based segmentation) (e.g., Arbelaez et al., 2011; although see Chan and Vese, 2001). Because LSBs typically are bounded by concave breaks in slope gradient, edge-based segmentation could, in principle, be used for LSB automated delineation. Though, in practice, limitations exist: the angle of curvature at LSB edges is variable – LSBs sometimes smoothly merge with the surrounding terrain and grade into one another (Heidenreich, 1964); and landforms occurring in association with LSBs (e.g., moraines) are themselves delimited by concave slope breaks.

An elevation-a.s.l. (fixed datum) contour dataset of a LSB field will contain closed contours closely matching the outlines of LSBs in relatively flat terrain. In contrast, the edges of LSBs on slopes cut across multiple contours. NLR addresses this limitation of fixed-datum contours for LSB SAM. NLR computation is a terrain detrending or flattening procedure. Local elevation minima and maxima in the original DTM are brought to common planes; one NLR contour may correspond to a range in elevation a.s.l. The NLR of a certain location (cell) *x,y* can be defined as the difference in elevation a.s.l ($\Delta z$) between *x,y* and a nearby datum (e.g., $z_{min}$), relative to maximum $\Delta z$ in the proximity of *x,y* with respect to the same datum. The datum thus varies spatially. Using $z_{min}$ as the datum, NLR varies between 0 ($z = z_{min}$) and 1 ($z = z_{max}$). The contour value is not relevant for application of the NCCM however. The position of the datum with respect to *x,y* can depend solely on the distribution of *z* within a pre-determined distance from *x,y* (as for the example given) or be morphometrically defined (e.g., base of slope). NLR has been used in previous LSB (semi-)automated mapping attempts. d'Oleire-Oltmanns et al. (2013) based their method on a NLR computed in moving windows on a terrain model excluding (flattening) topography below local (1x1 km neighborhood) median elevation (after Hillier and Smith, 2008) and Eisank et al. (2014) tested the suitability of multiresolution segmentation (Baatz and Schäpe, 2000) of an hydrology-based NLR (Böhner and Selige, 2006). None of these studies provides insights that can be used in this study for determining which type of NLR model might be more adequate for the NCCM.

### *Implementation*

The NCCM draws on test area LSB morphometry in two separate instances (Fig. 3.1): 1) for scale definition in NLR computation; and 2) for deriving some of the values for the LSB ruleset. Because the MM-dataset covers the complete test area (required for SAM performance assessment), sampling errors should be negligible; effectively, it includes the shortest, largest, most compact and most elongate LSBs as well as the range of LSB orientation. The NCCM processing flow, from NLR computation to the topologic filtering is explained below. SAGA GIS v.2.1, Grass GIS (Neteler et al., 2012; v.6.4) modules run within QGIS v.2.2 and v.2.3, Whitebox GIS v.3.2 and ArcMap® v.10.2 were used. This combination reflects author preference.

(1) NLR model computation. Four different NLR models were tested (Fig. 3.5): 1) normalized neighborhood relief (NNR) (i.e. local or relative relief; Mark, 1975) and 2) topographic position index (TPI) (Guisan et al., 1999), both computed in moving windows; 3) normalized hydrological relief (NHR) (normalized altitude of Böhner and Selige, 2006), based on a multiple direction flow routing algorithm; and 4) NHR combo (NHRC), combining NHR with a model derived from a single direction flow routing algorithm (NHR2) (the latter model after MacMillan, 2005). Whereas for NNR and TPI normalization is done relative to the minimum and mean elevation within a certain distance from the cell being transformed, respectively, for NHR and NHRC the datum approximates the base of the slope (based on drainage accumulation).

NNR was computed for each cell as

$$NNR_i = \frac{Z_i - (Zmin_{k(r)})_i}{(Zmax_{k(r)})_i - (Zmin_{k(r)})_i} \qquad \textbf{Equation 1}$$

where *i* is the cell, *Z* is elevation a.s.l. and *k* is a circular kernel (moving window) of radius *r* centered on *i*. A radius equivalent to the width of the widest LSB (664 m) was used.

TPI was computed as

$$TPI_i = Z_i - (\bar{Z}_{k(>r1<r2)})_i \qquad \textbf{Equation 2}$$

where *k* is an annulus kernel centered on *i* with inner radius *r1* and outer radius *r2*. The widths of the thinnest and of the widest LSBs were used for *r*1 (45 m) and *r*2 (664 m), respectively.

NHR is computed as

$$NHR = \frac{1}{2}\,[1 + (AD - AS)/\,AD + AS)] \qquad \textbf{Equation 3}$$

where AD and AS are normalized height above drainage culmination (cell catchment) and below summit, respectively (Böhner and Selige, 2006). These positions are based on a catchment area model derived from a multiple direction flow routing algorithm (Freeman, 1991) modified as a function of slope angle for correcting model inaccuracies

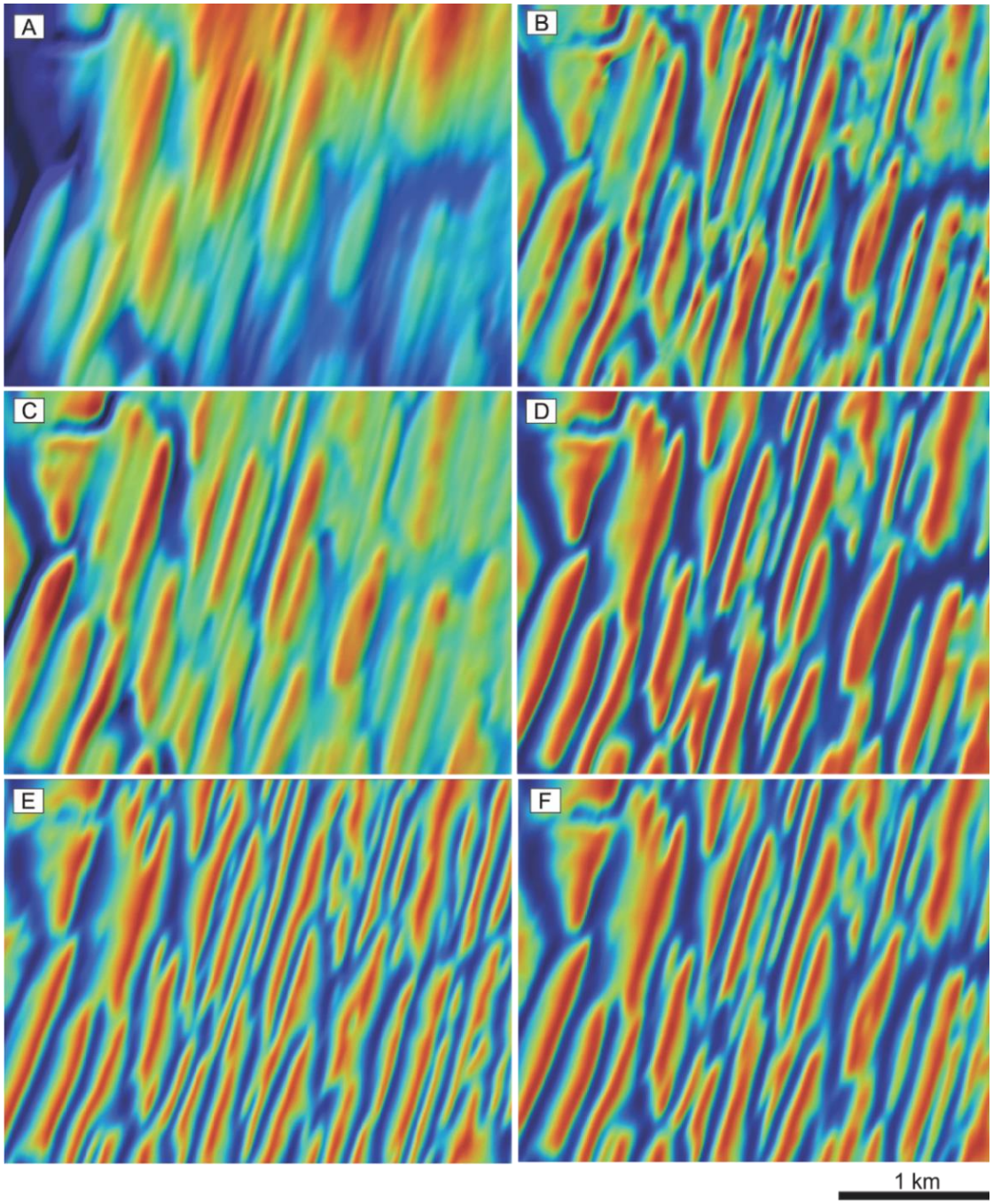


**Figure 3.5** **NLR models for part of the test area (refer to Fig. 3.3 for location). A) Preprocessed DTM; B) NNR; C) TPI; D) NHR; E) NHR2; F) NHRC. A ranges between 87-177m a.s.l.; B, D and E range between 0-1; C ranges from -4.5 to 3.2; F ranges between 0.1-1.7.**

in flat areas and used to weight relative altitudes. NHR requires setting three parameters: *w*, weighting the influence of catchment size on relative elevation (inversely

proportional); *t*, controlling the proportion of maximum accumulated flow in a cell's neighborhood that will move into the cell based on the slope between the cells (higher *t*, higher sensitivity to small elevation differences); and *e*, controlling the position of relative height maxima as a function of inclination. Values used for *w* (0.5), *t* (250) and *e* (1) were chosen after iteration using a range of values (*w* = 0.1, 0.5, 1, 2, 4 and 10; *t* = 10, 20, 100, 250 and 500; *e* = 1, 2 and 4) based on their ability to maximize model representation of the less evident swales. In order to subdue modeling artifacts (e.g., pronounced concavities and convexities in slopes), the resulting surface was subjected to a directional mean filter parallel to general LSB orientation (filter 1 of DTM preprocessing).

NHR2 was based on the D8-flow routing algorithm (O'Callaghan and Mark, 1984) and computed as

$$\text{NHR2} = CA^{-1} \,/\, (CA + CA^{-1}) \qquad \textbf{Equation 4}$$

where CA is catchment area. As for NHR, in order to subdue modeling artifacts, the resulting surface was subjected to a directional mean filter parallel to general LSB orientation. NHRC was computed as NHR * 0.75 + NHR2 * 0.25. NHR2 was given less weight than NHR due to artifacts resulting from the high sensitivity of the single direction flow routing algorithm to small changes in slope and aspect. On the other hand, weighting NHR2 less would render NHRC too similar to NHR.

(2) Contouring. Each NLR model was contoured at 0.1 equidistance. Contours were then converted from polyline to polygon geometry and resulting topological errors (intersection of polygons in relation to contours closed at the test area border) processed with ARCMAP® *repair geometry* module.

(3) Terrain segment morphometry. The LSB ruleset measures (Table 3.1) are computed for each polygon.

(4) Morphometric filtering. Closed contours discordant with the LSB ruleset values are removed. Rulesets X and Y were applied separately.

(5) Topologic filtering. This step selects which closed contour polygon in a set of superimposed polygons best represents the LSB footprint. Lone polygons and lowermost polygons from each set of superimposed polygons were labelled “LSB footprint” and the remaining polygons deleted.

### 3.5.6. Landform elements mask method

The LEMM processing flow (Fig. 3.2) can be summarized into three meta-steps (bolded in Fig. 3.2; each involving a number of sub-steps): 1) classification of the DTM into landform elements; 2) reclassification of these into A) typical LSB and B) non-LSB classes; and (3) filtering of segments composed of typical LSB elements through the LSB ruleset. A full description of the processing flow is described below. Unless otherwise noted, the processing was done with SAGA GIS.

#### *Implementation*

(1) Landform elements. The results of three methods for the classification of DTMs into landform elements were compared: 1) Wood (1996); 2) Schmidt and Hewitt (2004); and 3) Jasiewicz and Stepinski (2013) (in GRASS GIS 7). These methods classify the terrain into 6, 9 and 10 elements, respectively. Wood’s (1996) method was preferred because of a highly customizable output, a reduced number of classes and a relatively short processing time. This method classifies each cell of the DTM into flat, pit, channel, saddle, ridge or peak (Fig. 3.6). Based on a qualitative assessment of results from a range of parameter values, the following settings were applied: scale radius = 5 cells; slope tolerance for planar surface = 10°; curvature tolerance for planar surface = $5x10^{-5}$ radians. The absence or presence of pits and saddles within LSBs is very dependent on these settings. Significantly smaller scale radiuses and lower curvature tolerances would create too much detail (and vice-versa, though variable in space depending on terrain configuration). The high value of slope tolerance allowed more channel features (swales) to be defined without causing significant over-mapping.

(2) Reclassification of landform elements. First, landform elements were reclassified into two classes: elements typical of LSBs (peaks, ridges and flats);

elements absent to rare in LSBs (channels, pits and saddles). The first was then set as *null value*. The resulting layer is hereafter referred to as the inter-LSB mask.

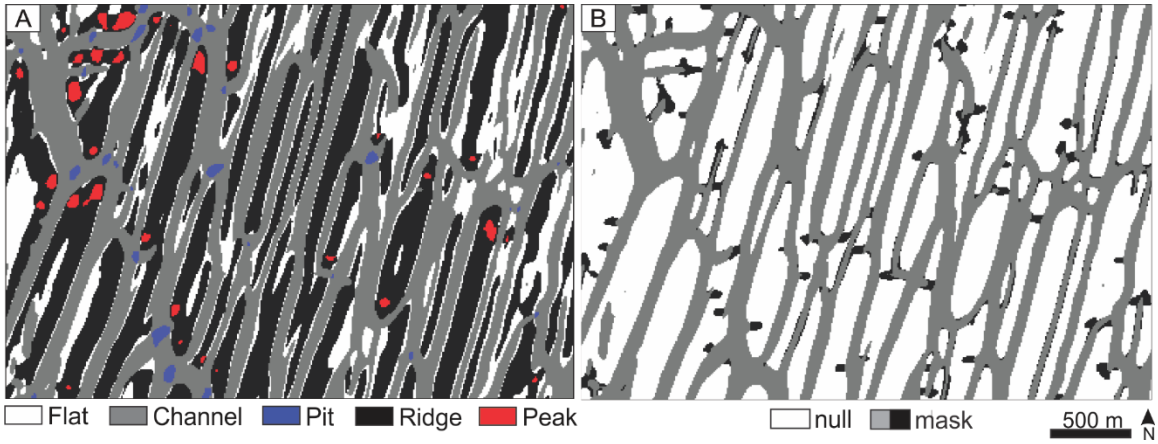


**Figure 3.6** **(A) Landform elements classification and (B) inter-LSB mask. In B, grey corresponds to the inter-LSB mask derived from the first landform elements classification and black represents the difference between that mask and processing loop 4 mask (mostly the result of the mathematical morphology filter – step 3 of LEMM processing flow). No saddle was mapped in this area.**

(3) Mathematical morphology filter – closing operation. The inter-LSB mask was subjected to cycles of isotropic dilation and erosion aimed at closing small gaps in the mask so as to increase the number of LSBs fully enclosed by it (Fig. 3.6B). Distances of 1 and 2 cells were used.

(4) Mask burning. The inter-LSB mask was reclassified to a negative value (-10, arbitrary) and summed to the preprocessed DTM. The modified DTM was then submitted to a *fill sinks* operation aimed at removing pits within LSBs, followed by a *mesh denoise* operation (Sun et al., 2007) for smoothing fine-scale topography and also counterworking the expansion of the mask into LSBs.

(5) Looping. The modified DTM (from step 4) is subjected to the landform elements classification and a new inter-LSB mask is derived (steps 1-4 are repeated). The decision on whether to stop or to re-run the loop was based on the visual (dis)similarity of the mask from the previous loop to the just-created mask and on the relationship between the amount of positive changes and unwanted artifacts in the latter.

The final mask was obtained at loop 4; the loop 5 mask was visually similar to that of loop 4. Following changes to the DTM at each loop, parameter values used for the landform elements classification also varied: loop 2 used the same parameters as loop 1 plus a vertical exaggeration of 2; and, relative to loop 2, loops 3 and 4 used different slope and curvature tolerances (20° and $3x10^{-4}$ radians, respectively).

(6) Raster to polygons. The final inter-LSB mask was inverted (class labels exchanged) in order to obtain the regions enclosed by it, then converted to polygon vector format.

(7) Polygon Simplification. A *bend simplify* operation (ARCMAP®) using a reference baseline of 500 m and fixing of topological errors was applied in order to subdue artifacts generated during the looping.

(8) Terrain segment morphometry (same as NCCM step 3). The LSB ruleset measures (Table 3.1) are computed for each polygon.

(9) Morphometric filtering (same as NCCM step 4). Closed contours discordant with the LSB ruleset are removed. Rulesets X and Y were applied separately.

### 3.5.7. Performance assessment

Method performance was evaluated with reference to the MM-dataset. The assessment was done individually for each of 10 SAM-footprint datasets: 4 (NLR models) times 2 (rulesets X and Y) applications of the NCCM, and 2 implementations of the LEMM (rulesets X and Y). Both object-oriented and cell-based measures were used (Liu et al., 2007; Clinton et al., 2010), the latter for establishing comparisons to previous studies. Object-oriented measures allow performance evaluation in terms of spatial detection (overlap) and morphometric fidelity, whereas cell-based measures ignore the latter. In order to assess the number of potentially newly identified LSBs and overdetection, each SAM-footprint without a MM-footprint was evaluated against the same terrain representations as used for MM.

The object-based performance assessment (OOPA) is based on 7 measures (Table 3.2). Two detection rates (general, morphometric) are used. The general detection rate is a 1st order indicator of method performance, akin to, although improved over, measures used to evaluate published methods (d'Oleire-Oltmanns et al., 2013; Saha et al., 2011 method, evaluated by d'Oleire-Oltmanns et al., 2013). d'Oleire-Oltmanns et al. (2013) used a detection rate where any MM-footprint intersected by a SAM-footprint seems to be considered successfully detected; for the general detection rate, a minimum overlap of 10% (of MM- by one SAM-footprint) is required and, due to the inclusion of orientation in the LSB ruleset, no successful SAM-footprint falls outside of the range in orientation of the LSBs in the test area. The morphometric detection rate rejects relationships of >1 SAM- to 1 MM-footprint and of 1 SAM- to >1 MM-footprint, and uses a minimum overlap of 50% between MM- and SAM-footprint and a maximum divergence of SAM- from MM-footprint orientation of 5º; it thus is a more constrained indicator of method success and provides a better basis for evaluating method adequacy with regard to morphometric inventorying purposes than the general detection rate; however, because different research objectives may have different quality requirements, those thresholds are somewhat arbitrary.

The difference of means index (DMI) and the correlation analysis were applied to footprint length, width, elongation and orientation. DMI was calculated separately for: all SAM- and MM-footprints (DMI-A); satisfactory (cf. morphometric detection) SAM- and all MM-footprints (DMI-B); and satisfactory SAM- and their respective MM-footprints (DMI-C). DMI-A informs about the relative extent to which false detections and non-satisfactory footprints compromise morphometric accuracy. DMI-B informs about the representativeness of satisfactory SAM-footprints.

For the cell-based assessment, the true skill statistic (TSS) (Allouche et al., 2006) and kappa (Cohen, 1960) were used. The TSS is calculated as *sensitivity* + *specificity* - 1. Sensitivity corresponds to the areal proportion of MM-footprints which is overlapped by SAM-footprints (true positives). Specificity corresponds to the proportion of non-LSB terrain not mapped as LSB; conceptually, it is different from the proportion of true negatives because mapping is done for a single feature – i.e. a detection or unary, not a binary (classification), problem, as there is no attempt to map non-LSB terrain

(background). Kappa measures the difference between the measured proportion of true positives and "true negatives" and the proportion expected to occur by chance alone. Both TSS and Kappa range from -1 to 1, values above zero indicating performance better than random.

**Table 3.2 Object-oriented performance measures**

| Measure name | Measure definition |
|---|---|
| N-rate | $(n2 \,/\, n1) * 100$<br>*n2*: number of SAM-footprints;<br>*n1*: number of MM-footprints. |
| N-new (new detections) | Number of LSB footprints mapped by the SAM method but not with MM. |
| General detection rate | $(n3 \,/\, n1) * 100$<br>*n3*: number of MM-footprints overlapped by a SAM-footprint by at least 10% of its extent;<br>*n1*: number of MM-footprints. |
| Morphometric detection rate | $(n4 \,/\, n1) * 100$<br>*n4*: number of satisfactory SAM-footprints (see text);<br>*n1*: number of MM-footprints. |
| Overdetection rate | *N-rate – general detection rate* |
| Difference of (morphometric) means index | $\sum_{i=1}^{n} \left( \frac{\mid (\bar{x}_{SAM)})_i - (\bar{x}_{MM)})_i \mid}{(\bar{x}_{MM)})_i} \right) / n * 100$<br>where $(\bar{x}_{SAM)})_i$ and $(\bar{x}_{MM)})_i$ correspond to the mean of morphometric measure *i* for the SAM- and MM-footprint dataset, respectively; and $n$ is the number of measures used. |
| (Correlation between SAM- and MM-footprint morphometry) | $r = \frac{\sum_{i=1}^{n}(x_i - \bar{x})\,(y_i - \bar{y})}{\sqrt{\sum_{i=1}^{n}(x_i - \bar{x})^2}\,\sqrt{\sum_{i=1}^{n}(y_i - \bar{y})^2}}$<br>where *r* is Pearson's correlation coefficient and *n* is the number of satisfactory SAM-footprint–respective MM-footprint (*Y* and *X*, respectively) pairs. |

## 3.6. Results

### 3.6.1. Manual mapping

MM yielded 135 LSB footprints (Fig. 3.7A), at a mean density of 1 footprint per $km^2$ and covering 22% of the test area. Footprint length, width and elongation (E) have left-skewed, high-range and high-dispersion distributions (Table 3.3). Orientation is approximately normally distributed and more consistent. Using an elongation (E) of 10 as a separation criteria (Stokes and Clark, 1999), 114 LSBs would be drumlins (E <10) and 21 would be MSGLs (E ≥10).

**Table 3.3 MM-footprint morphometry**

| Measure | Minimum | Median | Maximum | Mean | Coefficient of variation |
|---|---|---|---|---|---|
| Length (m) | 266 | 1146 | 4212 | 1213 | 0.53 |
| Width (m) | 45 | 182 | 664 | 212 | 0.60 |
| Elongation | 1.9 | 6 | 29.0 | 6.9 | 0.65 |
| Orientation (°) | 0 / 180 | 16 / 196 | 40 / 220 | 17 / 197 | 0.35 |

### 3.6.2. Object-oriented performance assessment

The object-oriented performance measures are presented in Table 3.4. Figure 3.7 presents maps from the SAM. The LEMM inventoried considerably fewer footprints (106% and 96% of the number of MM footprints for rulesets X and Y, respectively) than any of the NCCMs, and the NHRC method inventoried the largest number of footprints (Table 3.4). On average ruleset Y yielded 19 footprints less and had 1.8% lower general detection than ruleset X. The detection and overdetection rates are lowest for the LEMM_Y and highest for the NHRC_X method (Table 3.4). N-new and the general and morphometric detection rates and overdetection rate are strongly correlated with N-rate ($r$ = 0.95, 0.91, 0.94 and 0.99, respectively).

NHR, NHRC and TPI footprint datasets had the lowest, and similar, DMI-A (Table 3.4). DMI-B indicates that the TPI satisfactory (successful according to morphometric detection rate) footprints are particularly representative of the morphometry of the MM-dataset. In contrast, the correlation between the morphometry of the subsets of

footprints used in calculating DMI-C was, in general, relatively low for the TPI and higher for the LEMM (Table 3.5). On average, the LEMM footprints were larger, and the NCCM footprints smaller, than the MM-footprints (Table 3.6). All methods were relatively accurate in terms of orientation and length (Table 3.6). The large differences in footprint width explain the relatively low accuracy of elongation (Table 3.6). Regarding morphometric differences between the complete SAM- and MM-footprint datasets (Table 3.7): 1) all methods but NHR were relatively accurate (difference ≤10%) in terms of footprint orientation; and 2) the NNR and NHRC methods were accurate also for orientation and elongation, the NHR method for elongation and the LEMM for length. All DMIs had weak correlations with each other, with the detection rates and with N-rate.

**Table 3.4 Performance assessment; with the exception of N-new (number of footprints) and TSS and kappa, all values are percentages; DMI, Difference of means index; DMI-A, all SAM & all MM; DMI-B, satisfactory SAM & all MM; DMI-C, satisfactory SAM & their respective MM footprints**

| Method | Object-oriented | | | | | | | | Cell-based | |
|---|---|---|---|---|---|---|---|---|---|---|
| | N- rate | N-new | Detection rate | | Overdet-ection rate | DMI | | | TSS | Kappa |
| | | | general | morpho-metric | | A | B | C | | |
| LEMM_X | 106 | 1 | 65 | 32 | 41 | 19 | 18 | 11 | 0.47 | 0.43 |
| LEMM_Y | 96 | 1 | 65 | 31 | 30 | 18 | 19 | 11 | 0.47 | 0.44 |
| NNR_X | 162 | 7 | 84 | 41 | 79 | 21 | 15 | 14 | 0.37 | 0.44 |
| NNR_Y | 150 | 7 | 81 | 40 | 69 | 20 | 15 | 14 | 0.37 | 0.43 |
| TPI_X | 141 | 4 | 75 | 41 | 66 | 17 | 3 | 9 | 0.44 | 0.48 |
| TPI_Y | 120 | 3 | 71 | 41 | 49 | 15 | 2 | 9 | 0.44 | 0.48 |
| NHR_X | 126 | 6 | 79 | 38 | 47 | 16 | 5 | 10 | 0.45 | 0.48 |
| NHR_Y | 117 | 4 | 78 | 39 | 39 | 15 | 4 | 10 | 0.44 | 0.48 |
| NHRC_X | 198 | 12 | 90 | 56 | 108 | 17 | 14 | 12 | 0.48 | 0.49 |
| NHRC_Y | 181 | 12 | 87 | 56 | 93 | 15 | 14 | 11 | 0.48 | 0.49 |

X and Y refer to the LSB ruleset used. Underlined and bolded numbers are the two lowest and the two highest values, respectively, for each measure.

### 3.6.3. Cell-based performance assessment

With the exception of NNR, all TSS and kappa values fall within the moderate accuracy range (0.41-0.60, after Landis and Koch, 1977) (Table 3.4). The two statistics

agree on the best performer (NHRC method) and on a worst performer (NNR method). On the other hand, whereas according to kappa the LEMM performed similarly to the NNR method, based on TSS it is the second best method. Differences between rulesets X and Y are small.

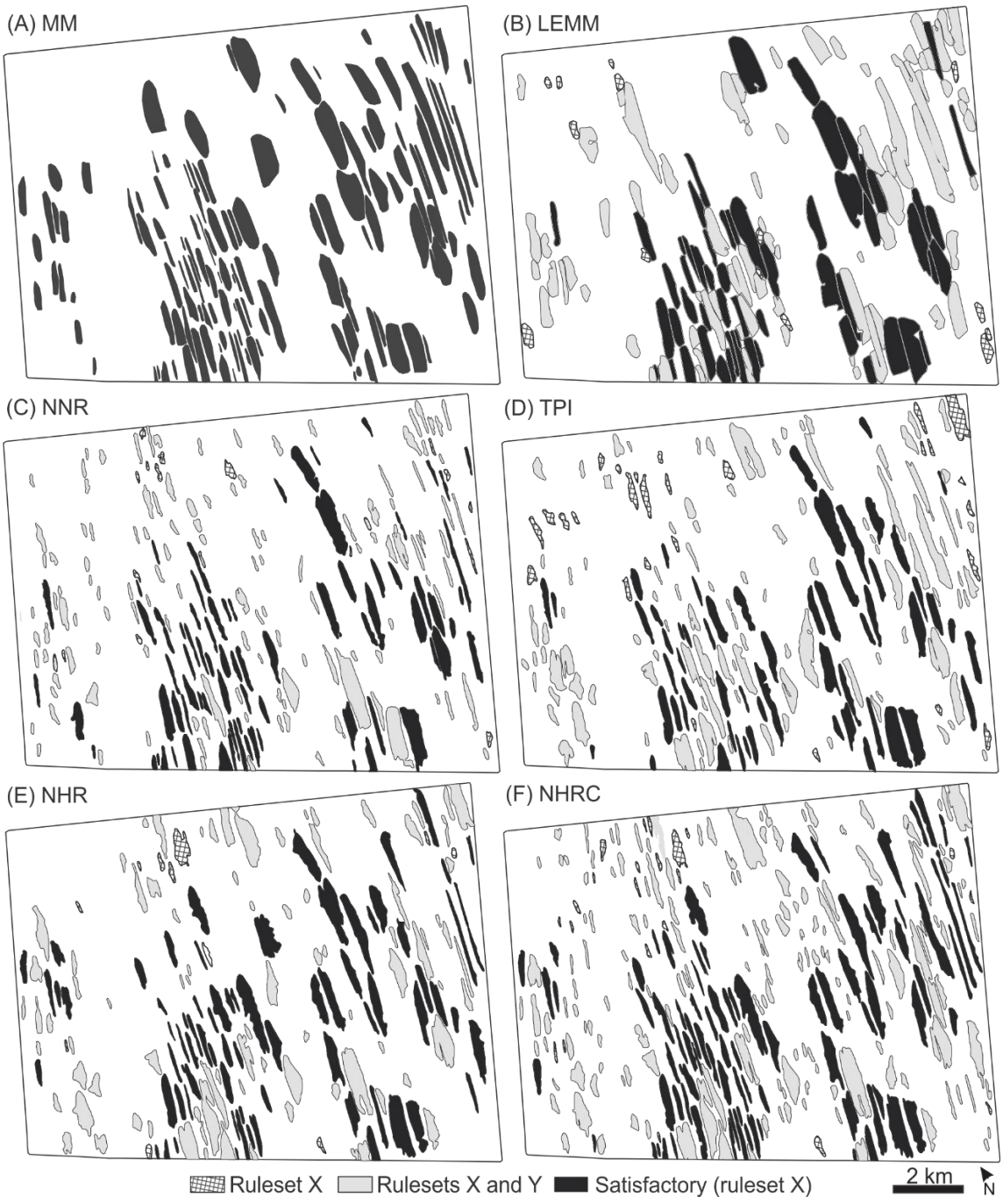


**Figure 3.7 MM-footprints (A) and SAM-footprints (B-F).**

**Table 3.5** **Correlation (Pearson's coefficient) of footprint morphometry measures between satisfactory SAM-footprints and their respective MM-footprints (DMI-C)**

| Method | Orientation | Length | Width | Elongation |
|---|---|---|---|---|
| LEMM_X | 0.82 | **0.88** | **0.97** | **0.88** |
| LEMM_Y | 0.82 | **0.88** | **0.97** | **0.88** |
| NNR_X | **0.93** | **0.88** | 0.77 | 0.78 |
| NNR_Y | **0.91** | 0.87 | 0.76 | 0.79 |
| TPI_X | 0.87 | 0.87 | 0.81 | 0.67 |
| TPI_Y | 0.86 | 0.87 | 0.81 | 0.66 |
| NHR_X | 0.79 | **0.88** | 0.85 | 0.83 |
| NHR_Y | 0.75 | **0.88** | 0.85 | 0.80 |
| NHRC_X | 0.86 | 0.85 | 0.85 | 0.86 |
| NHRC_Y | 0.84 | 0.85 | 0.85 | **0.89** |

Underlined and bolded numbers are the two lowest and the two highest values, respectively, for each measure.

**Table 3.6** **Morphometric differences (% difference of SAM-footprints mean relative to MM-footprints mean) between satisfactory SAM-footprints and their respective MM-footprints (DMI-C)**

| Method | Length | Width | Elongation | Orientation | DMI-C |
|---|---|---|---|---|---|
| LEMM_X & Y | 9 | 18 | -14 | 2 | 11 |
| NNR_X & Y | -3 | -23 | 26 | 2 | 14 |
| TPI_X & Y | -3 | -19 | 12 | 2 | 9 |
| NHR_X & Y | -2 | -18 | 18 | 1 | 10 |
| NHRC_X / Y | 6 / 7 | -15 | 23 / 22 | 1 | 12 / 11 |

**Table 3.7** **Morphometric differences (% difference of SAM-footprints mean relative to MM-footprints mean) between the complete datasets of SAM- and MM-footprints (DMI-A)**

| Method | Length | Width | Elongation | Orientation | DMI-A |
|---|---|---|---|---|---|
| LEMM_X / Y | -8 / -1 | 30 / 34 | -39 / -36 | -1 / 0 | 19 / 18 |
| NNR_X / Y | -37 / -35 | -38 / -37 | -7 / -4 | 4 / 4 | 21 / 20 |
| TPI_X / Y | -27 / -23 | -16 / -15 | -23 / -20 | -3 / -2 | 17 / 15 |
| NHR_X / Y | -21 / -19 | -9 / -8 | -16 | 16 | 16 / 15 |
| NHRC_X / Y | -28 / -25 | -30 / -27 | -4 / -3 | 8 / 6 | 17 / 15 |

## 3.7. Discussion

### 3.7.1. DTM preprocessing

DTM preprocessing is an important step for LSB SAM because, due to post-formational modification, present (recent) topography may depart significantly from original (pristine) subglacial topography (Finlayson, 2013). In the test area, LSBs frequently display highly indented outlines and irregular topography, and sometimes are truncated by natural (rivers) or anthropogenic features (roads), whereas original LSB outlines and topography are thought to be regular and smooth. Relatedly, the original DTM was very noisy and in many areas unsuitable for LSB SAM. DTM preprocessing using anisotropic (LSB orientation-constrained) smoothing fundamentally changed this (Figs 3.4, 3.8). This study indicates that SAM of LSBs is possible even in terrains with a high degree of post-LSB formation modification.

### 3.7.2. Object-oriented performance assessment

SAM-method performance was variable; no single method scored best in all measures (Table 3.4). Determining which methods performed, on balance, better and worse based on object-oriented measures requires to jointly consider detection and overdetection and to account for reference data (MM-dataset) density (e.g., prevalence, the proportion of test area covered by LSBs; i.e. *a priori* probability). For example, alone, a general detection of 100% cannot be used to conclude that the method performed perfectly; only if overdetection was 0%. On the other hand, considering a value of 100% for both general detection and overdetection, and imagining that LSBs were all the same size, only for prevalences below 50% (lower probability for detection than overdetection) could the method be considered better than random. These examples are simplifications and require postulating that detection, as defined for the general detection rate, is a direct indicator of SAM correctness, but illustrate the basis for conclusions presented below well. It is important to note also that, when morphometric fidelity is taken into account, a method can be better than random even if detection and overdetection are the same and prevalence is 50%.

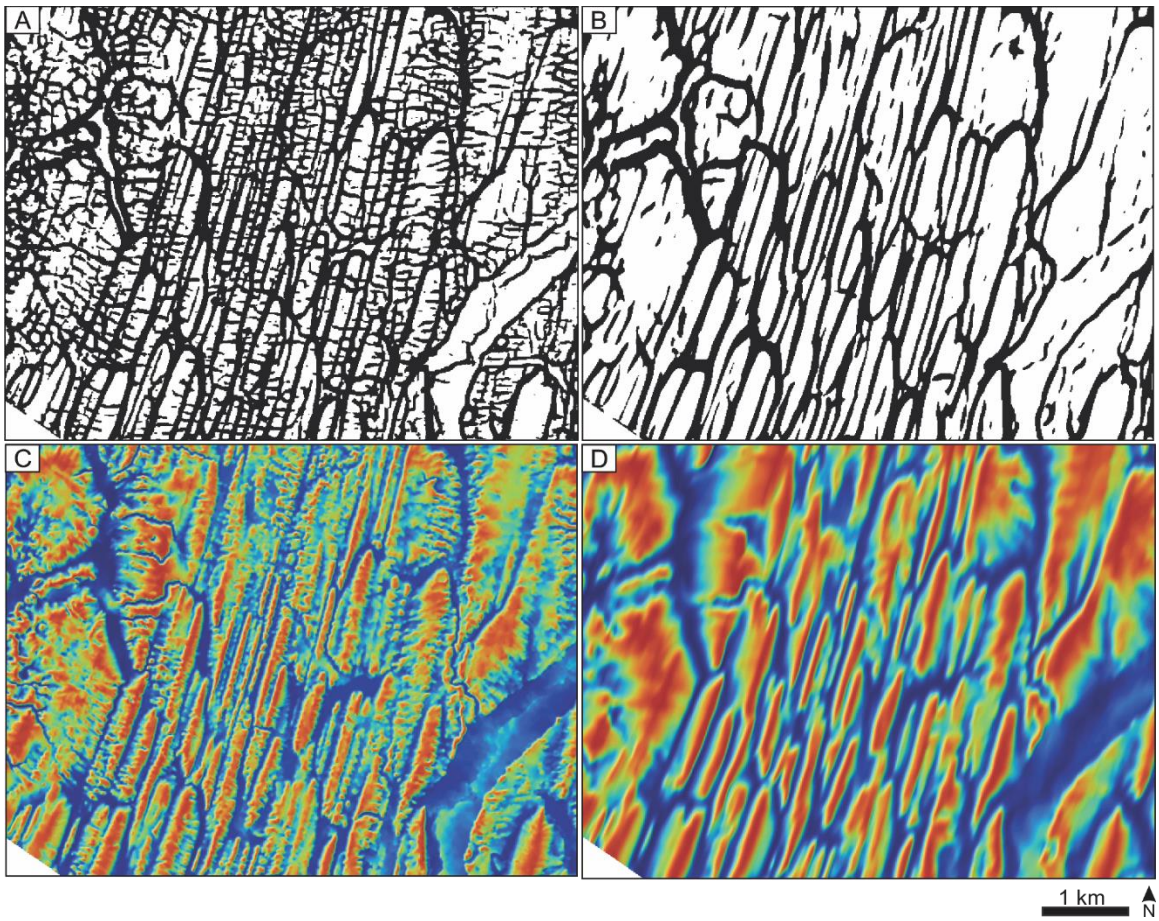


**Figure 3.8** **Inter-LSB mask and NHR derived from the original DTM (A and C, respectively) and from the preprocessed DTM (B and D, respectively). C and D vary between zero (dark blue) and one (red). Both A and B, and C and D were computed with the same parameters (the inter-LSB mask from the first loop in the LEMM processing flow and section 3.5.5, respectively). The original DTM was very noisy and neither A nor C would be adequate inputs for SAM.**

Figure 3.9 ranks methods based on the ratio of general detection to overdetection. The NHRC was the only method with lower detection than overdetection (0.83:1 and 0.94:1 for rulesets X and Y, respectively), but in a proportion still well above the prevalence of LSBs in the test area (0.22:1). In every method, ruleset Y has a larger ratio than ruleset X, indicating that the inclusion of topographic texture (ruggedness) measures in the LSB ruleset is advantageous – the decrease in detection from X to Y was always small (maximum and mean of -4% and -2.1% for general detection, respectively) and outweighed by a decrease in overdetection (mean = -11.9%) (Table

3.4). For a classification of overall method performance, an index was computed as: *general detection* * ((*general detection* / *overdetection* - 0.22) / 2) * 0.5 + *morphometric detection* * (*morphometric detection* / *morphometric overdetection*) * 0.5. Morphometric overdetection was computed as: *N-rate* - *morphometric detection*. For the ratio of general detection to (general) overdetection, values of 0.22 (prevalence of LSBs in the study area) and 2.22 are valued 0% and 100%, respectively. The NHR_Y and LEMM_Y, and the NNR_X and NHRC_X, arise as the best and worst methods, respectively (Table 3.8). The NHR_Y was one of the best methods also according to the DMIs (lowest (best) DMI-A together with the TPI and NHRC, and 2nd lowest DMI-B and DMI-C; Table 3.4).

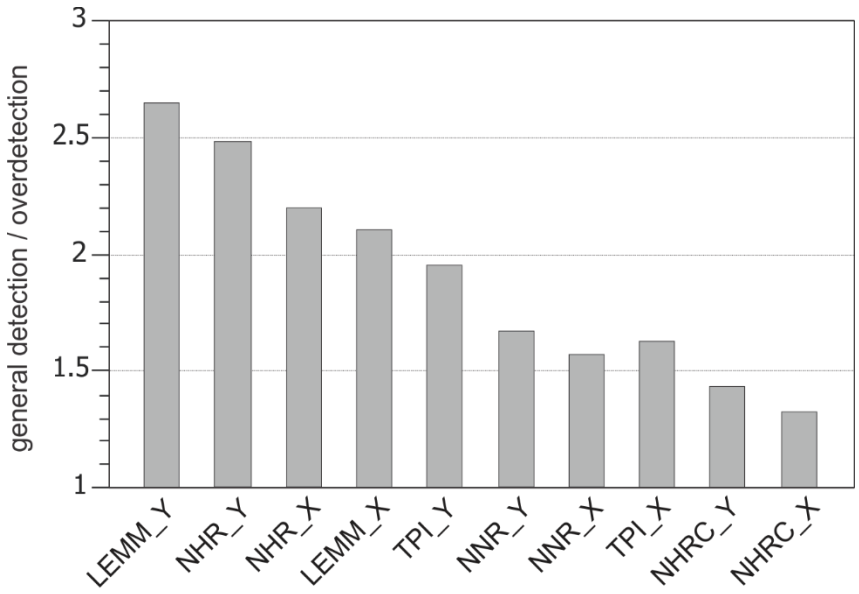


**Figure 3.9 SAM-methods ratio of general detection to overdetection.**

The relative success of the LEMM is related to the short spacing between LSBs in the test area; LEMM will perform relatively poorly where LSBs are more spaced apart. The LEMM has a processing flow which is more dependent on study area specificities and user input than the NCCM and thus is less transferrable than the latter. Other terrains and DTMs with different cell sizes would require careful re-evaluation of the processing flow. The overestimation of footprint size (Tables 3.6, 3.7) reflects limitations of the land-form elements classification as a segmentation procedure – channels often are at lower elevations and some distance away from the MM-edges (breaks-of-slope) of LSBs. These are reasons to conclude that the LEMM is inferior to the NCCM.

**Table 3.8 Overall performance index**

| Method | Performance index (%) |
|---|---|
| LEMM_X / Y | 29 / 39 |
| NNR_X / Y | 25 / 26 |
| TPI_X / Y | 26 / 33 |
| NHR_X / Y | 37 / 44 |
| NHRC_X/ Y | 25 / 28 |

False detections were mainly related to artifacts resulting from NLR modelling and anisotropic smoothing (e.g. “streamlining” of non-LSB ridges) of both the original DTM and NLR model (NHR and NHRC) (issue exacerbated by the high-degree of post LSB-formation terrain modification, which is common in drumlin fields), and to limitations of the LSB ruleset, which did not exclude convex upper sections of some non-LSB hills. The LSB ruleset was limited also in its ability to screen out partial (truncated) LSBs, which may emulate the morphometry of complete LSBs; this is particularly relevant when inventorying morphometry, but has no obvious solution (besides manual deletion of SAM-footprints). The tested NLR models substantially differ from the ideal surface, where inter-LSB areas (swales) would be homogeneous and similar in value; swales in the NLR models frequently were not flat and occur at different NLR levels. The reduced dimension of the NCCM satisfactory footprints (closed contours) relative to MM-footprints (Table 3.6) reflects this. SAM-footprints tend to be smaller than MM-footprints because the lowest contours conformant to the LSB ruleset typically occur above the concave slope break at the base of LSBs (Fig. 3.10). One other factor contributing to the smaller size of SAM-footprints is the interpolation or generalization conducted in the MM; while MM tends to pass over post-formational concavities (indentations) in current LSB outlines, SAM was based on a DTM of recent topography where post-formational topographic features, though subdued by the DTM preprocessing, are present. With improvements to NLR modelling, a rule relative to NLR contour value can be used to exclude hilltops of non-LSB hills (larger value than the lowest ruleset-conformant closed contour in LSBs).

The overdetection of the NHRC method was very high (Table 3.4) because the NHR2 model is particularly sensitive to small changes in terrain aspect and slope. While the NHR generalizes original topography, the NHR2 accentuates terrain variability,

facilitating mapping of thin LSBs missed by the NHR, but also creating many artifacts. This contrast is related to differences in the flow routing algorithms used: multiple (NHR) vs. single (NHR2) flow path direction.

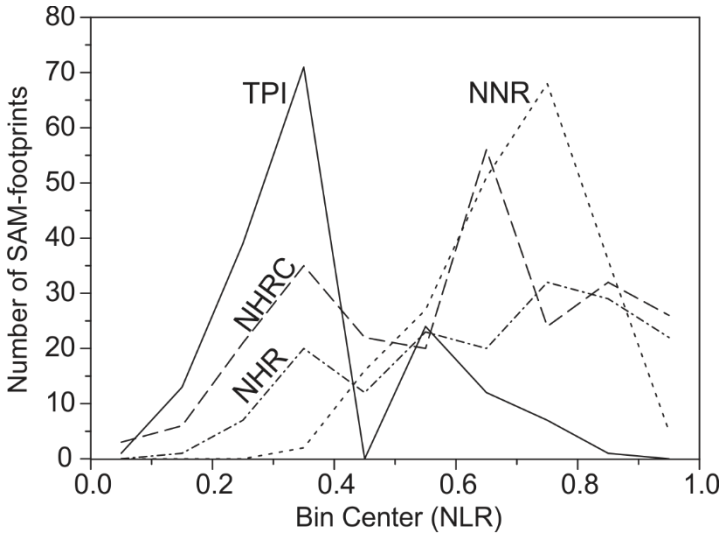


**Figure 3.10 Statistical distribution of SAM-footprints' (closed contours) NLR value. TPI and NHRC scales were normalized between 0-1. The relatively low values of TPI are related to TPI formula (i.e. mean, instead of minimum, elevation is the reference).**

### 3.7.3. Cell-based performance assessment

The cell-based performance measures (Table 3.4) were less discriminative between methods and partially disagree with the overall performance index (Table 3.8). Essentially, the differences result from the TSS and kappa being based solely on spatial overlap. The NHRC was the best method according to both the TSS and kappa because, in terms of area, differences in overdetection (commission errors) relative to the other methods were not as pronounced as in the object-oriented assessment (3% difference in commission errors vs. 54% difference in overdetection rate between the NHRC_Y and NHR_Y methods); i.e. NHRC false positives were relatively small in size. Inversely, the LEMM, which had the lowest detection and overdetection in the object-oriented assessment, obtained the highest sensitivity and commission. Cell-based measures are generally inappropriate for assessing the performance of object-based

methods. In this study they are useful for establishing comparison to previous methods (section 3.7.4).

For LSBs on relatively flat terrain, basing mapping on contour datasets directly extracted from the preprocessed DTM may lead to higher accuracy than using NLR contours. Variable DTM preprocessing based on a classification of the test area into morphometric units (landform elements) may reduce preprocessing artifacts and facilitate NLR modelling. Excluding regions where no LSBs occur or post-LSB formation processes profoundly changed original subglacial topography may considerably reduce overdetection and consequently improve performance; we tested this (Fig. 3.11; Tables 3.9, 3.10). The mask was drawn manually based on hillshaded terrain models; it encloses highly incised terrain, flats (glacial outwash and Holocene alluvium – Haugerud, 2009) and irregular surfaces (kame-kettle topography), as well as significantly modified LSBs adjacent to, or within, those areas. The performance index significantly rises for every method due to a decrease in overdetection, the difference being largest for the NHRC method, and the NHR_Y and NNR_X become the best- and worst-performing methods by a larger margin, respectively (Tables 3.9, 3.10). Importantly, a high degree of automation is possible for masking out areas where LSBs probably do not occur or will be too degraded (e.g., floodplains and highly incised terrain; e.g., Gallant and Dowling, 2003; Stout and Belmont, 2014), and this can be enhanced by the use of surficial geology data (e.g., areas covered by Holocene alluvium can be readily masked out).

### 3.7.4. Comparison to previous methods

A comparison to results of Saha et al. (2011), d'Oleire-Oltmanns et al. (2013) and Eisank et al. (2014) is discussed below. It is important to note that the same method will tend to perform differently in different terrains and that validation datasets of the same area prepared by different interpreters may be significantly different (subjectivity of MM).

Saha et al. (2011) did not explain the criteria used to determine the "80 most closely matched drumlins that were clearly identified in both datasets [MM- and SAM-footprints]" and did not include overdetection or cell-based measures. d'Oleire-Oltmanns

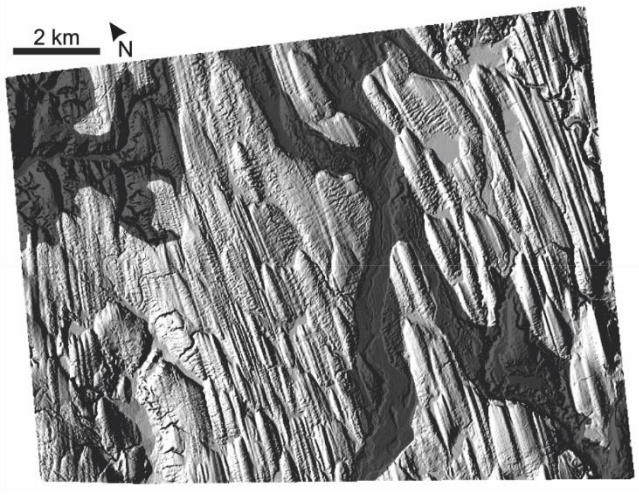


**Figure 3.11** **Mask (dark grey) of regions where LSBs do not occur or are much degraded.**

**Table 3.9** **Overall performance index after the exclusion of regions where LSBs do not occur or are much degraded (Fig. 3.11)**

| Method | Performance index (%) | Difference |
|---|---|---|
| LEMM_X / Y | 44 / 53 | +14 / +14 |
| NNR_X / Y | 32 / 34 | +7 / +7 |
| TPI_X / Y | 40 / 47 | +14 / +14 |
| NHR_X / Y | 52 / 62 | +15 / +18 |
| NHRC_X / Y | 41 / 47 | +16 / +19 |

**Table 3.10** **SAM-method performance after the exclusion of regions where LSBs do not occur or are much degraded (Fig. 3.11); numbers within brackets represent changes relative to values in Table 3.4 (no mask)**

| Method | Overdetection (%) | TSS | Kappa |
|---|---|---|---|
| LEMM_Y | 22 (-8) | 0.49 (+0.1) | 0.47 (+0.3) |
| NNR_Y | 55 (-14) | 0.38 (+0.1) | 0.45 (+0.2) |
| TPI_Y | 34 (-15) | 0.45 (+0.1) | 0.50 (+0.2) |
| NHR_Y | 27 (-12) | 0.45 (+0.1) | 0.50 (+0.2) |
| NHRC_Y | 56 (-37) | 0.50 (+0.2) | 0.52 (+0.3) |

et al. (2013) estimated Saha et al.'s (2011) method detection rate to be ~88% (of 129 MM-drumlins). Based on these figures and on the number of SAM-footprints (111), the overdetection rate (*N-rate – detection rate*) of Saha et al.'s (2011) method would be -2% (111 / 129 * 100 - 88). The low overdetection rate results from their SAM-footprints being

frequently very large, there being cases where one SAM-polygon indiscriminately covers more than five MM-footprints (their Fig. 8); counting relationships of 1 SAM-footprint to >1 MM-footprint as only one successful detection would reveal that Saha et al.'s (2011) method performed poorly. Additionally, as previously mentioned (section 3.5.7), d'Oleire-Oltmanns et al. (2013) detection rate is different from the general detection rate used here; in that study, every MM-footprint intersected by a SAM-footprint is considered detected, whereas here a minimum spatial overlap of 10% (by a single SAM-footprint) was used. The "intersection rate" (to distinguish it from the general detection rate) is highest (93%) for the NHRC_X method.

d'Oleire-Oltmanns et al. (2013) also used cell-based measures (Table 3.11) to assess performance. The NHRC_X method apparently outperforms their method (Table 3.11). However, it needs to be noted that their method uses an unsupervised operational definition and that their MM criteria seems to differ from the one used here. From visual inspection of their figure 1, it seems that multiple LSBs were represented with a single footprint and that, in some cases, outlines were drawn above LSB edges.

**Table 3.11 Performance comparison between d'Oleire-Oltmanns et al. (2013) method and the NHR and NHRC methods; best-scoring method in each measure is also given; all values are percentages**

| Method | Sensitivity[1] | Producer accuracy[2] | Commission (overdetection)[3] | Intersection rate[4] |
|---|---|---|---|---|
| d'Oleire-Oltmanns et al. | 58 | 61 | 39 | 88 |
| NHR_X | 53 | 65 | 35 | 84 |
| NHRC_X | 59 | 62 | 38 | 93 |
| Best score | 64 (LEMM_X) | 72 (NNR_Y) | 28 (NNR_Y) | 93 (NHRC_X) |

[1] User accuracy; [2] percent of SAM-footprints total area which overlaps MM-footprints; [3] inverse of producer accuracy; [4] detection rate of d'Oleire-Oltmanns et al. (2013) (any partially overlapped MM-footprint is considered detected)

Eisank et al. (2014) report a minimum *miss rate* of ~0.52 and an *area fit index* (Lucieer and Stein, 2002) always in excess of ~0.55 (their Figs 5 and 6). The *miss rate* is similar to the inverse of the general detection rate, ranging here from 0.35 (LEMM) to 0.10 (NHRC). The area-weighted average *area fit index* for the NHRC_X method is 0.04. For both measures, lower values correspond to better performance.

The NCCM, besides performing relatively well, may have more potential for improvement than previous methods. This study supports that NLR is a suitable terrain parameter for the (semi-)automated mapping of LSBs (d'Oleire-Oltmanns et al., 2013; Eisank et al., 2014), but also that region-based segmentation is not a pre-requisite for success; in fact, as mentioned earlier, since LSBs are topographically complex and variable and currently are not well represented by a single terrain parameter(ization), using a region-based segmentation (delineation of internally homogeneous objects) for extracting LSBs as single objects is counterintuitive. Additionally, unlike previously used segmentation algorithms, contouring, besides relatively simple, is intrinsically multi-scale; for example, satisfactory footprints from the NHRC_X method ranged in length from 341 m to 3958 m. Regarding cost of implementation, whereas previous methods were based on very costly software (eCognition©), existent opensource GIS software is fully adequate for applying the NCCM.

The type of operational definition used here is parsimonious: visual discovery of morphometric extremes followed by ruleset definition is a fast procedure (maybe one or two days of work for thousands of LSBs); and using case study-constrained measures improves performance (less false detections) relative to unsupervised definitions. Most of the LSB ruleset measures used here should be transferrable to other areas. Additionally, separate rulesets can be used for separately mapping LSBs of specific shapes or dimensional range, eventually improving overall performance. In terms of scale information for DTM preprocessing (e.g., scale of smoothing) and terrain attribute computation, while manual sampling can be slow relative to automated procedures (e.g., Drăguţ et al., 2010), it is not laborious and the latter may not be able to separate the signal of LSBs from the rest of the terrain (dependent on the geomorphology of the area: which other landforms occur along with LSBs and how frequent are they?).

### 3.7.5. Methodology limitations

Uncertainty in the validation dataset (MM-footprints) related to the subjectivity of visual interpretation and MM induces uncertainty in computed performance. Different interpreters may map a different number of LSBs and the same LSB differently. For better constraining method performance, methods can additionally be tested on

synthetic DTMs for which the exact number of LSBs in the area is known and where LSB topography is simplified. Hillier et al. (2014) and Eisank et al. (2014) (after Hillier and Smith, 2012) used DTMs with synthetic drumlins with this goal. The DTMs used in these studies were generated by manually mapping drumlin footprints, removing the corresponding drumlins from the original DTM, modelling new drumlin surfaces based on extracted data and placing them at random positions in the DTM without the original drumlins. Being rooted on the visual interpretation of real topography, these DTMs still are limited tools for the assessment of actual method performance (e.g., would different interpreters manually map and remove the same drumlins from the original DTM?). Eliminating subjectivity in the reference dataset would be best done using fully synthetic (simulated) DTMs or synthetic LSBs on real terrain that did not have LSBs (drumlins and mega-scale glacial lineations). Here, bias related to the potential incompleteness of the MM-footprint dataset is small and does not affect conclusions, because: 1) all SAM-methods were evaluated with regard to the same reference data; 2) the MM-dataset was constructed through several iterations, towards the end of which changes in the total number of mapped LSBs was small. An indication of potential MM-dataset incompleteness is given by N-new (number of LSBs mapped by the SAM method but not with MM), which was largest for NHRC_X&Y (12, 8 more than NHR_Y), though this measure too is based on visual interpretation. Re-computing the general detection rate taking into account N-new (adding N-new to both the number of detected MM-footprints and the total number of MM-footprints) would raise detection by 1% for all methods but the LEMM (0%).

As explained in section 3.5.2, elongate partial footprints of LSBs truncated transverse to their long axis at the test area border ($n$ = 8) were included in the reference dataset. In order to assess differences in performance relative to whether those LSBs had not been included, Kappa and TSS were recomputed for the NHR_Y after deletion of all MM-footprints truncated at the border and of the SAM-footprints that would not have been mapped was it not for the presence of the test area border. Differences are minor: Kappa changes from 0.480 to 0.483 and TSS from to 0.443 to 0.439.

## 3.8. Conclusion

This study presents and compares two object-based methods for the semi-automated extraction of positive-relief, longitudinal subglacial bedform (LSB) footprints from digital terrain models (DTMs). Tests are conducted on a 139.5 $km^2$ area located in the Puget Lowland drumlin field, WA, USA. Method performance is evaluated against a manually mapped footprint dataset. The normalized closed contour method (NCCM) is based on ("passive") contouring (raster to vector conversion) of a normalized local relief surface (dealing with LSBs on slopes) and the landform elements mask method (LEMM) on the classification of landform elements derived from the DTM. For both methods, identification of LSB segments was based on a supervised ruleset. The NCCM was separately applied to 4 different NLR models, two computed in moving windows and two hydrology-based.

Departure of present-day topography from original LSB topography (regular outline and smooth texture) strongly limited the suitability of the original DTM for LSB automated mapping. DTM preprocessing with isotropic and LSB orientation-constrained smoothing (a novelty) drastically increased DTM suitability, showing that even terrains with a high degree of post-LSB formation modification are suitable for SAM.

This study supports that NLR is a suitable terrain parameter for LSB automated mapping (d'Oleire-Oltmanns et al., 2013; Eisank et al., 2014), but also shows that multiresolution segmentation (Baatz and Schäpe, 2000), which all previous LSB SAM methods (Saha et al., 2011; d'Oleire-Oltmanns et al., 2013; Eisank et al., 2014) depend on, is not a pre-requisite for method success. A hydrology-based NLR (NHRC) combining a relief model derived from a multiple direction flow routing algorithm (Böhner and Selige, 2006) with a model from a single direction algorithm had the highest general detection rate (90%, better than equivalent measures in published methods), morphometric detection rate (56%), True Skill Statistic (0.48) and kappa (0.49). However, NHRC had also the highest overdetection (38% in terms of area). Based on an index combining the general detection rate with the morphometric detection rate, each weighted by the corresponding ratio of detection to overdetection, Böhner and Selige's (2006) NLR model (NHR), LEMM and NHRC arise as the best, second-best and worst

methods, respectively. Detection and overdetection need to be analysed jointly, but neither Saha et al. (2011) nor d'Oleire-Oltmanns et al. (2013) present object-oriented overdetection figures. Future studies should also incorporate *a priori* probability (density of LSBs in the study area) in the performance assessment.

The LEMM worked better than the NCCM where LSBs are closely spaced. The LEMM requires more user input and is more dependent on study area specificities, and thus is less transferrable, than the NCCM. The NCCM has more possibility for improvement than published methods. Previous methods were based on very costly software (eCognition®), whereas existent opensource software is fully adequate for the NCCM. Using a region-based segmentation (delineation of internally homogeneous objects) for extracting LSBs as single objects is conceptually counterintuitive because, currently, LSBs are not well-represented by a single terrain parameter(ization). Contouring, unlike multiresolution segmentation, is intrinsically multi-scale and thus does not require *a priori* information on the scale of the objects to be mapped.

Reducing artifacts generated during DTM preprocessing and NLR modelling (such as by applying a spatially variable DTM preprocessing based on a classification of the terrain into land-form elements), further refining the LSB operational definition (mining for terrain parameters on which LSBs have a signature) and using contours directly derived from the preprocessed DTM for mapping LSBs on relatively flat terrain, may improve NCCM performance. Tests on fully synthetic DTMs would be useful in the future to better isolate sources of error and determine absolute method performance more exactly (no subjectivity in validation dataset).

## 3.9. References

Aario, R., 1977. Associations of flutings, drumlins, hummocks and transverse ridges. GeoJournal 1(6), 65-72.

Allouche, O., Tsoar, A., Kadmon, R., 2006. Assessing the accuracy of species distribution models: prevalence, kappa and the true skill statistic (TSS). Journal of applied ecology 43(6), 1223-1232.

Arbelaez, P., Maire, M., Fowlkes, C., Malik, J., 2011. Contour detection and hierarchical image segmentation. Pattern Analysis and Machine Intelligence, IEEE Transactions on 33(5), 898-916.

Baatz, M., Schäpe, A., 2000. Multiresolution Segmentation – an optimization approach for high quality multi-scale image segmentation. In: Strobl, Blaschke, Griesebner (Eds), Angewandte Geographische Informationsverarbeitung XII, Wichmann-Verlag, Heidelberg, pp. 12-23.

Blaschke, T., 2010. Object based image analysis for remote sensing. ISPRS journal of photogrammetry and remote sensing 65(1), 2-16.

Blaschke, T., Lang, S., Lorup, E., Strobl, J., Zeil, P., 2000. Object-oriented image processing in an integrated GIS/remote sensing environment and perspectives for environmental applications. Environmental information for planning, politics and the public 2, pp 555-570.

Böhner, J., Selige, T., 2006. Spatial prediction of soil attributes using terrain analysis and climate regionalisation. In: Böhner, J., Mccloy, K. R., Strobl, J. (Eds.): SAGA–Analyses and Modelling Applications. Göttinger Geographische Abhandlungen 115, 13-28.

Bue, B. D., Stepinski, T. F., 2007. Machine detection of Martian impact craters from digital topography data. Geoscience and Remote Sensing, IEEE Transactions on 45(1), 265-274.

Chan, T. F., Vese, L. A., 2001. Active contours without edges. Image processing, IEEE transactions on 10(2), 266-277.

Clark, C. D., 1993. Mega-scale glacial lineations and cross-cutting ice-flow landforms. Earth Surface Processes and Landforms 18(1), 1-29.

Clark, C. D. 2010. Emergent drumlins and their clones: from till dilatancy to flow instabilities. Journal of Glaciology 56(200), 1011-1025.

Clark, C. D., Hughes, A. L., Greenwood, S. L., Spagnolo, M., Ng, F. S., 2009. Size and shape characteristics of drumlins, derived from a large sample, and associated scaling laws. Quaternary Science Reviews 28(7), 677-692.

Clinton, N., Holt, A., Scarborough, J., Yan, L., Gong, P., 2010. Accuracy assessment measures for object-based image segmentation goodness. Photogrammetric Engineering and remote sensing 76(3), 289-299.

Cohen, J., 1960. A Coefficient of Agreement for Nominal Scales. Educational and Psychological Measurement 20, 37-46.

d'Oleire-Oltmanns, S., Eisank, C., Drăguţ, L., Blaschke, T., 2013. An object-based workflow to extract landforms at multiple scales from two distinct data types. Geoscience and Remote Sensing Letters, IEEE 10(4), 947-951.

Davis, W.M., 1884. Drumlins. Science 4, 418–420.

de Carvalho, O. A., Guimarães, R. F., Montgomery, D. R., Gillespie, A. R., Trancoso Gomes, R. A., de Souza Martins, É., Silva, N. C., 2013. Karst Depression Detection Using ASTER, ALOS/PRISM and SRTM-Derived Digital Elevation Models in the Bambuí Group, Brazil. Remote Sensing 6(1), 330-351.

Dikau, R., Brabb, E. E., Mark, R. M., 1991. Landform classification of New Mexico by computer. US Department of the Interior, US Geological Survey (1991) Open-file report.

Doctor, D.H., Young, J.A., 2013. An evaluation of automated GIS tools for delineating karst sinkholes and closed depressions from 1-meter LIDAR-derived digital elevation data. In: Land L, Doctor DH, Stephenson JB (Eds), Sinkholes and the Engineering and Environmental Impacts of Karst. Proceedings of the Thirteenth Multidisciplinary Conference, May 6-10, Carlsbad, New Mexico, pp. 449-458.

Dowling, T. P.F., Spagnolo, M., Möller, P., 2015. Morphometry and core type of streamlined bedforms in southern Sweden from high resolution LiDAR. Geomorphology (accepted manuscript).

Drăguţ, L., Blaschke, T., 2006. Automated classification of land-form elements using object-based image analysis. Geomorphology 81(3), 330-344.

Drăguţ, L., Tiede, D., Levick, S. R., 2010. ESP: a tool to estimate scale parameter for multiresolution image segmentation of remotely sensed data. International Journal of Geographical Information Science 24(6), 859-871.

Eisank, C., Smith, M., Hillier, J., 2014. Assessment of multiresolution segmentation for delimiting drumlins in digital elevation models. Geomorphology 214, 452-464.

Ely, J. C., Clark, C. D., Spagnolo, M., Stokes, C. R., Greenwood, S. L., Hughes, A. L., Dunlop, P., Hess, D., 2014. Demonstration of a subglacial bedform continuum: Is a unifying formation theory required?. EGU General Assembly Conference Abstracts 16, p. 5533.

Engelhardt, H., Humphrey, N., Kamb, B., Fahnestock, M., 1990. Physical conditions at the base of a fast moving Antarctic ice stream. Science 248(4951), 57-59.

Euillades, L. D., Grosse, P., Euillades, P. A., 2013. NETVOLC: An algorithm for automatic delimitation of volcano edifice boundaries using DEMs. Computers & Geosciences 56, 151-160.

Evans, I. S., 1972. General geomorphometry, derivatives of altitude, and descriptive statistics. In: Chorley, R.J. (Ed.), Spatial Analysis in Geomorphology. Methuen, London, pp. 17–90

Evans, I. S., 2012. Geomorphometry and landform mapping: What is a landform?. Geomorphology 137(1), 94-106.

Finlayson, A., 2013. Digital surface models are not always representative of former glacier beds: palaeoglaciological and geomorphological implications. Geomorphology 194, 25–33.

Finlayson, D.P., 2005. Combined bathymetry and topography of the Puget Lowland, Washington State. [Online]. (http://www.ocean.washington.edu/data/pugetsound/). (Accessed April 2014).

Fowler, A. C., Chapwanya, M., 2014. An instability theory for the formation of ribbed moraine, drumlins and mega-scale glacial lineations. Proceedings of the Royal Society A: Mathematical, Physical and Engineering Science 470, 20140185.

Francek, M. A., 1991. A spatial perspective on the New York drumlin field. Physical Geography 12(1), 1-18.

Freeman, T. G., 1991. Calculating catchment area with divergent flow based on a regular grid. Computers & Geosciences 17(3), 413-422.

Gallant, J. C., Dowling, T. I., 2003. A multiresolution index of valley bottom flatness for mapping depositional areas. Water Resources Research 39(12).

Goldstein, B., 1994. Drumlins of the Puget Lowland, Washington State, USA. Sedimentary geology 91(1), 299-311.

Greenwood, S. L., Clark, C. D., 2009. Reconstructing the last Irish Ice Sheet 1: changing flow geometries and ice flow dynamics deciphered from the glacial landform record. Quaternary Science Reviews 28(27), 3085-3100.

Guisan, A., Weiss, S.B., Weiss, A.D., 1999. GLM versus CCA spatial modeling of plant species distribution. Plant Ecology 143, 107-122.

Haugerud, R. A., 2009. Preliminary geomorphic map of the Kitsap Peninsula, Washington. U.S. Geological Survey, Open-File Report 2009-1033, 2 sheets, scale 1:36,000.

Heidenreich, C., 1964. Some observations on the shape of drumlins. The Canadian Geographer/Le Géographe canadien 8(2), 101-107.

Hillier, J. K., Smith, M., 2008. Residual relief separation: digital elevation model enhancement for geomorphological mapping. Earth Surface Processes and Landforms 33(14), 2266-2276.

Hillier, J. K., Smith, M. J., 2012. Testing 3D landform quantification methods with synthetic drumlins in a real digital elevation model. Geomorphology 153, 61-73.

Hillier, J. K., Smith, M. J., Armugam, R., Barr, I., Boston, C. M., Clark, C. D., ..., Wooldridge, K., 2014. Manual mapping of drumlins in synthetic landscapes to assess operator effectiveness. Journal of Maps (ahead-of-print), 1-11.

Hooke, R. L., Medford, A., 2013. Are drumlins a product of a thermo-mechanical instability?. Quaternary Research 79(3), 458-464.

Hughes, A. L., Clark, C. D., Jordan, C. J., 2010. Subglacial bedforms of the last British Ice Sheet. Journal of Maps 6(1), 543-563.

Jasiewicz, J., Stepinski, T. F., 2013. Geomorphons—a pattern recognition approach to classification and mapping of landforms. Geomorphology 182, 147-156.

King, E. C., Hindmarsh, R. C., Stokes, C. R., 2009. Formation of mega-scale glacial lineations observed beneath a West Antarctic ice stream. Nature Geoscience 2(8), 585-588.

Kleman, J. I., Hattestrand, C., Borgstrom, I., 1997. Fennoscandian palaeoglaciology reconstructed using a glacial geological inversion model. Journal of Glaciology 43(144), 283-299.

Knight, J., 1997. Morphological and morphometric analyses of drumlin bedforms in the Omagh Basin, north central Ireland. Geografiska Annaler: Series A, Physical Geography 79(4), 255-266.

Landis, J. R., Koch, G. G., 1977. The measurement of observer agreement for categorical data. Biometrics 33(1), 159-174.

Lindsay, J. B., 2014. The Whitebox Geospatial Analysis Tools project and open-access GIS. Proceedings of the GIS Research UK 22nd Annual Conference, University of Glasgow, 16-18 April.

Liu, C., Frazier, P., Kumar, L., 2007. Comparative assessment of the measures of thematic classification accuracy. Remote sensing of environment 107(4), 606-616.

Lucieer, A., Stein, A., 2002. Existential uncertainty of spatial objects segmented from satellite sensor imagery. IEEE Transactions on Geoscience and Remote Sensing 40(11), 2518-2521.

Lucieer, A., Stein, A. 2005. Texture-based landform segmentation of LiDAR imagery. International Journal of Applied Earth Observation and Geoinformation 6(3), 261-270.

Maclachlan, J. C., Eyles, C. H., 2013. Quantitative geomorphological analysis of drumlins in the Peterborough drumlin field, Ontario, Canada. Geografiska Annaler: Series A, Physical Geography 95(2), 125-144.

MacMillan, R.A., 2005. A new approach to automated extraction and classification of repeating landform types. Abstract book Pedometrics 2005, Naples, Florida, USA, p.54.

MacMillan, R. A., Pettapiece, W. W., Nolan, S. C., Goddard, T. W., 2000. A generic procedure for automatically segmenting landforms into land-form elements using DEMs, heuristic rules and fuzzy logic. Fuzzy sets and Systems 113(1), 81-109.

Margold, M., Stokes, C. R., Clark, C. D., Kleman, J., 2014. Ice streams in the Laurentide Ice Sheet: a new mapping inventory. Journal of Maps (ahead-of-print), 1-16.

Margold, M., Stokes, C. R., & Clark, C. D., 2015. Ice streams in the Laurentide Ice Sheet: Identification, characteristics and comparison to modern ice sheets. Earth-Science Reviews 143, 117-146.

Mark, D. M., 1975. Geomorphometric parameters: a review and evaluation. Geografiska Annaler. Series A, Physical Geography 57, 165-177.

Menzies, J., 1979. A review of the literature on the formation and location of drumlins. Earth-Science Reviews 14(4), 315-359.

Minár, J., Evans, I. S., 2008. Elementary forms for land surface segmentation: The theoretical basis of terrain analysis and geomorphological mapping. Geomorphology 95(3), 236-259.

Mitchell, W. A., Riley, J. M., 2006. Drumlin map of the Western Pennines and southern Vale of Eden, northern England, UK. Journal of Maps 2(1), 10-16.

Molloy, I., Stepinski, T. F., 2007. Automatic mapping of valley networks on Mars. Computers & Geosciences 33(6), 728-738.

Munro-Stasiuk, M. J., Shaw, J., 2002. The Blackspring Ridge Flute Field, south-central Alberta, Canada: evidence for subglacial sheetflow erosion. Quaternary International 90(1), 75-86.

Napieralski, J., Nalepa, N., 2010. The application of control charts to determine the effect of grid cell size on landform morphometry. Computers & Geosciences 36(2), 222-230.

Neteler, M., Bowman, M. H., Landa, M., Metz, M., 2012. GRASS GIS: A multi-purpose open source GIS. Environmental Modelling & Software 31, 124-130.

NDEP, 2004. Guidelines for Digital Elevation Data. National Digital Elevation Program (NDEP), Version 1.0. (http://www.ndep.gov/NDEP_Elevation_Guidelines_Ver1_10May2004.pdf)

O'Callaghan, J. F., Mark, D. M., 1984. The extraction of drainage networks from digital elevation data. Computer vision, graphics, and image processing 28(3), 323-344.

Ó Cofaigh, C., Pudsey, C. J., Dowdeswell, J. A., Morris, P., 2002. Evolution of subglacial bedforms along a paleo-ice stream, Antarctic Peninsula continental shelf. Geophysical Research Letters 29(8), 41-1.

Ó Cofaigh, C., Stokes, C. R., Lian, O. B., Clark, C. D., Tulacyzk, S. 2013. Formation of mega-scale glacial lineations on the Dubawnt Lake Ice Stream bed: 2. Sedimentology and stratigraphy. Quaternary Science Reviews 77, 210-227.

Olaya, V., Conrad, O., 2009. Geomorphometry in SAGA. In: T. Hengl, H.I. Reuter (Eds.): Geomorphometry—Concepts, Software, Applications, Developments in Soil Science 33, Elsevier, Amsterdam (2009), pp. 293–308.

Patterson, C. J., Hooke, R. LeB., 1995. Physical environment of drumlin formation. Journal of Glaciology 41, 30–38.

Porter, S. C., Swanson, T. W., 1998. Radiocarbon age constraints on rates of advance and retreat of the Puget lobe of the Cordilleran ice sheet during the last glaciation. Quaternary Research 50(3), 205-213.

Prest, V. K., Grant, D. R., Rampton, V. N., 1968. Glacial map of Canada. Geological Survey of Canada, "A" Series Map.

QGIS Development Team, 2014. QGIS Geographic Information System. Open Source Geospatial Foundation Project. http://qgis.osgeo.org.

Rains, B., Shaw, J., Skoye, R., Sjogren, D., Kvill, D., 1993. Late Wisconsin subglacial megaflood paths in Alberta. Geology 21(4), 323-326.

Rignot, E., Mouginot, J., Scheuchl, B., 2011. Ice flow of the Antarctic ice sheet. Science 333(6048), 1427-1430.

Rose, J., 1987. Drumlins as part of a glacier bedform continuum. In: Menzies, J., Rose, J. (Eds), Drumlin Symposium. Balkema, Rotterdam, pp. 103-116.

Rutzinger, M., Hoefle, B., Kringer, K., 2012. Accuracy of automatically extracted geomorphological breaklines from airborne LiDAR curvature images. Geografiska Annaler: Series A, Physical Geography 94(1), 33-42.

Saha, K., Wells, N. A., Munro-Stasiuk, M., 2011. An object-oriented approach to automated landform mapping: A case study of drumlins. Computers & Geosciences 37(9), 1324-1336.

Schmidt, J., Hewitt, A., 2004. Fuzzy land element classification from DTMs based on geometry and terrain position. Geoderma 121(3), 243-256.

Shaw, J., 1983. Drumlin formation related to inverted melt-water erosional marks. Journal of Glaciology 29, 461-479.

Shaw, J., 2002. The meltwater hypothesis for subglacial bedforms. Quaternary International 90(1), 5-22.

Shaw, J., Kvill, D., Rains, B., 1989. Drumlins and catastrophic subglacial floods. Sedimentary Geology 62(2), 177-202.

Shaw, J., Rains, B., Eyton, R., Welssling, L., 1996. Laurentide subgiacial outburst floods: landform evidence from digital elevation models. Canadian Journal of Earth Sciences 33(8), 1154-1168.

Shaw, J., Pugin, A., Young, R. R., 2008. A meltwater origin for Antarctic shelf bedforms with special attention to megalineations. Geomorphology 102(3), 364-375.

Smalley, I., Warburton, J., 1994. The shape of drumlins, their distribution in drumlin fields, and the nature of the sub-ice shaping forces. Sedimentary geology 91(1), 241-252.

Sollid, J. L., Sørbel, L., 1994. Distribution of glacial landforms in southern Norway in relation to the thermal regime of the last continental ice sheet. Geografiska Annaler. Series A. Physical Geography 76, 25-35.

Spagnolo, M., Clark, C. D., Hughes, A. L., Dunlop, P., Stokes, C. R., 2010. The planar shape of drumlins. Sedimentary Geology 232(3), 119-129.

Spagnolo, M., Clark, C. D., Hughes, A. L., Dunlop, P., 2011. The topography of drumlins; assessing their long profile shape. Earth Surface Processes and Landforms 36(6), 790-804.

Spagnolo, M., Clark, C. D., Hughes, A. L., 2012. Drumlin relief. Geomorphology 153, 179-191.

Spagnolo, M., Clark, C. D., Ely, J. C., Stokes, C. R., Anderson, J. B., Andreassen, K., Graham, A. G. C., King, E., 2014. Size, shape and spatial arrangement of mega-scale glacial lineations from a large and diverse dataset. Earth Surface Processes and Landforms 39.11, 1432-1448.

Stearns, L. A., Smith, B. E., Hamilton, G. S., 2008. Increased flow speed on a large East Antarctic outlet glacier caused by subglacial floods. Nature Geoscience 1(12), 827-831.

Stepinski, T. F., Ghosh, S., Vilalta, R., 2006. Automatic recognition of landforms on Mars using terrain segmentation and classification. Proceedings of the 9th International Conference on Discovery Science, Barcelona, Spain, October 7-10, pp. 255-266.

Stokes, C. R., Clark, C. D., 1999. Geomorphological criteria for identifying Pleistocene ice streams. Annals of Glaciology 28(1), 67-74.

Stokes, C. R., Clark, C. D., 2001. Palaeo-ice streams. Quaternary Science Reviews 20(13), 1437-1457.

Stokes, C. R.,Clark, C. D., 2002. Are long subglacial bedforms indicative of fast ice flow?. Boreas 31(3), 239-249.

Stokes, C. R., Spagnolo, M., Clark, C. D., 2011. The composition and internal structure of drumlins: Complexity, commonality, and implications for a unifying theory of their formation. Earth-Science Reviews 107(3), 398-422.

Stokes, C. R., Spagnolo, M., Clark, C. D., Ó Cofaigh, C., Lian, O. B., Dunstone, R. B., 2013. Formation of mega-scale glacial lineations on the Dubawnt Lake Ice Stream bed: 1. size, shape and spacing from a large remote sensing dataset. Quaternary Science Reviews 77, 190-209.

Stout, J. C., Belmont, P., 2014. TerEx Toolbox for semi-automated selection of fluvial terrace and floodplain features from lidar. Earth Surface Processes and Landforms 39(5), 569-580.

Sun, X., Rosin, P. L., Martin, R. R., Langbein, F. C., 2007. Fast and effective feature-preserving mesh denoising. Visualization and Computer Graphics, IEEE Transactions on 13(5), 925-938.

Thorson, R. M., 1980. Ice-sheet glaciation of the Puget Lowland, Washington, during the Vashon Stade (late Pleistocene). Quaternary Research 13(3), 303-321.

Trenhaile, A. S., 1975. The morphology of a drumlin field. Annals of the Association of American Geographers 65(2), 297-312.

Van Asselen, S., Seijmonsbergen, A. C., 2006. Expert-driven semi-automated geomorphological mapping for a mountainous area using a laser DTM. Geomorphology 78(3), 309-320.

Wood, J., 1996. The geomorphological characterisation of digital elevation models. Ph.D. Thesis, University of Leicester.

This page intentionally left blank.

# Chapter 4. Conclusions

This thesis contributes to the testing and development of methods that can be used to produce a rich and robust LSB morphometric inventory which, in turn, facilitates our ability to resolve LSB genesis and to reconstruct paleo glacier dynamics and evolution. Focus was on the adequacy of previously used automated methods (GIS) for measuring LSB footprint orientation, length and longitudinal asymmetry (chapter 2), and the development of methodology for the semi-automated mapping (SAM) of LSB footprints from digital terrain models (DTMs) (chapter 3).

## 4.1. LSB measurement methods

Chapter 2 was motivated by the failure of previous LSB morphometric research to justify method appropriateness and by the realization that some previously used techniques (GIS) for measuring length and longitudinal asymmetry, such as the use of the longest straight line enclosed by LSB footprints to represent LSB orientation suitable to inferring formative flow direction, could be flawed. The results show that, while most of the previously used methods are appropriate for characterizing LSB samples in terms of central tendency (mean), some methods can yield large individual errors depending on LSB footprint general shape and outline complexity. The following is recommended:

1) the use of elliptical length (from ellipse fitted to the area and perimeter of footprints based on Euler's approximation; Clark et al., 2009; Lamsters, 2012; Spagnolo et al., 2014; Lamster and Zelčs, 2014) should be discontinued;

2) when analyzing morphometric data spatially, the longest straight line (LSL) fitting footprints (Spagnolo et al., 2010, 2011; Maclachlan and Eyles, 2013) should not be used for deriving orientation;

3) data based on footprints' standard deviational ellipse (SDE) (Lefever 1926; new method) should be preferred over data based on the LSL or on footprints' minimum bounding rectangle (MBR) (Napieralski and Nalepa, 2011; Dowling et al., 2015), for which error magnitude is dependent on footprint shape.

Re-analyzing previously characterized datasets using these 3 methods (LSL, SDE and MBR) would be useful for elucidating the degree of bias in their original morphometric data.

## 4.2. **LSB mapping**

Two new methods for the SAM of LSBs from DTMs were compared (Chapter 3). Both methods can be classified as object-based methods though neither makes use of the more complex segmentation algorithms typically associated with object-based (image) analysis (Lucieer and Stein, 2005; Blaschke, 2010). For terrain segmentation, one method (normalized closed contour method – NCCM) uses contouring (raster to vector format conversion) of a normalized local relief model and the other (landform elements mask method – LEMM) is based on a classification of the original DTM into landform elements. The NCCM outperformed the LEMM and published methods, but suffered from high overdetection. DTM preprocessing using directional smoothing constrained by LSB orientation for subduing post-LSB formation terrain modification drastically increased DTM suitability for SAM.

Automation is touted as the solution to the subjectivity of visual interpretation and MM, but that automated mapping methods allow for higher accuracy is not straightforward. While LSBs do seem to have "enough of" a topographic signature as to be suitable for SAM, problems, both conceptual and technical, persist and automatedly mapped footprints do not match the accuracy of MM-footprints. First, dealing with topographic changes post-dating LSB formation requires interpretation and decision at a level which automated methods have trouble reproducing. DTM preprocessing and the exclusion of areas where LSBs are likely to be particularly degraded lessen, but do not neglect, the issue; applying a spatially variable DTM preprocessing, such as depending on a morphometric classification of the test area (e.g., landform elements; e.g.,

Jasiewicz and Stepinski, 2013), may lead to additional improvements relative to the preprocessing flow used in this study. Second, the source of inter-operator differences in the MM of LSBs probably extends beyond the domain of intrinsic subjectivity; the openness/restrictiveness of LSBs' conceptual framework and the volatility of LSBs' definitions (in relation to uncertain genesis and limited morphometric descriptions) probably condition those differences and are a problem for both manual and automated mapping. Additionally, LSB (particularly drumlin) morphometric complexity and variability dictates that any morphometric definition of LSB is necessarily broad, setting limits to the success of a single SAM method.

Manual mapping still seems to be the only appropriate method to date that allows a sufficiently detailed (individual bedform) morphometric inventorying for the purpose of LSB formation hypothesis testing (e.g., the ice-keel groove-ploughing hypothesis prediction of a downflow decrease in bedform amplitude – Clark et al., 2003). For mapping individual LSB footprints (either all LSBs or subcategories), SAM likely will never reach the accuracy of MM. Nonetheless, with further method development, SAM will be able to replace MM in some inventories, such as when differences between individual bedforms are less relevant than the distribution of averages over wider spatial extents. The analysis of the spatial distribution of LSB elongation at the ice-stream scale is an example of a potential application. With further development, the NCCM has the potential to do this confidently. For the regional-scale mapping of properties irrespective of footprints (e.g., ridgeline orientation), raster-based analyses may be a better solution, particularly because processing of vector data is computationally more demanding.

Local relief modeling (NCCM method) entailed the generation of artifacts and significant differences between various tested algorithms. A most obvious potential solution to this problem is subdividing the NCCM processing flow for separately mapping LSBs on relatively flat terrain and on slopes. On flat terrain, contours directly derived from the DTM (elevation relative to fixed datum) may outperform NLR contours. For LSBs on slopes, alternatives to NLR modelling for DTM detrending include subtracting a smooth (e.g., low degree polynomial) surface based on local elevation minima (referent to the original subglacial landscape) in the DTM from the DTM.

The current morphometric data and reference datasets used in evaluating LSB automated method performance are based on MM even though the magnitude of subjective differences in the MM of LSBs is not well understood (cf. Hillier et al., 2014). Advances in this regard require revisiting previously mapped areas and conducting tests using synthetic DTMs (with a predetermined number of LSBs and representing LSBs in their original condition) (Hillier and Smith, 2012; Hillier et al., 2014; Eisank et al., 2014). Assessing inter-operator MM differences in previous study areas requires using the same data sources, mapping scales and visual representations used in the corresponding studies, and should involve different research teams (differences in conceptualizations) and researchers with prior LSB mapping experience (e.g., Clark et al., 2009; Spagnolo et al., 2010, 2011, 2012; Stokes et al., 2013; Spagnolo et al., 2014; Lamsters and Zelčs, 2014; Dowling et al., 2015). On the other hand, synthetic DTMs are important because they allow determining the exact number, location and morphometry of the landforms they represent, and thus permit evaluating MM subjectivity in absolute terms (Eisank et al., 2014; Hillier et al., 2014). Such tests are important for defining operational mapping guidelines.

Future studies on the development of automated LSB mapping methods should converge in terms of the measures used to assess performance. Also, assessment methodologies have been generous in their definition of success; as methods improve more realistic targets need to be set. The morphometric detection rate is incipient in this regard but can be turned into a more rigorous measure through the redefinition of applied, and addition of new, thresholds. Weighting this morphometric detection rate by the ratio of morphometric detection to overdetection, itself weighted by the *a priori* probability of LSBs in the study area, will allow a strict, goal-oriented assessment of performance.

## 4.3. **Novelty of conducted research**

The research reported in this thesis is novel in geomorphology in that it develops and assesses morphometric methods rather than simply applying untested methods to new field areas. Prior to this thesis, the adequacy of LSB morphometric measurement methods had scarcely been addressed. The standard deviational ellipse (Lefever, 1926)

was used for the first time to quantify LSB morphometry and outperformed previously used methods. DTM preprocessing using anisotropic filtering constrained by LSB orientation has not been used before (not found in the reviewed literature) and was associated with a drastic improvement in DTM (terrain) suitability for SAM. The new LSB SAM methods tested in chapter 2 were devised based on "first principles" and diverge considerably from previous approaches, which were all based on multiresolution segmentation (Baatz and Schäpe, 2000). Also, whereas all previous (semi-)automated mapping methods were developed based on very expensive software (eCognition®), existent opensource software is fully adequate for applying both the NCCM and the LEMM. The SAM performance assessment was relatively elaborate when compared to previous LSB (semi-)automated mapping studies, highlighting inadequacies in previous performance assessment methodologies, and leading to recommendations for future studies (above).

This thesis contributes to advances in the fields of glacial geomorphology and geomorphometry. More generally, conducted research is relevant for studies applying rotation-variant morphometrics (independently of the scientific field) and developing DTM-based automated mapping methodologies.

## 4.4. References


Baatz, M., Schäpe, A., 2000. Multiresolution Segmentation – an optimization approach for high quality multi-scale image segmentation. In: Strobl, Blaschke, Griesebner (Eds), Angewandte Geographische Informationsverarbeitung XII, Wichmann-Verlag, Heidelberg, pp. 12-23.

Blaschke, T., Lang, S., Lorup, E., Strobl, J., Zeil, P., 2000. Object-oriented image processing in an integrated GIS/remote sensing environment and perspectives for environmental applications. Environmental information for planning, politics and the public 2, 555-570.

Clark, C. D., Tulaczyk, S. M., Stokes, C. R., Canals, M., 2003. A groove-ploughing theory for the production of mega-scale glacial lineations, and implications for ice-stream mechanics. Journal of Glaciology 49(165), 240-256.

Clark, C. D., Hughes, A. L., Greenwood, S. L., Spagnolo, M., Ng, F. S., 2009. Size and shape characteristics of drumlins, derived from a large sample, and associated scaling laws. Quaternary Science Reviews 28(7), 677-692.

Dowling, T. P.F., Spagnolo, M., Möller, P., 2015. Morphometry and core type of streamlined bedforms in southern Sweden from high resolution LiDAR. Geomorphology (accepted manuscript).

Eisank, C., Smith, M., Hillier, J., 2014. Assessment of multiresolution segmentation for delimiting drumlins in digital elevation models. Geomorphology 214, 452-464.

Hillier, J. K., Smith, M. J., 2012. Testing 3D landform quantification methods with synthetic drumlins in a real digital elevation model. Geomorphology 153, 61-73.

Hillier, J. K., Smith, M. J., Armugam, R., Barr, I., Boston, C. M., Clark, C. D., ..., Wooldridge, K., 2014. Manual mapping of drumlins in synthetic landscapes to assess operator effectiveness. Journal of Maps (ahead-of-print), 1-11.

Jasiewicz, J., Stepinski, T. F., 2013. Geomorphons—a pattern recognition approach to classification and mapping of landforms. Geomorphology 182, 147-156.

Lamsters, K., 2012. Drumlins and related glaciogenic landforms of the Madliena Tilted Plain, Central Latvian Lowland. Bulletin of the Geological Society of Finland 84, 45–57.

Lamsters, K., Zelčs, V., 2014. Subglacial bedforms of the Zemgale Ice Lobe, south-eastern Baltic. Quaternary International (in press).

Lefever, D. W., 1926. Measuring geographic concentration by means of the standard deviational ellipse. American Journal of Sociology 32, 88-94.

Lucieer, A., Stein, A., 2005. Texture-based landform segmentation of LiDAR imagery. International Journal of Applied Earth Observation and Geoinformation 6(3), 261-270.

Maclachlan, J. C., Eyles, C. H., 2013. Quantitative geomorphological analysis of drumlins in the Peterborough drumlin field, Ontario, Canada. Geografiska Annaler: Series A, Physical Geography 95(2), 125-144.

Napieralski, J., Nalepa, N., 2010. The application of control charts to determine the effect of grid cell size on landform morphometry. Computers & Geosciences 36(2), 222-230.

Spagnolo, M., Clark, C. D., Hughes, A. L., Dunlop, P., Stokes, C. R., 2010. The planar shape of drumlins. Sedimentary Geology 232(3), 119-129.

Spagnolo, M., Clark, C. D., Hughes, A. L., Dunlop, P., 2011. The topography of drumlins; assessing their long profile shape. Earth Surface Processes and Landforms 36(6), 790-804.

Spagnolo, M., Clark, C. D., Hughes, A. L., 2012. Drumlin relief. Geomorphology 153, 179-191.

Spagnolo, M., Clark, C. D., Ely, J. C., Stokes, C. R., Anderson, J. B., Andreassen, K., Graham, A. G. C., King, E., 2014. Size, shape and spatial arrangement of mega-scale glacial lineations from a large and diverse dataset. Earth Surface Processes and Landforms 39(11), 1432-1448.

Stokes, C. R., Spagnolo, M., Clark, C. D., Ó Cofaigh, C., Lian, O. B., Dunstone, R. B., 2013. Formation of mega-scale glacial lineations on the Dubawnt Lake Ice Stream bed: 1. size, shape and spacing from a large remote sensing dataset. Quaternary Science Reviews 77, 190-209.

# Appendix A.

# Puget Lowland drumlin field integrated terrain map

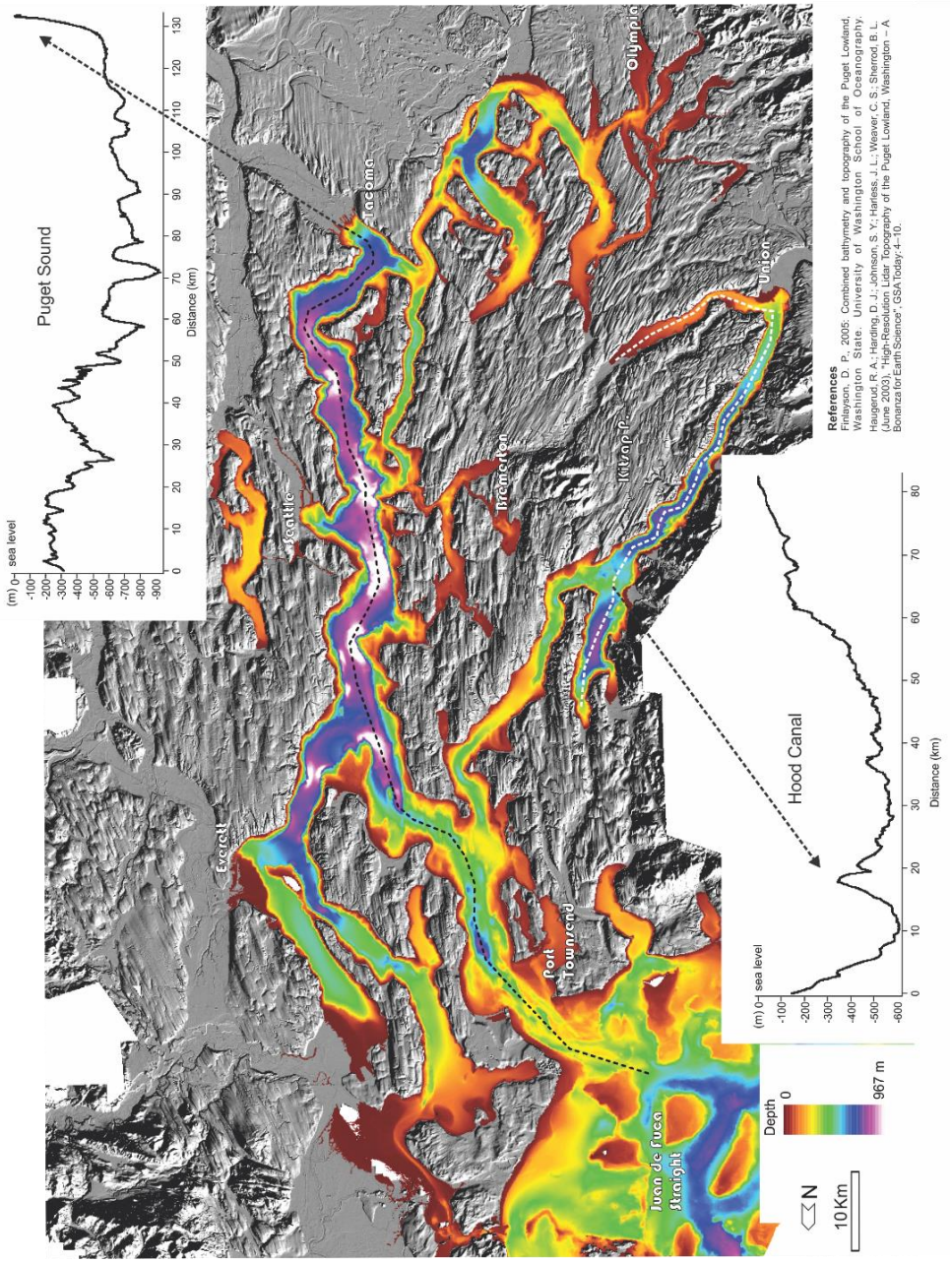


**Figure A1**. Puget Lowland Drumlin Field integrated terrain map. Areas above and below present-day sea level are represented with a hillshaded terrain model and a color elevation rendering, respectively.

# Appendix B.

# LSB manual mapping in the Puget Lowland drumlin field

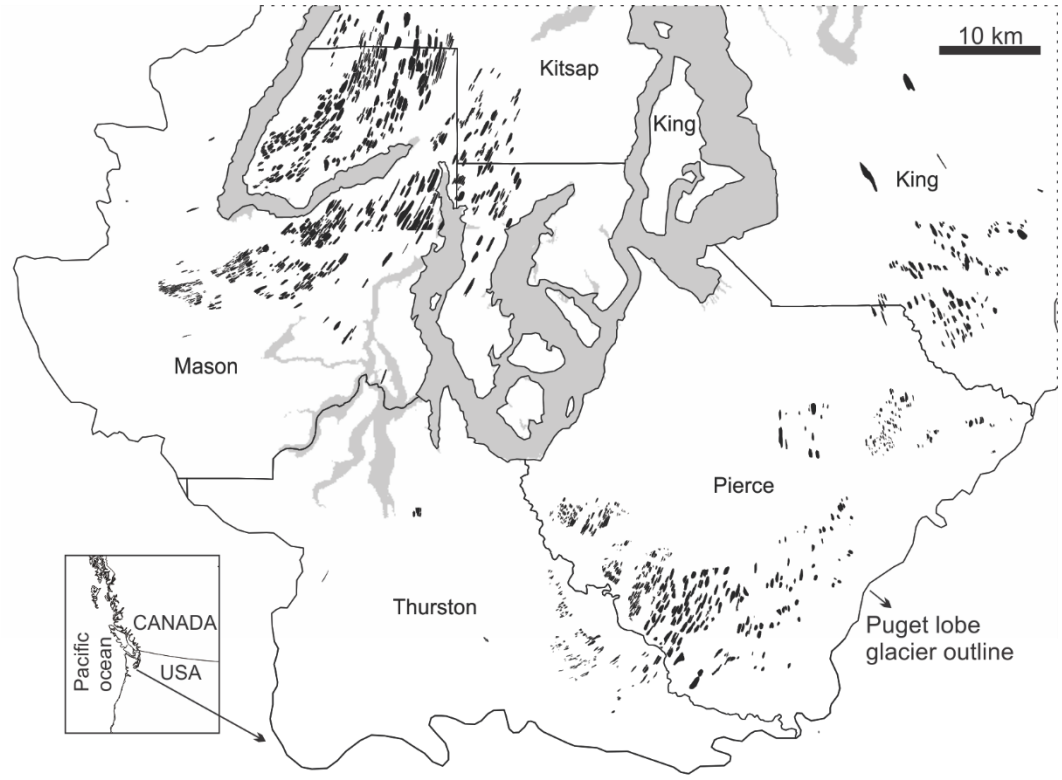


**Figure B1**. Manually mapped LSBs (black-fill polygons) (*n* = 1.6k) in central and southern Puget Lowland, WA, USA. Inner labels and lines are county names and boundaries. Mapping was conducted mostly over hillshaded terrain models, and contour maps, derived from a 1.8 m cell-size DTM (http://pugetsoundlidar.ess.washington.edu/About_ PSLC.htm). Puget Lobe limit (local Last Glacial Maximum) from Thorson, 1980.

# Appendix C.

# Field investigations on LSB composition in the Puget Lowland drumlin field – visited sites

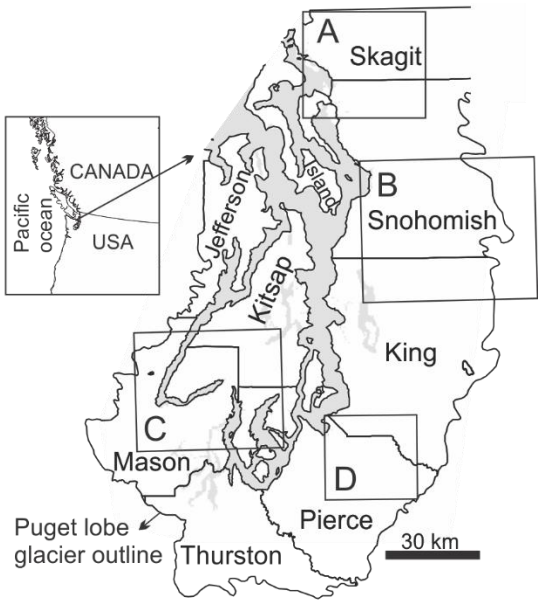


**Figure C1**. Areas visited during field work in the Puget Lowland, WA (quadrangles A-D). Puget Lobe limit (local Last Glacial Maximum) from Thorson, 1980.

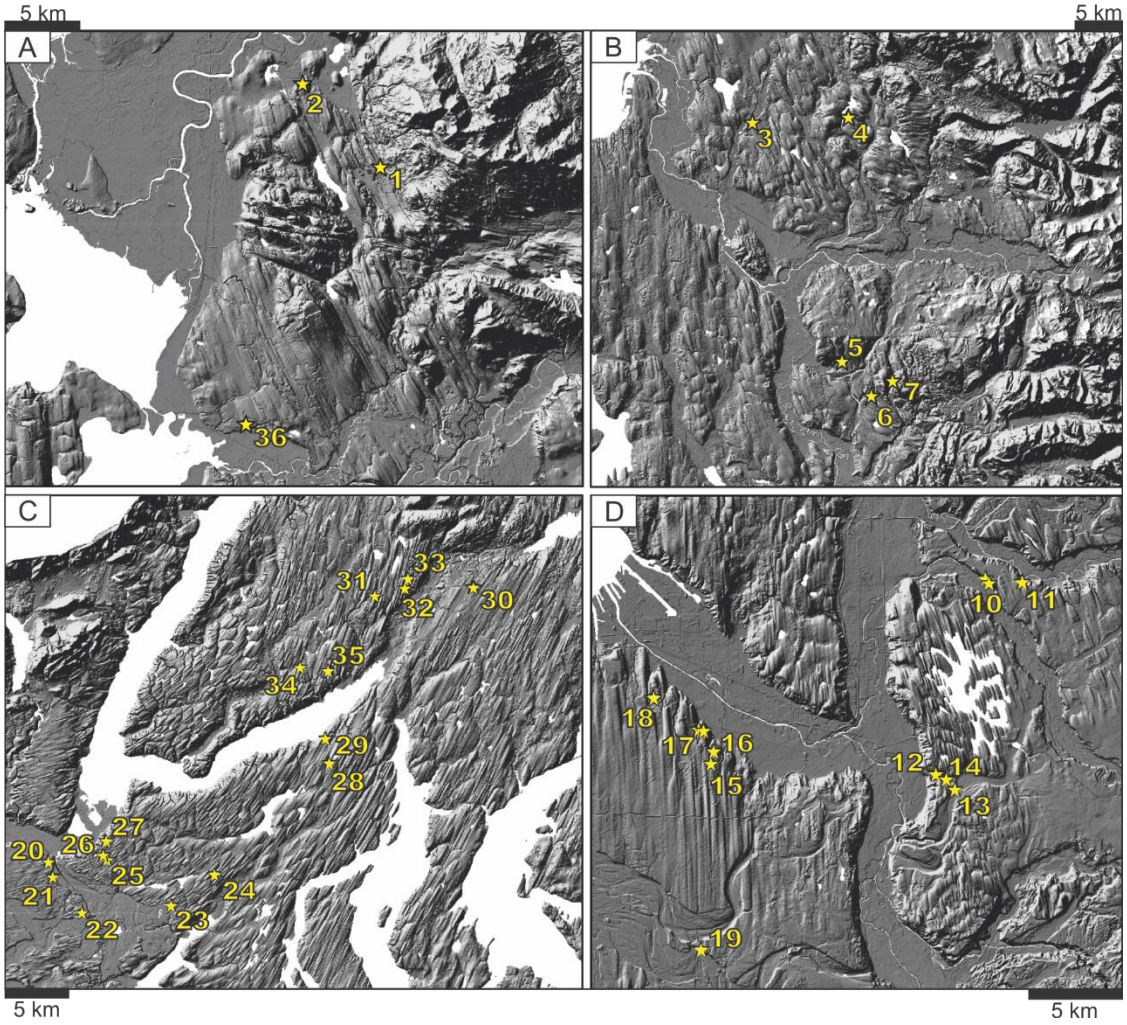


**Figure C2**. Location of sedimentary exposures visited during field work (see Fig. C1 for location of quadrangles A-D). Traditional sedimentary descriptions were done in 30 of the 36 sites. Eighteen sites expose drumlin sediments; 16 sites potentially expose drumlin sediments; 4 or 5 sites are positioned in between or by drumlins; 2 or 3 sites appear to expose sediments stratigraphically lower than drumlins. Hillshaded terrain models were derived from a 1.8 m cell-size DTM (http://pugetsoundlidar.ess.washington.edu/About_ PSLC.htm).